A MICROMECHANICS STUDY ON CARBON-BASED AND MULTIFERROIC COMPOSITES

By

YANG WANG

A dissertation submitted to the

Graduate School-New Brunswick

Rutgers, The State University of New Jersey

In partial fulfillment of the requirements

For the degree of

Doctor of Philosophy

Graduate Program in Mechanical and Aerospace Engineering

Written under the direction of

Dr. George J. Weng

And approved by

_____

_____

_____

_____

New Brunswick, New Jersey

May, 2016

ABSTRACT OF THE DISSERTATION

A micromechanics study on
carbon-based and multiferroic composites
by YANG WANG

Dissertation Director:

Dr. George J. Weng

In this thesis, two physical properties of modern composites are studied. One is the electrical conductivity of carbon nanotube- and graphene-based polymer nanocomposites, and the other is the magnetoelectric coupling of highly anisotropic piezoelectric-piezomagnetic multiferroic composites. Along the way, several related issues have also been examined. These include percolation threshold, interfacial resistance, electron tunneling, and filler agglomeration in the first case, and, in the second one, the influence of aspect ratio of inclusions, imperfect interface, and phase connectivity. The studies of these two problems are linked by the common theme of micromechanics theory but cast in different settings. The effective electrical conductivity and percolation threshold of CNT-based nanocomposites are investigated with the effective-medium approach as the backbone. We then introduce of a diminishing layer of interface with an interfacial resistivity that is further modified by Cauchy's statistical distribution function to account for the additional tunneling-assisted interfacial conductivity. The issue of filler agglomeration is examined in details for graphene-based nanocomposites, in which a two-scale

effective-medium approach with graphene-rich and graphene-poor regions is also developed. Our predictions are shown to be in close agreement with experimental data. For multiferroic composites, our focus is on the intriguing property of magnetoelectric coupling coefficient which is absent in either piezoelectric or piezomagnetic phase but owned by overall composites. We study this iconic effect in depth for $BaTiO_3$-$CoFe_2O_4$ system with different types of connectivity, including 1-3, 0-3, 2-2, that display the inclusion-matrix morphology, and 1-1, 0-0 connectivity that are marked by their symmetric geometrical footing. These two classes of composites are analyzed by the Mori-Tanaka method and the effective-medium approach, respectively. We demonstrate how the magnetoelectric coupling coefficients, α_{33} and α_{11}, are highly dependent on the phase volume concentration, inclusion aspect ratio, interface effect, and phase connectivity. Our results also reveal that the magnetoelectric coupling of 0-0 connectivity are substantially higher than that of 0-3 connectivity, but the difference between 1-1 and 1-3 connectivity is limited. In the end, we point to the need of exploring the physical mechanism of interfacial resistance for carbon-based nanocomposites and the nonlinear coupling behaviors for ferroelectric-ferromagnetic composites in our future work.

Acknowledgment

First and foremost, I would like to offer my deepest gratitude and appreciation to my PhD advisor, Dr. George J. Weng, for his valuable guidance and support throughout my entire PhD study. Being dedicated to research and teaching, and responsible for students, Dr. Weng is the perfect example of a scholar and an advisor. He has a great passion for research and a keen sense of research trends, and most importantly, he keeps being hardworking and productive while always maintains high academic standards. From him I have learnt how to get into research, and his spirit of being diligent and conscientious. As a Chinese proverb goes, "He who teaches me for one day is my father for life." I am forever indebted to Dr. Weng for enriching my knowledge and skills, for making me a better researcher, and for continuously supporting my living during my study.

Next I would like to express my sincere thanks to Dr. Jackie Li, Dr. Assimina A. Pelegri, and Dr. Jerry Shan for being my dissertation committee members and offering their much appreciated advice and suggestions on how to improve my research work. During my proposal, they have already shown their comprehensive thinking and meticulous attention to every detail. These are the necessary qualities for being a researcher, and the qualities I should learn from them.

In addition, my appreciation goes to my group members, Roohollah Hashemi, Jia Hao and Xiaodong Xia, for their support and help. I am also thankful to my friends and fellow students, including Wei Song, Lixin Hu, Xike Zhao, Huihui Qi, Michelle Hsiao-Fang Lee, Zhihua Wang, Yi Pan, Yizhai Zhang, Yang Zhang, Peinan Ge, Han

Sun, Fei Liu, Kuo Chen, Kaiyan Yu, Wanlin Du, Hua Hong, Kuan-yu Chen, Wuhan Yuan, Hanxiong Wang, Xiaoshi Su, Zhaocheng Lu, Wei Wang, Mengdi Xing, Mena Tawfik, Joseph Lakawicz, Michael Pavlou and Peter Balogh. It is so good to have all of you during my life as a PhD student.

Particularly, I want to offer my special thank to my cousin, Dr. Shengquan Yan. His experience has significantly influenced and inspired me to study abroad and pursuit a PhD, and his help is crucial in my PhD application. He has always been a great role model to me.

Finally, I am truly grateful to my father, Jianfeng Wang, and my mother, Yumei Ma. They have been the best parents ever since I was born, and from whom I have received tremendous love and care. Without their encouragement and support, I could never be confident and determined enough to leave my hometown and cross the ocean, and then to study and thrive in this new nation. Even though I am far away from home, they have always provided the best support to me, both mentally and financially. No words can adequately describe my true love and gratefulness to them, my dearest parents.

Dedication

To my father, Jianfeng Wang, and my mother, Yumei Ma. Proud to be their son.

Table of contents

List of tables

List of illustrations

Chapter 1.
Introduction

The focus of this thesis is on two physical properties of modern composites. One is the electrical conductivity of carbon nanotube- and graphene-based polymer nanocomposites, and the other is the magnetoelectric coupling of highly anisotropic piezoelectric-piezomagnetic multiferroic composites. Both properties are of some fundamental importance. Since these issues involve lots of complex transport and coupled processes, the determination of these properties still remains a challenge. For instance, in the former case the percolation threshold, interfacial resistance, electron tunneling, and filler agglomeration can play very critical roles, while in the latter the aspect ratio of inclusions, imperfect interface, and phase connectivity can all greatly affect the magnetoelectric coupling. Our objective is to provide some continuum models so that both properties can be determined with all these microstructural features taken into account. In this way our study will help shed new light on how the observed properties result from these intrinsic features of the composites, and on how the desired effective electrical conductivity and magnetoelectric coupling can be obtained through proper design of microstructures.

In recent years with the development of nanotechnology, more and more carbon particles whose dimensions are on the scale of nanometers have been applied to composite materials for enhanced mechanical, thermal and electrical performance. Generally these carbon particles are used as fillers and mixed into the polymer

material matrix to produce a class of carbon-based nanocomposites. Two most typical and widely used carbon fillers are carbon nanotubes (CNTs) and graphene. Both classes of carbon fillers are known to possess very high mechanical stiffness and strength, and exceptional thermal and electrical conductivity. Therefore the addition of carbon nanofillers to polymer matrix can greatly improve their overall properties and provide some unique features for the nanocomposites. In the context of electrical conductivity, one of the most intriguing features is that the overall conductivity of carbon-based nanocomposites will increase sharply at certain filler volume concentration, which is the well-known percolation phenomenon. Around that particular filler concentration, which is referred to as percolation threshold, the overall conductivity can rapidly grow for several orders of magnitude, from almost insulating like the polymer matrix to highly conductive as pure carbon fillers. In addition, for CNT and graphene fillers their percolation thresholds tend to be very low, with some reported values as low as 0.1 vol.%. It is necessary to develop a theoretical model to explain these characteristics of carbon-based nanocomposites, which serves as the first focus of this research.

The second focus of this thesis is on the study of piezoelectric, piezomagnetic, and multiferroic composites. The latter is the combination of piezoelectric and piezomagnetic phases. For this kind of composite materials, one important characteristic is the existence of multiple fields; it is not just a single field like the case in the electrical conductivity problem. This will result in significant coupling effects between different kinds of field. For example, there is electroelastic coupling

for the piezoelectric phase and magnetoelastic coupling for the piezomagnetic phase, and, for multiferroic composites, there is an additional magnetoelectric coupling effect. Among them the determination of magnetoelectric coupling coefficient has been the focus of many studies. It is not an intrinsic property for any constituent phase of multiferroic composites; it is rather a kind of "$0+0\rightarrow 1$" product effect that is exclusive for the overall multiferroic composites. This product effects depend on the phase volume concentration, inclusion shape, interface condition, and phase connectivity, which could be 0-3, 1-3 and 2-2 connectivity on one hand, or 0-0 and 1-1 connectivity on the other. We will show that the theoretical formulation of multiferroic composites is far more complicated than the problem of elasticity or electrical conductivity, for the reason that it is a highly anisotropic and highly coupled implicit problem. We will demonstrate that analytical solutions are only available for composites with 1-3 and 2-2 connectivity, and for other cases the solution can only be numerically evaluated.

The study of these two physical problems will be linked by the common theory of micromechanics. This is because in these problems, their linear constitutive relations can be treated in the same way as those in micromechanics theory. The theory of micromechanics has been a powerful tool in the study of effective properties of composite materials. It is a homogenization approach that can predict the macroscopic composite properties on the basis of material properties and geometries of each individual phase on the microscopic scale. The most important foundation of micromechanics was laid by Eshelby in his famous paper in 1957.[1] From then on, a

comprehensive system of micromechanics theories has been built to analyze the overall mechanical response of composite materials. However, the capability of micromechanics is not only limited in mechanical context; it can be further applied to investigate a wide range of physical properties such as thermal and electrical conductivity, or dielectric and piezoelectric properties. Thermal conductivity is the first territory that has been thoroughly studied by means of micromechanics approach. Later as the development of nanotechnology begins to grow, micromechanics also becomes an essential part of the theoretical foundations for nanocomposites. Furthermore, with proper theoretical treatment micromechanics is capable of extending from single material property to composites that are subjected to multiple fields, such as the combination of elastic, electric and magnetic fields. In this case, the coupling effect among various fields, which serves as the figure of merits for such class of composites, can also be successfully addressed. Micromechanics approach has indeed gone beyond the context of mechanics and become an effective means to deal with multidisciplinary problems for composite materials. In the following sections, several important concepts and methods in micromechanics theory, which are so essential that serve as the theoretical foundations of our current study, are introduced in the first place. Then the introductions to carbon-based and multiferroic composites are presented subsequently.

1.1. Eshelby S-tensor

In 1957 Eshelby published the most important paper in the field of

micromechanics "The Determination of the Elastic Field of an Ellipsoidal Inclusion, and Related Problems".[1] In this seminal work he provided the solution to the induced strain field ε inside an ellipsoidal inclusion under a uniform eigenstrain ε^*. It can be expressed in a simple relation

$$\varepsilon_{ij} = S_{ijkl}\varepsilon^*_{kl}, \tag{1.1}$$

where fourth-order tensor S_{ijkl} is the Eshelby S-tensor. This result will then facilitate the study of Eshelby equivalent inclusion for inhomogeneities and the formulation of strain concentration tensor, so that a more accurate estimation of the effective properties of composite materials becomes feasible. The components of the S-tensor depend on the ellipsoidal inclusion's material properties (or in Eshelby equivalent inclusion, the material properties of the matrix phase) and its shape, which is generally characterized by aspect ratio (length-to-diameter ratio) α. And only when the inclusion has ellipsoidal shape does the S-tensor components become constant, so that the induced strain field ε is also uniform over the entire inclusion. This important conclusion has been proved by Liu in 2008.[2] Despite of this ellipsoidal shape requirement, the Eshelby S-tensor is still capable of studying many kinds of composite structures. That is because a variety of inclusion shapes, such as long fiber, particle and thin plate, can be treated as the special cases of general ellipsoids with α as ∞, 1 and 0.

The Eshelby S-tensor is established in the context of elasticity, but similar concepts also exist in other contexts. For example, in the context of magnetic field, the induced demagnetizing field of a uniformly magnetized ellipsoidal specimen is

proportional to the magnetization by a constant called demagnetizing factor. While in the context of electric field there is also depolarizing factor describing the relation between induced depolarizing field and polarization in an ellipsoidal body. Both depolarizing and demagnetizing factors are the counterparts of the Eshelby S-tensor in their own context. And due to their mathematical analogies, all of them can be evaluated in a common way. Therefore in our study, the concept of the S-tensor has been expanded to cover not only the elastic S-tensor, but also its counterpart in electrical conductivity, and electric and magnetic field. For the problems with isotropic material properties, the evaluation of the S-tensor components is relatively straightforward and analytical results are available. However, for anisotropic material properties, e.g., the moduli tensor of multiferroic composites, obtaining the S-tensor is not trivial. It requires carrying out some complex integrals and only numerical results exist in most cases. Several notable works, including those by Dunn and Taya,[3] Dunn,[4] Huang and Yu,[5] Huang *et al.*,[6] Li and Dunn,[7] and Mikata,[8] have greatly contributed to the study of the S-tensor in piezoelectric and piezomagnetic materials. The determination of the S-tensor is given in details in Appendix C.

1.2. Mori-Tanaka method

Mori and Tanaka calculated the average stress induced by transformed homogeneous inclusions in a large matrix volume in 1973.[9] Based on their average stress concept and Eshelby equivalent inclusion, Weng (1984)[10] and Benveniste (1987)[11] respectively built the formulation of Mori-Tanaka (M-T) method to estimate

the effective mechanical properties of composite materials. Meanwhile Hatta and Taya[12] and Nan *et al*.[13] applied M-T method in the context of thermal conductivity. The latter used a Green function-based multiple scattering approach and its result was identical to the explicit formula of Weng.[14] Later M-T method has also been extended to the study of multiferroic composite materials by Nan,[15] Dunn and Taya,[16] Huang and Kuo,[17] and Li and Dunn.[18] M-T method has a typical matrix-inclusion type of geometry, i.e., each inclusion phase is embedded into an infinite matrix. In mechanical setting, the boundary of matrix is subjected to prescribed traction or displacement boundary conditions, which corresponds to the average stress or strain field of the composite. When the composite has prescribed traction boundary condition, the average strain in inclusion phase *r* is related to the average strain in the matrix by strain concentration tensor $\mathbf{A}_r$,

$$\mathbf{A}_r = \left[\mathbf{I} + \mathbf{S}_r \mathbf{L}_0^{-1}\left(\mathbf{L}_r - \mathbf{L}_0\right)\right]^{-1}, \tag{1.2}$$

where $\mathbf{S}_r$, $\mathbf{L}_r$ are the S-tensor and stiffness tensor of phase *r*, $\mathbf{L}_0$ is the stiffness tensor of the matrix and $\mathbf{I}$ is the fourth-order identity tensor given by $I_{ijkl} = (1/2)\left(\delta_{ik}\delta_{jl} + \delta_{il}\delta_{jk}\right)$. With the strain concentration tensor $\mathbf{A}_r$, the effective stiffness tensor of the composite, $\mathbf{L}_e$, can be expressed as

$$\mathbf{L}_e = \left(c_0\mathbf{L}_0 + \sum c_r \mathbf{L}_r \mathbf{A}_r\right)\left(c_0\mathbf{I} + \sum c_r \mathbf{A}_r\right)^{-1}, \tag{1.3}$$

where *c* term represents the volume concentration, subscript 0 denotes the matrix phase, and *r* denotes the *r*th inclusion phase. As has been pointed out by Weng and further proved by Benveniste, M-T method can also be used to calculate the effective compliance tensor of the composite $\mathbf{M}_e$ from exactly the same derivation. One can

simply substitute each stiffness tensor $\mathbf{L}$ in Eq. (1.3) with its related compliance tensor $\mathbf{M}$ by $\mathbf{M}=\mathbf{L}^{-1}$, and replace each S-tensor $\mathbf{S}_r$ by the corresponding T-tensor $\mathbf{T}_r$ which satisfies $\mathbf{T}_r=\mathbf{L}_0\left(\mathbf{I}-\mathbf{S}_r\right)\mathbf{M}_0$. Here the T-tensor describes the relation between the induced stress field and the uniform eigenstress in an ellipsoidal inclusion. In this way the result of $\mathbf{L}_e$ and $\mathbf{M}_e$ by M-T method will always satisfy $\mathbf{M}_e=\mathbf{L}_e^{-1}$ at any given volume concentration.

In general, M-T method is capable of delivering the effective property of composite materials, no matter which form is used to describe the material property. For a pure elastic problem, there are two different ways to write its constitutive equation, i.e., stress vs. strain or strain vs. stress. Hence we can take either stiffness tensor or compliance tensor to characterize the elastic material property. As mentioned above, both effective stiffness and compliance tensor of composite materials can be evaluated by M-T method in the same fashion, and their results at any given volume concentration are always interchangeable. To apply M-T method it is necessary to obtain the corresponding S-tensor (or T-tensor). Even though the S-tensor is usually not symmetric, its product with the inverse of stiffness tensor $\mathbf{S}\mathbf{L}_e^{-1}$ (or $\mathbf{T}\mathbf{M}_e^{-1}$) is symmetric, provided that the stiffness tensor $\mathbf{L}$ (or $\mathbf{M}$) is symmetric. Due to these abovementioned similarities, it is convenient to regard both the stiffness and compliance tensor as two different kinds of generalized moduli tensors, and both the S-tensor and T-tensor as two different kinds of generalized S-tensors, so that they can be treated under the same theoretical framework of M-T method. For a multiferroic problem, we can take one quantity from mechanical stress σ and strain ε, another

from electric field E and electric displacement D, and the third one from magnetic field H and magnetic flux density B, to be a set of independent variables. Therefore there are 8 different ways to write its constitutive equations, and thus there exist 8 different kinds of generalized electro-magneto-elastic moduli tensors, each with an associated generalized S-tensor. It can be shown that these 8 kinds of generalized moduli tensors are equivalent in describing the property of multiferroic composites. They are also interchangeable, which means from any one given kind we can derive the rest 7 kinds, and so do the 8 kinds of generalized S-tensors. The details of transforming these 8 kinds of generalized moduli tensors and S-tensors between each other are presented in Appendix B and C. For each kind of generalized moduli tensor of multiferroic composites, its effective value can be evaluated by M-T method, and

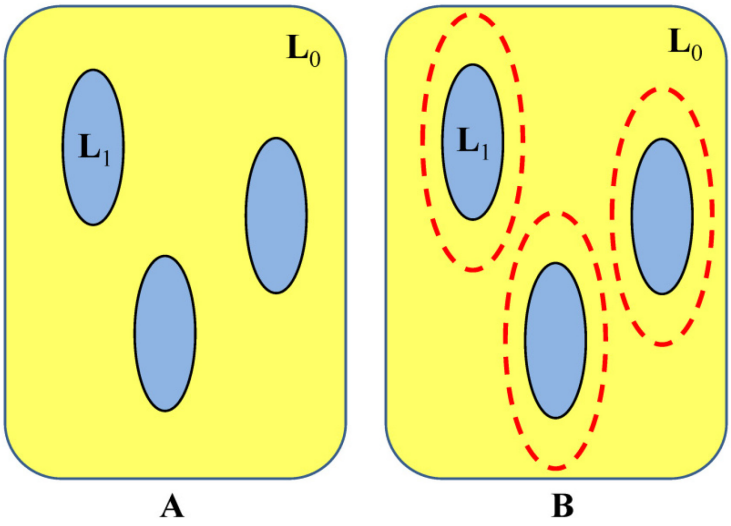

FIG. 1.1. A typical two-phase composite model with aligned ellipsoidal inclusions, showing (a) inclusions are directly embedded in the matrix, and (b) inclusions are coated by surrounding matrix first to form coated inclusions (denoted by red dashed lines).

all of them are interchangeable at any given volume concentration. This feature of M-T method enables us to study the effective property of multiferroic composites

under different prescribed boundary conditions (e.g., free standing or with substrate).

In M-T method, we only need to calculate the S-tensor for the matrix, which makes it very easy to implement at low computational cost. The result of M-T method is also explicit and linear. The former feature can be directly observed from Eq. (1.3), while the latter can be illustrated by the following example. Consider a two-phase composite, as shown in Fig. 1.1 Case A, with ellipsoidal inclusions which have volume concentration c_1. The effective property of this composite can be directly obtained by using M-T method once, or as an alternative way, we can imagine every inclusion is surrounded by a layer of matrix material to form a coated inclusion, and then these coated inclusions are embedded in the matrix (as shown in Fig. 1.1 Case B). For the second case, we should first use M-T method to get the effective property of the coated inclusion, and use it one more time to calculate the effective property of the overall composite with coated inclusions and a matrix. Since the two microstructures in Fig. 1.1 are exactly identical in nature, we expect the same results from these two ways of calculation. And it turns out to be true as long as the coated inclusion has the same shape as the original inclusion, regardless of the thickness of coating layer. This is exactly the linear behavior of M-T method.

1.3. Effective-medium approach

Effective-medium approach (or EMA), which is also called coherent potential approximation, is a symmetric version of self-consistent method and can date back to the original work of Bruggeman in 1935.[19] Later Landauer (1952)[20] first applied

effective-medium approach to study the effective electrical resistance of a binary metallic composite with random mixture. In mechanical context Budiansky (1965)[21] and Hill (1965)[22] comprehensively developed this approach and applied it on the effective elastic moduli of two-phase composite materials. As has been pointed out by Willis (1981)[23], self-consistent method has various forms to estimate the effective properties of two-phase composites, and effective-medium approach is a specific form in which two constituent phases are on equal geometrical footing. This is in contrast with Mori-Tanaka method that has the inclusion-matrix type of geometry. In effective-medium approach, both constituent phases are considered to be embedded into the effective medium, a conceptual medium whose properties are the same as the effective properties of the composite. This kind of geometry is sometimes more realizable,[24,25] especially when it is hard to identify which phase is the matrix of composites, such as the case of polycrystals.

The effective-medium approach equation adopted in our current study is derived by Weng (2010)[26] with the help of Maxwell's far-field matching of the scattered fields between the two-phase composite and the homogenized effective medium.[27] If we denote the moduli tensor of the reference medium in which the scattered fields of the two-phase composite and the homogeneous effective medium are to be evaluated by $\mathbf{L}_r$, the moduli tensor of the effective medium by $\mathbf{L}_e$, and those of constituent phases 1 and 2 by $\mathbf{L}_1$ and $\mathbf{L}_2$ respectively, then the scattered tensor $\mathbf{T}_i$ of phase *i* can be written as

$$\mathbf{T}_i = \left[\left(\mathbf{L}_i - \mathbf{L}_r \right)^{-1} + \mathbf{S}_i \mathbf{L}_r^{-1} \right]^{-1}, \tag{1.4}$$

where $\mathbf{S}_i$ is the S-tensor of *i*th phase in the reference medium. Now denote the volume concentrations of phase 1 and 2 by c_1 and c_2 respectively, then Maxwell's far-field matching requires that the scattered fields from the effective medium and the sum of scattered fields from two individual phases are equal, which leads to $\mathbf{T}_e = c_1\mathbf{T}_1 + c_2\mathbf{T}_2$, or

$$\left[\left(\mathbf{L}_e - \mathbf{L}_r\right)^{-1} + \mathbf{S}_e\mathbf{L}_r^{-1}\right]^{-1} = c_1\left[\left(\mathbf{L}_1 - \mathbf{L}_r\right)^{-1} + \mathbf{S}_1\mathbf{L}_r^{-1}\right]^{-1} + c_2\left[\left(\mathbf{L}_2 - \mathbf{L}_r\right)^{-1} + \mathbf{S}_2\mathbf{L}_r^{-1}\right]^{-1}. \tag{1.5}$$

In the theory of effective-medium approach, the property of the reference medium $\mathbf{L}_r$ is chosen to be equal to that of the effective medium $\mathbf{L}_e$, so that the scattered field on the left of Eq. (1.5) automatically vanishes. This then leads to the equation for effective-medium approach

$$c_1\left[(\mathbf{L}_1 - \mathbf{L}_e)^{-1} + \mathbf{S}_1\mathbf{L}_e^{-1}\right]^{-1} + c_2\left[(\mathbf{L}_2 - \mathbf{L}_e)^{-1} + \mathbf{S}_2\mathbf{L}_e^{-1}\right]^{-1} = \mathbf{0}. \tag{1.6}$$

The result of effective-medium approach can be obtained by solving this equation for effective property tensor $\mathbf{L}_e$ at any given volume concentration. Unlike M-T method, Eq. (1.6) is a nonlinear, implicit equation, and its solution can be very complicated to evaluate since it involves several rounds of inverse operation on $\mathbf{L}_e$. It is even more complicated if we study anisotropic material property, such as the property of multiferroic composites, as in that case the S-tensors of both constituent phases also depend on the effective property $\mathbf{L}_e$. For these reasons, in general the equation for effective-medium approach can only be solved numerically, and it demands lots of computational efforts to get the solution. This will be demonstrated later in the study of multiferroic composites with 0-0 and 1-1 connectivity.

1.4. Carbon-based nanocomposites

One focus of this micromechanics study is the carbon-based nanocomposites with polymer matrix and carbon nanotubes (CNTs) or graphene nanofillers. The research on CNTs and graphene has been rapidly growing in both physics and material science. Graphene is an allotrope of carbon in the form of a one-atom-thick two-dimensional layer of sp^2-bonded carbon.[28] Each carbon atom is bonded to another three atoms, together forming an atom-scale hexagonal lattice like the shape of honeycomb.[29] Since each carbon atom has 4 outer shell electrons but is only connected to 3 other carbon atoms, one remaining electron is thus highly mobile and available for electrical conduction. The high electrical conductivity of graphene and CNTs is exactly due to the existence of large amount of highly mobile electrons. In the microstructure of graphene, several (less than 10) layers of graphene can stack together to form graphene multilayers, while the manufacturing of monolayer

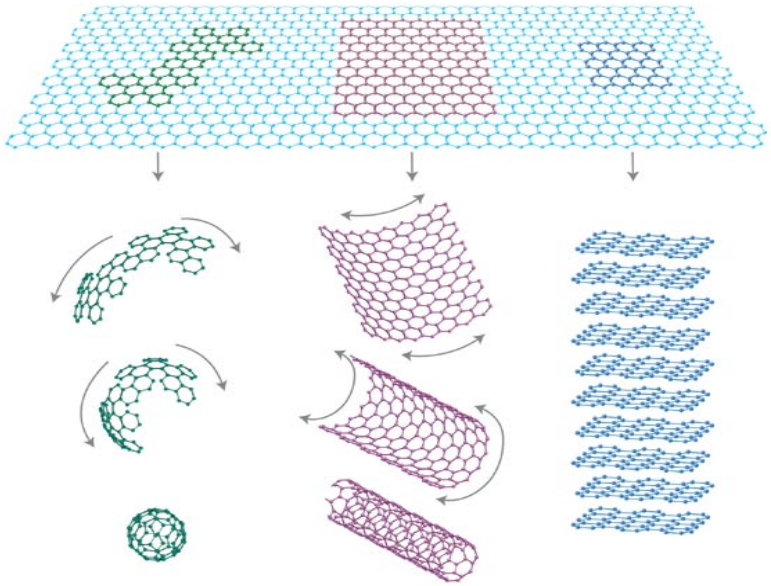

FIG. 1.2. The 2-D graphene can be wrapped up into 0-D fullerenes, rolled up into 1-D CNT or stacked up into 3-D graphite. Reprinted from Geim and Novoselov, Nat. Mater. 6, 183-191 (2007), with permission from Nature Publishing Group through RightsLink.

graphene has also been achieved. The 2-D graphene is the basic structural element of other allotropes of carbon. It can be wrapped up into 0-D fullerenes, rolled up into 1-D CNT or stacked up into 3-D graphite (see Fig. 1.2).[30] On the other hand, CNTs were discovered by Iijima in 1991,[31] which are allotropes of carbon with a cylindrical microstructure and are members of the fullerene structural family. The long, hollow walls of CNTs are formed by rolling up one or several sheets of graphene, which are called single-walled CNTs (SWCNT) or multi-walled CNTs (MWCNT), respectively. The diameters of CNTs range from about 1 nm (for SWCNT) to more than 100 nm (for MWCNT), while their lengths vary from 100 nm (for SWCNT) to about 50 μm (for MWCNT). Therefore from the view of micromechanics, the geometrical structure of CNTs can be modeled as prolate ellipsoids with very high aspect ratios, or long fibers. In contrast, graphene sheets have extremely thin thickness (several nanometers) and large surface area, which can be characterized as oblate ellipsoids with very low aspect ratios, or thin sheets.

Both graphene and CNTs have exceptional material properties in terms of mechanical stiffness and strength, as well as thermal and electrical conductivity. For example, graphene and CNTs are considered as the stiffest and strongest materials ever tested, their Young's modulus could be as high as 270 to 950 GPa for CNTs and 1 TPa for graphene, while their tensile strengths are also phenomenal, about 11 to 63 GPa for CNTs and 130 GPa for graphene. Their thermal conductivity have been measured as 3500 W/(m·K) for CNTs and 1500 to 2500 W/(m·K) for graphene. This can be compared to silver and copper, which are considered as the best thermal

conductors among metal materials, with thermal conductivity of 406 and 385 W/(m·K), respectively. The honeycomb lattice structure also gives CNTs and graphene extraordinary electrical conductivity, which can be as high as 10^6 to 10^7 S/m for CNTs and 10^8 S/m for graphene. This is also comparable to two best kinds of metal conductor of electricity, silver and copper, which have electrical conductivity of 6.30×10^7 and 5.96×10^7 S/m, respectively. In summary, those remarkable properties of CNTs and graphene make them the ideal and promising reinforcements in substantially enhancing the overall properties of the resulting carbon/polymer nanocomposites. Particularly, the enhancement of overall electrical conductivity by carbon fillers will be the key point of our current study.

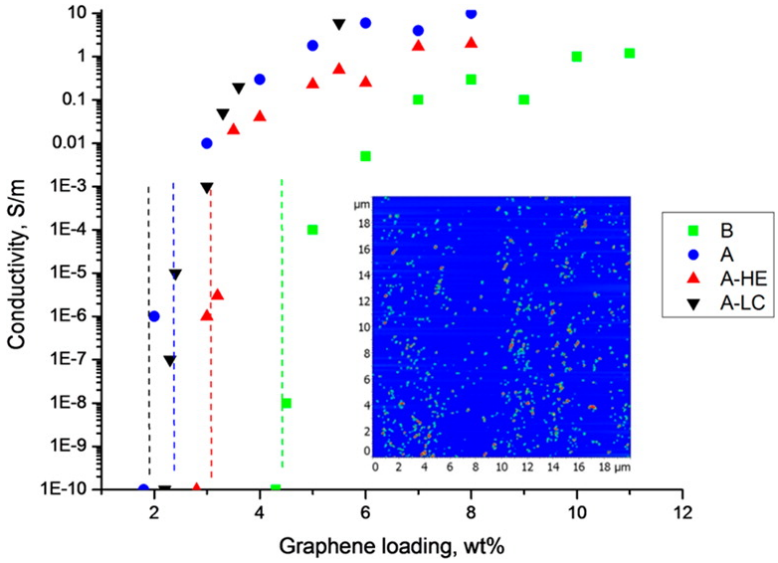

FIG. 1.3. Reproduction of the experimental data of effective electrical conductivity for four samples of graphene-polystyrene nanocomposites. Reprinted with permission from Tkalya *et al.*, ACS Appl. Mater. Interfaces 6, 15113 (2014). Copyright 2014 American Chemical Society.

Carbon-based nanocomposites have a particular percolation phenomenon that their overall electrical conductivity can be dramatically improved at percolation threshold. Moreover, because of their geometrical structures, both CNT and graphene

fillers will result in very low percolation threshold, and this can be observed from lots of reported experimental data.[32] Fig. 1.3 shows four sets of experimental data on the electrical conductivity of graphene nanocomposites. All of them display a sharp increase at about 2 to 4.5 wt.% of graphene, which corresponds to 1 to 2.3 vol.%. The low percolation threshold is a remarkable feature for carbon-based nanocomposites, thus we will focus on developing a theoretical model to evaluate the percolation threshold, and the effective electrical conductivity in our current study.

1.5. Multiferroic composites

Multiferroic composites are a class of composite materials which possess at least two of the three kinds of ferroic properties, i.e., ferroelectricity, ferromagnetism and ferroelasticity. Our current study focuses on the linear behaviors of two ferroic phases, i.e., the piezoelectric and piezomagnetic phase. A piezoelectric phase, such as barium titanate ($BaTiO_3$), lead zirconium titanate (PZT), and lead magnesium titanate-lead titanate (PMT-PT), has the electroelastic coupling between elastic and electric fields. While a piezomagnetic phase has the magnetoelastic coupling between elastic and magnetic fields, such as cobalt ferrite ($CoFe_2O_4$), Terfenol-D, lanthanum strontium manganite (LSMO), and nickel ferrite (NFO). In piezoelectric-piezomagnetic multiferroic composites, the coexistence of two piezo phases will further demonstrate a new magnetoelectric coupling effect, which means applied electric field can induce magnetization, or electric polarization can be generated by applying magnetic field. It can be mathematically described by the magnetoelectric coefficient tensor $\boldsymbol{\alpha}$ (note

this term is not to be confused with the scalar α that represents the aspect ratio of inclusions), which has two components α_{11} and α_{33} for multiferroic composites with transversely isotropic material properties (assuming 3-direction is the axial symmetric direction and 1-2 plane is isotropic). The axial magnetoelectric coupling coefficient, α_{33}, signifies the induced axial magnetization, B_3, under a unit axial electric field, E_3, or conversely, the induced axial electric displacement, D_3, under a unit axial magnetic field, H_3. Likewise, the transverse coupling coefficient, α_{11}, signifies a similar effect in the transverse 1-direction (see Fig. 1.4, also note that 1- and 2-direction are equivalent). This unique effect is considered as the figure of merits for multiferroic composites and makes them highly attractive for applications that

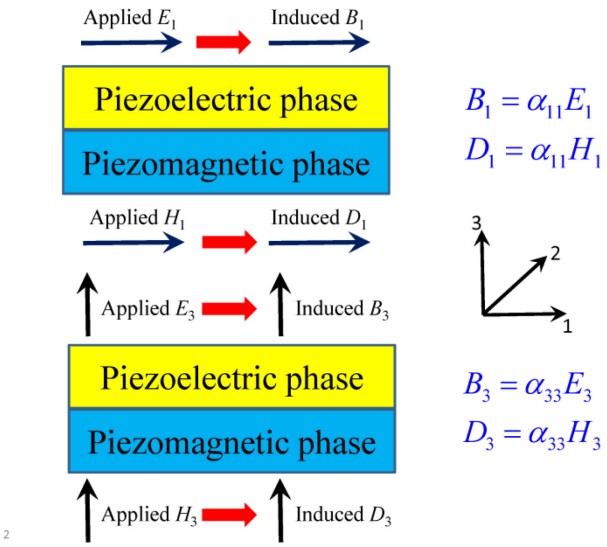

FIG. 1.4. The illustration of magnetoelectric coupling of multiferroic composites, both in 1- and 3- direction.

require the exchange and interaction of mechanical, electrical and magnetic energies. Besides it is also useful in sensors, actuators, transducers, and high-frequency devices whose properties need to be tuned electrically or magnetically.

Magnetoelectric coupling effect was first proposed by van Suchtelen in 1972.[33] It

does not exist in any single piezoelectric or piezomagnetic phase, rather it is only owned by the overall composite due to the electro-magneto-elastic coupling of two piezo phases. Specifically, piezomagnetic effect relates magnetic field to mechanical strain in the piezomagnetic phase, while piezoelectric effect connects mechanical stain to electric field in the piezoelectric phase. As a result, electric and magnetic field are coupled via the compatibility of the strain fields of two phases, therefore only the overall multiferroic composites can demonstrate such magnetoelectric coupling effect. The magnetoelectric coefficient α_{11} and α_{33} depend on many factors of two constituent phases, such as their material properties, volume concentrations, inclusion shape and phase connectivity. Among them phase connectivity illustrates the number of dimensions through which a phase is continuous. Following the notation by Newnham *et al.*,[34] it is represented as a combination of two numbers "*a*-*b*". The number *a* and *b* can be 0, 1, 2 or 3, which may be interpreted as the shape of 0-D particle, 1-D cylinder, 2-D plane and 3-D body, respectively. Hence there are 10 different types of connectivity in total. Phase connectivity also indicates the geometrical structures of multiferroic composites. For instance, the most commonly seen 0-3, 2-2 and 1-3 connectivity correspond to particulate, laminate and fibrous composites, respectively. Multiferroic composites with different types of connectivity must be addressed by different micromechanics approaches. Our current study covers 5 types of connectivity. For 0-3, 2-2 and 1-3 connectivity, they have the typical inclusion-matrix type of microstructures, and thus are studied by Mori-Tanaka method. On the other hand, 0-0 and 1-1 connectivity are examined via

effective-medium approach, since both constituent phases have the same geometrical footing.

Early works on 0-3 composites can be traced back to the square-block model of Harshé *et al.*[35] and the Green's function approach of Nan,[15] while for 1-3 fibrous composites it can be attributed to Benveniste,[36] and for 2-2 multilayers to Avellaneda and Harshé.[37] In principle 0-3, 1-3, and 2-2 connectivity can all be studied in a unified fashion, that aligned spheroidal piezomagnetic (or piezoelectric) inclusions are embedded in a homogeneous piezoelectric (or piezomagnetic) matrix. By taking the aspect ratio of the spheroidal inclusions as 1, ∞ and 0 respectively, these three types of connectivity can all be recovered. Such an approach has been taken in Nan's seminal work,[15] and also in the works of Huang and Kuo,[17] Li and Dunn,[18] and Srinivas *et al.*[38] Direct considerations of 2-2 and 1-3 connectivity have also been given by Bichurin *et al.*,[39] Wang *et al.*,[40] Liu and Kuo,[41] Kuo and Bhattacharya,[42] Chen *et al.*,[43] and Liu *et al.*[44] All of them have greatly contributed to our current understanding of magnetoelectric coupling in 0-3, 1-3, and 2-2 connectivity. While these three types of connectivity have received extensive investigations, 0-0 and 1-1 connectivity have not. Their geometrical setting, that both two ferroic phases exist on equal geometrical footing, requires totally different theoretical principles to determine their effective properties. In this study, we will use effective-medium approach in the piezoelectric-piezomagnetic context with a novel incremental scheme, to address these two types of connectivity and numerically solve for their effective properties.

Chapter 2.

Carbon nanotube-based nanocomposites

2.1. Overview

As mentioned above, carbon nanotubes (CNTs) have very high electrical conductivity and high aspect ratio, whereas polymers are almost insulating. From the continuum perspective, the prediction of the effective conductivity of CNT-based nanocomposites is thus a high-contrast and high-aspect ratio problem, which is difficult in general. This task is further compounded with many complicated microstructural and physical issues, such as the interface condition between CNTs and polymer. For this reason, it is not easy to develop a continuum model with a sufficiently simple framework but can still be widely useful. To be more specific, the axial electrical conductivity of CNTs is usually on the orders of 10^3 to 10^5 S/m, and for metallic multi-walled CNTs it can be as high as 10^6 to 10^7 S/m.[45] In contrast, the conductivity of most polymers is on the orders of 10^{-15} to 10^{-8} S/m. This makes the contrast of their conductivity on the orders of 10^{12} to 10^{18}. This is a dramatic change from the classical problem of effective elastic moduli in fiber-reinforced composites where the property contrast is usually within the order of 10^2. But the high contrast problem also offers high opportunity, and it is known that, even with a very low CNT loading, the electrical conductivity of CNT-based nanocomposites can be greatly enhanced. For instance, Gardea and Lagoudas reported a remarkable 10 orders of magnitude increase in electrical conductivity for pristine CNT/epoxy composite

relative to the neat epoxy, at 0.1 wt.% CNT concentration.[46] Due to the high aspect ratio of CNTs, this class of composites tends to possess a percolation threshold at very low filler concentration. Over a very narrow range near the percolation threshold, the effective electrical conductivity rises sharply, from almost insulating to highly conductive. This well-known percolation phenomenon is a fundamental characteristic for the electrical conductivity of CNT-based nanocomposites.[47-50] It is a result of many possible contributions, such as CNT geometry, the formation of percolating networks, and electron tunneling.[51-53]

The CNT problem involves two major issues: (i) the determination of the percolation threshold, and (ii) the determination of the overall electrical conductivity. Due to the complex CNT geometry and electron tunneling process, Monte Carlo (MC) simulations have often been invoked to investigate this class of problems.[54-56] MC simulations have provided significant insights into the microscopic processes but are highly computational. Our approach here is not so computational; instead we seek to develop a continuum model that could have both simplicity and wide applicability. The model is intended to embody the three most essential features of the conduction processes for the nanocomposites. In this regard, we will consider the issues of percolation threshold, interface effect, and electron tunneling effect. The issue of electron tunneling is of quantum nature and is difficult to simulate in a continuum fashion, but we still plan to include it in a phenomenological way so that its effect will not be completely lost. It will be shown that our model involves only very limited number of input parameters, such as the intrinsic electrical conductivity of CNTs and

the matrix, CNT aspect ratio and volume concentration, interfacial resistance, and parameters that characterize the tunneling-assisted interfacial conductivity in a statistical fashion. We also demonstrate that the theoretical predictions of our model can be easily connected with the macroscopically measured experimental data.

2.2. The theory

2.2.1. Effective electrical conductivity

The microstructure of CNT-based nanocomposites can be abstracted as a two-phase composite model, with CNTs as inclusion phase and polymer as the matrix. CNT inclusions are regarded as long, prolate ellipsoids with high aspect ratio (more than 10). Compared with the cylindrical CNT model, a prolate spheroidal CNT will possess almost the same shape when its aspect ratio is sufficiently large, as is usually the case. The dispersion of CNT inclusions is considered homogeneous and their orientations are totally random. This microstructure is shown in Fig. 2.1. As the

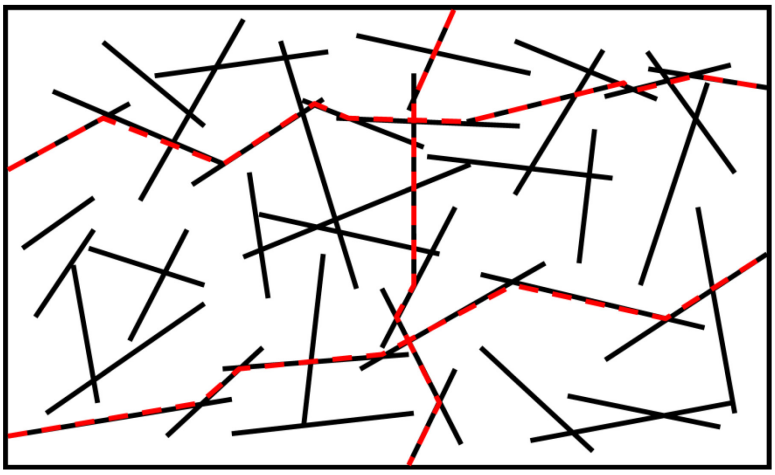

FIG. 2.1. Microstructure of CNT-based nanocomposites, showing CNTs (black solid line) in the effective medium and three percolating paths (one vertical and two horizontal, in red dashed line).

volume concentration of CNT inclusions increases, it becomes possible for CNTs to have contact with each other. Those contacted CNTs will form percolating paths and all paths together will become a conductive network, so that electrical current can flow in this network without having to bypass the insulating matrix. The formation of conductive network is exactly the percolation phenomenon at the macroscopic scale. To study this phenomenon in micromechanics theory, we consider to implement the effective-medium approach with its 3-D random version, since CNTs are randomly oriented. Denoting the orientational average of a tensor by angular bracket $\langle\ \rangle$, the 3-D random effective-medium approach can be written as

$$\begin{aligned} &c_0\langle \mathbf{T}_0\rangle + c_1\langle \mathbf{T}_1\rangle = \mathbf{0} \quad \text{or} \\ &c_0\left\langle \left[(\mathbf{L}_0-\mathbf{L}_e)^{-1}+\mathbf{S}_0\mathbf{L}_e^{-1}\right]^{-1}\right\rangle + c_1\left\langle \left[(\mathbf{L}_1-\mathbf{L}_e)^{-1}+\mathbf{S}_1\mathbf{L}_e^{-1}\right]^{-1}\right\rangle = \mathbf{0}, \end{aligned} \tag{2.1}$$

where subscript 0 denotes the polymer phase, and 1 denotes the CNT phase. The moduli tensor of the polymer matrix $\mathbf{L}_0$ is taken to be isotropic, with electrical conductivity σ_0 in all three directions; while the moduli of CNT inclusion $\mathbf{L}_1$ is transversely isotropic, with axial electrical conductivity σ_3 and transverse electrical conductivity $\sigma_1 = \sigma_2$. In general, σ_3 is substantially higher than σ_1, so that the latter can be expressed as $\sigma_1 = m\sigma_3$, with $m \le 1$. Due to the random orientation of CNT inclusions, the overall electrical conductivity of the nanocomposite should be isotropic in nature, therefore the moduli tensor of the effective medium $\mathbf{L}_e$ carries effective electrical conductivity σ_e in all three directions. $\mathbf{S}_1$ is the electric S-tensor for CNT inclusion phase, which is also transversely isotropic. The three diagonal components of $\mathbf{S}_1$ depend on the aspect ratio of CNT α only, since the

effective medium is isotropic. Taking 3-direction as the symmetric axis of the CNT ellipsoids, they can be explicitly expressed as

$$S_{11} = S_{22} = \begin{cases} \dfrac{\alpha}{2\left(1-\alpha^2\right)^{\frac{3}{2}}}\left[\cos^{-1}\alpha - \alpha\left(1-\alpha^2\right)^{\frac{1}{2}}\right], & \alpha < 1 \\ \dfrac{\alpha}{2\left(\alpha^2-1\right)^{\frac{3}{2}}}\left[\alpha\left(\alpha^2-1\right)^{\frac{1}{2}} - \cosh^{-1}\alpha\right], & \alpha > 1 \end{cases} \tag{2.2}$$

and $S_{33} = 1 - 2S_{11}$. For prolate shape CNTs, their aspect ratios should always be larger than 1, and $0 < \alpha < 1$ corresponds to oblate spheroid such as the shape of graphene. When $\alpha \to \infty$ (long fiber), these components are reduced to $S_{11} = S_{22} = 1/2$ and $S_{33} = 0$; and when $\alpha \to 0$ (thin plate), they are reduced to $S_{11} = S_{22} = 0$ and $S_{33} = 1$. For spherical inclusion, $\alpha = 1$ and each component is 1/3. $\mathbf{S}_0$ on the other hand is the electric S-tensor for the polymer matrix phase. In view of the isotropic nature of the effective medium, the "effective" shape of the matrix could be envisioned to be spherically symmetric so that $\mathbf{S}_0$ carries the same diagonal components of 1/3 in all three directions.

It is also recognized that most CNTs are curly in reality; but to present our theory in a simple and analytical form, it is necessary to idealize CNTs as straight. This idealization to some extent could be justified that, in the 3-D randomly oriented setting a curly CNT could be thought as two distinct segments with two different orientations having contact with each other. Since effective-medium approach permits CNTs to be in contact, the problem of curly CNTs can also be addressed by the 3-D random effective-medium approach as Eq. (2.1). The calculation of orientational average of a tensor is presented in Appendix A. In the context of electrical

conductivity, all the property tensors are second-order. For any second-order tensor, its orientational average is given by the mean of three diagonal components times the second-order identity tensor δ_{ij}. Therefore Eq. (2.1) can be simplified to a scalar equation

$$c_0 \overline{\mathrm{T}}_0^e + c_1 \overline{\mathrm{T}}_1^e = 0 \tag{2.3}$$

where the bar symbol denotes the orientational average value, and a superscript *e* is added to signify that both two phases are embedded in the effective medium. $\overline{\mathrm{T}}_0^e$ and $\overline{\mathrm{T}}_1^e$ are given as

$$\overline{\mathrm{T}}_0^e = \frac{1-n_e}{n_e + (1/3)(1-n_e)} \quad \text{and} \quad \overline{\mathrm{T}}_1^e = \frac{1}{3}\left[\frac{2(1-n_e)}{n_e + S_{11}(n_1 - n_e)} + \frac{n_3 - n_e}{n_e + S_{33}(n_3 - n_e)}\right] \tag{2.4}$$

where $n_1 = \sigma_1/\sigma_0$ and $n_3 = \sigma_3/\sigma_0$ are the axial and transverse electrical conductivity of CNTs in their normalized forms. We can solve this implicit equation for n_e, which equals to σ_e/σ_0, for the normalized effective electrical conductivity of the nanocomposite. The result with isotropic CNT conductivity can be obtained simply by setting $n_1 = n_3 \equiv n$.

To explain why effective-medium approach is selected as the backbone of our continuum model, we make a comparison among three different micromechanics approaches, including effective-medium approach, M-T method, and Ponte Castañeda-Willis (PCW) method.[57] PCW method was also first developed in the mechanical setting, and it was Duan *et al.*[58] who made it explicit in the thermal conduction context. Pan *et al.*[59] have suggested the combination of PCW method at low CNT concentration and Hashin-Shtrikman (H-S)[60] upper bound at high CNT concentration to model the effective electrical conductivity of CNT nanocomposites

over a wide range of concentration. H-S bounds have been widely used as the upper and lower limit for the effective properties of composite materials. Any valid estimation of effective properties should not violate these two bounds, therefore it is helpful to examine these three approaches in the light of H-S bounds. In the setting of electrical conductivity problem with isotropic CNTs and polymer matrix, the results of M-T and PCW method can be written as

$$\frac{\sigma_e^{\mathrm{MT}}}{\sigma_0}=1+\frac{c_1\overline{\mathrm{T}}_1^0}{1-c_1\left[1-\overline{\mathrm{T}}_1^0/(n-1)\right]} \quad \text{and} \quad \frac{\sigma_e^{\mathrm{PCW}}}{\sigma_0}=1+\frac{c_1\overline{\mathrm{T}}_1^0}{1-c_1\overline{\mathrm{T}}_1^0/3}, \tag{2.5}$$

where superscript 0 means that unlike effective-medium approach, in M-T and PCW method CNT inclusions are directly embedded in the polymer matrix, so that

$$\overline{\mathrm{T}}_1^0=\frac{n-1}{3}\left[\frac{2}{1+(n-1)S_{11}}+\frac{1}{1+(n-1)S_{33}}\right]. \tag{2.6}$$

It can be easily proved that, when aspect ratio $\alpha=1$, both formulas in Eq. (2.5) will return to Maxwell's original formula for a system with uniform suspensions of spherical particles.[61] On the other hand, considering that CNT is much more conductive than polymer ($\sigma_1 \gg \sigma_0$), the lower and upper H-S bounds[60] are respectively given by

$$\begin{aligned}\frac{\sigma_e^{\mathrm{HS}(-)}}{\sigma_0}&=1+\frac{c_1(n-1)}{(1/3)(1-c_1)(n-1)+1},\\ \frac{\sigma_e^{\mathrm{HS}(+)}}{\sigma_0}&=1+\frac{(1-c_1)(1-n)}{(1/3)c_1(1-n)+n}.\end{aligned} \tag{2.7}$$

Using the normalized electrical conductivity $n=\sigma_1/\sigma_0=10^{10}$ and aspect ratio $\alpha=20$ for the properties of CNTs, we have plotted the results of effective electrical conductivity in Fig. 2.2 in a log-scale for these three methods. It is seen that the PCW

result quickly goes out of the H-S upper bound, at a CNT volume concentration of

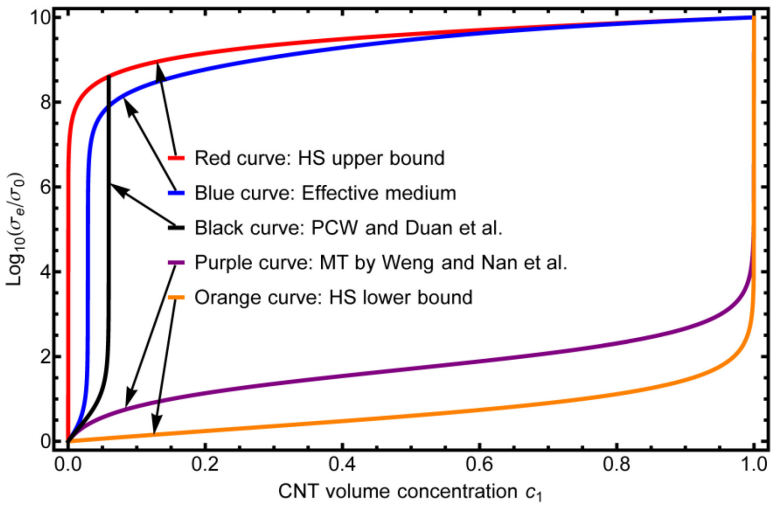

FIG. 2.2. Examination of the effective-medium approach, Mori-Tanaka method (1973) by Weng (1984, 1990) and Nan *et al.* (1997), and Ponte Castañeda-Willis method (1995) by Duan *et al.* (2006), in light of the Hashin-Shtrikman (1962) bounds.

$c_1 < 0.1$. In strict applications, this theory is limited to the range $c_1 < 1/\alpha^2$, which is 0.0025 here, but it can go a bit higher before it hits the upper bound. This shows that PCW method cannot properly yield the effective electrical conductivity over the entire range of c_1. In fact it is originally developed in mechanical setting, in which the elastic properties of inclusion and matrix phase have very little contrast (usually less than 10 times). But the electrical conductivity is an extremely high-contrast problem, which would cause the PCW result to have singularity at certain value of c_1. Therefore PCW method is not suitable to account for a high-contrast problem. Both effective-medium and M-T results are seen to stay within the bounds, but the M-T result has no early percolation feature. Its curve stays rather flat at low CNT concentration and only when c_1 approaches 1 does it start to grow rapidly, which is close to the trend of H-S lower bound. Only the effective-medium result displays a sharp increase at low CNT concentration and possesses a percolation threshold, which

is like the behavior of H-S upper bound but is still always lower than it. In the microstructure of CNT nanocomposites, since large amount of CNTs are contacted with each other to form a conductive network, the CNT inclusions cannot be considered to be directly "embedded" in the polymer matrix any more. They are rather embedded in the effective medium, and therefore effective-medium approach has been chosen to study the effective electrical conductivity.

2.2.2. Percolation threshold

The determination of percolation threshold of CNT-based nanocomposites has been extensively studied by different approaches. Numerical approach such as MC simulation has been a popular tool in the study of percolation threshold. But the computational cost of MC simulation is so high, that a simple analytical result is more desirable. Some theoretical works have focused on geometric method. For instance, Balberg *et al.*[62] considered 3-D randomly oriented sticks combined with their associated average excluded volume, Bao *et al.*[63] randomly generated cylinder models in representative volume and proposed a percolating network recognition scheme with periodic boundary conditions, and Chatterjee[64] used a polydisperse system of rods with the help of Bethe lattice site percolation model. All these methods are insightful, but when the percolation threshold has to be borrowed from other theory, it implies that the proposed CNT nanocomposites model is not self-contained to be able to cover both effective electrical conductivity and percolation threshold simultaneously. This is an issue that we want to avoid. And next it will show that in our continuum model,

percolation threshold is an integral part that can be directly derived from the effective-medium approach.

The effective electrical conductivity, σ_e, is given by solving the following equation,

$$c_0 \frac{\sigma_0 - \sigma_e}{\sigma_e + (1/3)(\sigma_0 - \sigma_e)} + c_1 \frac{1}{3}\left[\frac{2(\sigma_1 - \sigma_e)}{\sigma_e + S_{11}(\sigma_1 - \sigma_e)} + \frac{\sigma_3 - \sigma_e}{\sigma_e + S_{33}(\sigma_3 - \sigma_e)} \right] = 0, \quad (2.8)$$

which is equivalent to Eq. (2.3) except all the electrical conductivity terms have not been normalized. Eq. (2.8) can further be used to determine the percolation threshold of the nanocomposite, c_1^*. This is done with the observation that, when the matrix phase is totally insulating ($\sigma_0 = 0$), the effective electrical conductivity is entirely controlled by the CNT conductive networks, so the CNT volume concentration c_1 that first gives rise to a non-negative value of σ_e represents the percolation threshold, c_1^*. With $\sigma_0 = 0$, Eq. (2.8) turns into a quadratic equation for σ_e, in the following form

$$\mathrm{A}\sigma_e^2 + \mathrm{B}\sigma_e + \mathrm{C} = 0, \quad (2.9)$$

with coefficient A, B and C all being functions of c_1, as

$$\begin{aligned}
&\mathrm{A} = 9\left(1 - S_{33}^2\right) + c_1\left(1 - 3S_{33}\right)^2, \\
&\mathrm{B} = \sigma_1\left[-3c_1\left(1 - S_{33}\right)\left(5 - 3S_{33}\right) + 9\left(1 - S_{33}\right)^2 \right] + \sigma_3\left[-c_1\left(9S_{33}^2 + 3S_{33} + 2\right) + 9S_{33}\left(1 + S_{33}\right) \right], \\
&\mathrm{C} = \sigma_1\sigma_3\left[-c_1\left(-9S_{33}^2 + 15S_{33} + 2\right) + 9S_{33}\left(1 - S_{33}\right) \right],
\end{aligned} \quad (2.10)$$

where the relation $2S_{11} + S_{33} = 1$ has been used. As c_1 increases from zero, initially all three coefficients are positive, so there is no positive solution for σ_e at very low c_1. When c_1 increases to a critical value, there is a solution of $\sigma_e = 0$, and as it

further increases there is a finite positive value of σ_e corresponding to each c_1. This is the generally sought effective electrical conductivity of the CNT-based nanocomposites with a perfectly insulating matrix, whereas the critical value of c_1 giving rise to $\sigma_e = 0$ is exactly the percolation threshold, c_1^*. This occurs when coefficient $\mathrm{C} = 0$, and this relation provides the value

$$c_1^* = \frac{9S_{33}(1-S_{33})}{-9S_{33}^2 + 15S_{33} + 2}. \tag{2.11}$$

Since the S-tensor component S_{33} only depends on inclusion aspect ratio α, the percolation threshold is thus a strictly geometrical parameter. To see its effects, we have plotted its dependence on α in Fig. 2.3, as α increases from almost 0 (graphene-like) to infinity (CNT-like). For carbon-based nanocomposites, the percolation thresholds with extreme values of α are further illustrated in the insets. One can see that CNTs provide a lower percolation threshold than graphene with reciprocal aspect ratio. This is also consistent with the result predicted by Pan *et al*.[65]

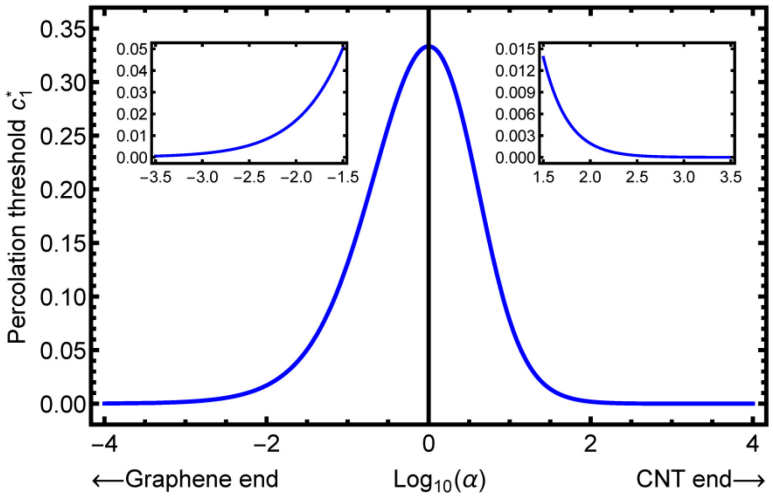

FIG. 2.3. Dependence of the percolation threshold on the inclusion aspect ratio. The left-hand side is the graphene side while the right-hand side is the CNT side.

It can be seen the maximum value that c_1^* can attain is exactly 1/3, which

corresponds to spherical particle inclusion with $\alpha = 1$. This value has been widely reported in other literature.[62,66]

The percolation threshold c_1^* can also be determined from Eq. (2.8) following a procedure suggested by Gao and Li.[67] In general, the matrix is almost insulating while CNTs are highly conducive. Therefore σ_i ($i = 1$ or 3, the same below) are usually several orders of magnitude higher than σ_0, which makes $\sigma_0/\sigma_i \to 0$. According to the percolation theory, when CNT concentration $c_1 < c_1^*$, σ_e has almost the same order of magnitude as σ_0, therefore $\sigma_e/\sigma_i \to 0$; but after c_1^*, σ_e will quickly approach σ_i, making $\sigma_e/\sigma_0 \to \infty$. Therefore at $c_1 = c_1^*$, σ_e is at the transition stage, satisfying both $\sigma_e/\sigma_0 \to \infty$ and $\sigma_0/\sigma_i \to 0$ at the same time. Applying these two conditions to Eq. (2.8) and solving for c_1^*, one finds

$$c_1^* = \frac{3/(1-S_0)}{3/(1-S_0)+1/S_{11}+1/S_{22}+1/S_{33}} = \frac{9S_{33}(1-S_{33})}{-9S_{33}^2+15S_{33}+2}, \tag{2.12}$$

which is exactly the same result as Eq. (2.11).

2.2.3. Interfacial resistance

We now consider the interface effect on the effective electrical conductivity. Eq. (2.1) is derived based on the assumption of perfect interface between CNT and polymer phases, but in reality the interface condition is never perfect and interface effect is inevitable. The issue of imperfect interface has a longer history in the study of thermal conductivity. Notable contributions include the works of Dunn and Taya,[68] Nan *et al.*,[13] and Hashin,[69] among others. The effect of imperfect interface results in electrical resistance between two phases, which is the interfacial resistance and will

make the transport of electric current more difficult. Without this additional consideration the calculated σ_e could be much higher than the actual value. To address this issue, we first consider the existence of a very thin spheroidal layer of interphase by adding a tiny thickness *t* to the semi-axes of the CNT inclusion, with an electrical conductivity σ_i^{int}. This layer is taken to surround the spheroidal CNT, making it similar to a "thinly coated" CNT. Due to the imperfect condition, σ_i^{int} is usually much lower than the intrinsic conductivity of CNTs, σ_i, so that it is reasonable to assume $\sigma_i^{\text{int}}/\sigma_i \to 0$. Compared to the radius of CNT, *R*, thickness *t* is taken to be diminishingly small and we intend to make it approach zero to turn the interphase into an interface. In the limiting case of diminishing thickness ($t \to 0$), the "coated" CNT and the original CNT share the same shape, or the same S-tensor. This is a typical inclusion-matrix type of problem, therefore M-T method is appropriate to calculate the overall electrical conductivity of the coated inclusion, σ_i^c, as

$$\sigma_i^c = \sigma_i^{\text{int}}\left[1+\frac{\nu\left(\sigma_i-\sigma_i^{\text{int}}\right)}{\left(1-\nu\right)S_{ii}\left(\sigma_i-\sigma_i^{\text{int}}\right)+\sigma_i^{\text{int}}}\right], \tag{2.13}$$

where $i=1$ or 3 (no sum over *i* in S_{ii}), denoting the transverse or axial direction. And ν is the volume fraction of the original CNT in the coated CNT, given by $\nu = LR^2/\left[\left(L+t\right)\left(R+t\right)^2\right]$, where *L* is the half length of CNT satisfying $L=\alpha R$. By taking the limit $t \to 0$, ν can be simplified to

$$\nu \approx 1-\left(\frac{1}{\alpha}+2\right)\frac{t}{R}. \tag{2.14}$$

Then, with the assumption $\sigma_i^{\text{int}}/\sigma_i \to 0$, Eq. (2.13) can be rewritten as

$$\sigma_i^c = \frac{\sigma_i}{1+\rho_i\sigma_i S_{ii}\left(1/\alpha+2\right)/R}, \tag{2.15}$$

where $\rho_i = \lim_{\sigma_i^{\text{int}}/\sigma_i \to 0,\, t \to 0} t/\sigma_i^{\text{int}}$ stands for the interfacial resistivity in axial or transverse direction. For simplicity, it's convenient to take the property of interface to be isotropic, so that $\rho_i = \rho$. This result is also consistent with the Kapitza resistance in thermal conductivity derived by Nan *et al.*[13] and Duan and Karihaloo.[70] This electrical conductivity of coated CNT, σ_i^c, can then be used to replace the original σ_i in Eq. (2.8) of effective-medium approach to calculate the effective electrical conductivity of imperfectly bonded nanocomposites. In this way, the effect of interfacial resistance has been incorporated into our model.

2.2.4. Tunneling-assisted interfacial conductivity

The interfacial resistivity ρ is an intrinsic property of the interface between CNTs and the polymer matrix, and we denote its intrinsic value as ρ_0. This quantity contributes to the effective electrical conductivity of the coated CNT, σ_i^c, through Eq. (2.15). However as the volume concentration of CNT c_1 increases, ρ cannot remain constant at ρ_0. In CNT nanocomposites, we note that electron hopping from one CNT to the surface of another CNT can lead to enhanced electrical conductivity. This phenomenon, that electrons can directly pass though insulating polymer from one CNT to an adjacent one, is the quantum mechanical tunneling effect. The outcome is a higher interfacial conductivity, or conversely, a lower interfacial resistivity. It plays an essential role the electrical conduction process, but it is also difficult to analyze due to its quantum mechanical nature.

In our continuum model we take this tunneling effect as a statistical process that

depends on the volume concentration of CNTs. In establishing a probabilistic function, we note that, at dilute CNT concentration, the distance between CNTs is large and there is little tunneling possibility, so there is large interfacial resistivity; but around the percolation threshold c_1^*, CNT conductive networks begin to build up and the overall distance between CNTs is greatly reduced. As a consequence electron tunneling activity starts to become very intense and ρ begins to decrease. After c_1^*, the distance between CNTs will get even closer and thus tunneling effect will continue to be at a very high level, while ρ will stay very low. It turns out that Cauchy's probabilistic model is particularly suited to describe this phenomenon. We will incorporate Cauchy's cumulative distribution function, *F*, that can signify the dramatic increase of interfacial conductivity near c_1^*, to describe this tunneling effect. This function is given by

$$F\left(c_1; c_1^*, \gamma\right) = \frac{1}{\pi}\arctan\left(\frac{c_1 - c_1^*}{\gamma}\right) + \frac{1}{2}, \tag{2.16}$$

where γ is a scale parameter denoting the rate of change for function *F* around $c_1 = c_1^*$. The nature of function *F* is illustrated in Fig. 2.4 with $c_1^* = 0.023$ and $\gamma = 0.001$. It displays a sharp increase around c_1^* and continues to hold afterward. With function *F*, the decrease of interfacial resistivity ρ from ρ_0 as c_1 increases can be described by

$$\rho = \rho\left(c_1\right) = \rho_0\left[F\left(1; c_1^*, \gamma\right) - F\left(c_1; c_1^*, \gamma\right)\right] \Big/ \left[F\left(1; c_1^*, \gamma\right) - F\left(0; c_1^*, \gamma\right)\right]. \tag{2.17}$$

This c_1-dependent ρ is the tunneling-assisted interfacial resistivity, which returns to $\rho = \rho_0$ at $c_1 = 0$. The nature of its variation is illustrated in Fig. 2.5 which shows a drastic decrease of interfacial resistivity around c_1^*.

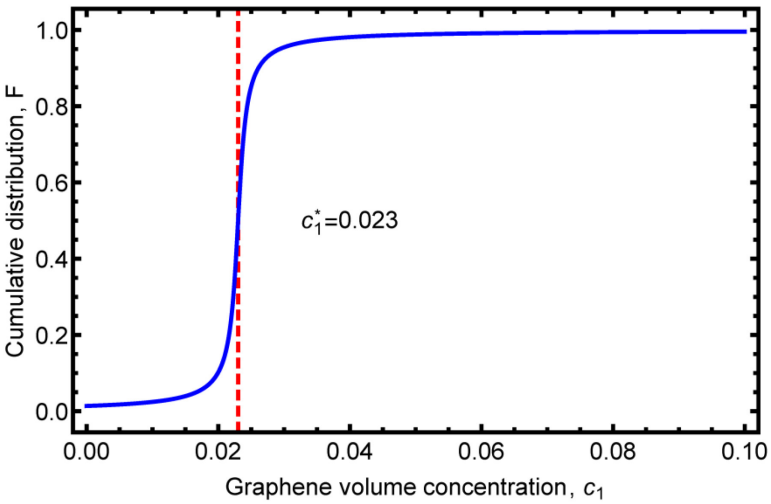

FIG. 2.4. The illustration of Cauchy's cumulative distribution function in Eq. (2.16), showing an increasing tunneling activity near the percolation threshold.

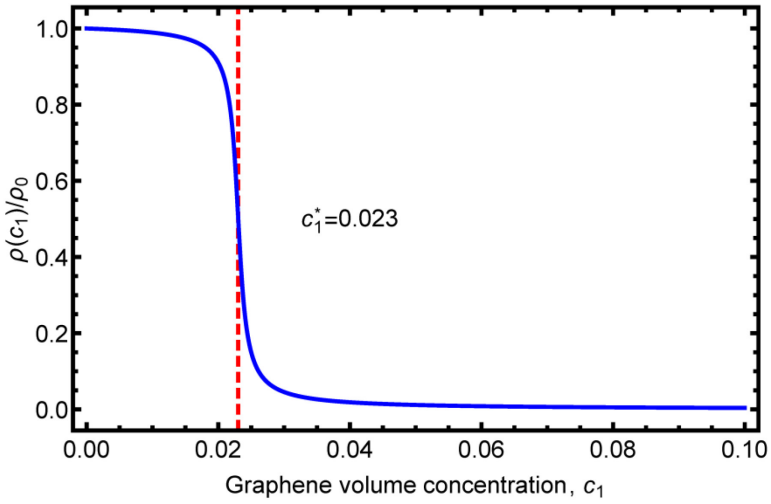

FIG. 2.5. The illustration of tunneling-assisted interfacial resistivity in Eq. (2.17), which leads to a sharp drop in resistivity near the percolation threshold.

This tunneling-assisted interfacial resistivity now should replace the original interfacial resistivity in Eq. (2.15) to calculate the electrical conductivity of the coated CNT σ_i^c, which in turn will replace σ_i in Eq. (2.8) for the effective electrical conductivity, σ_e, of CNT-based nanocomposites. In this way, the influence of electron tunneling effect is mathematically described by the tunnel-assisted interfacial resistivity ρ, and has been incorporated into our continuum model. Up to this point we have completed the development of our continuum model for CNT-based

nanocomposites, we will then present some calculated results and make comparisons with experimental data.

2.3. Results and discussion

To verify our continuum model, two sets of experimental data by Ngabonziza *et al*.[71] and McLachlan *et al*.[72] showing notable percolation phenomena are studied. The first set of data involved a multi-walled CNTs in polyimide matrix, while the second set was with single-walled CNTs and also polyimide matrix. The intrinsic electrical conductivity of CNTs and the matrix were both given in the original papers and are listed in Table I. In our calculations the anisotropic constant m, in $\sigma_1 = m\sigma_3$, for the CNTs is assumed to be 0.001 at this moment. All other relevant material constants used in the calculations are also listed here.

Table I. Physical values used in the calculation of effective electrical conductivity.

Physical values	Ngabonziza *et al.*, 2011	McLachlan *et al.*, 2005
σ_0	2.0×10^{-8} S/m	5.5×10^{-15} S/m
σ_3	1.943×10^{4} S/m	8.9×10^{3} S/m
σ_3/σ_0	9.715×10^{11}	1.8×10^{18}
m	10^{-3}	10^{-3}
Percolation threshold	0.0266	0.005
Aspect ratio α	21	213
CNT radius R	5 nm	5 nm
Interfacial resistivity ρ_0	4.82×10^{-8} m^2/S	7.16×10^{-4} m^2/S
Scale parameter γ	0.003	0.0003

2.3.1. Effective electrical conductivity of the coated CNT

With this Cauchy's cumulative distribution function F, we then use Eq. (2.15) to calculate the increase of the effective electrical conductivity of coated CNT, σ_i^c, as

c_1 increases, to reflect the contribution from the probabilistic electron tunneling process. The results with these two sets of experimental data are shown in Fig. 2.6(a) and 2.6(b), respectively, where the upper blue curves are for the axial electrical conductivity and the lower red ones for the transverse electrical conductivity. These two sets of data have substantially different percolation thresholds, one at 0.0266 and the other at 0.005. So the initial, nearly horizontal portion spans over a wider range of c_1 in the first set, but following the percolation threshold, both curves display a notable increase due to the stronger electron tunneling effect associated with the conductive network formation.

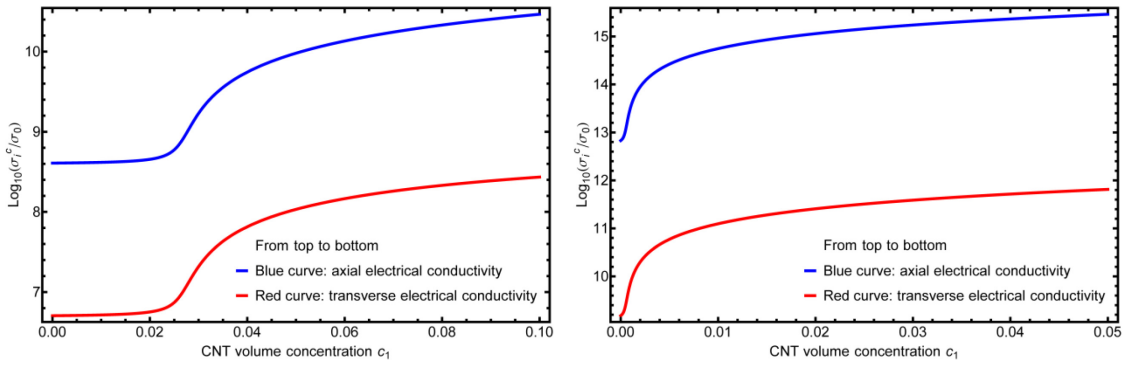

FIG. 2.6. Electrical conductivity of the coated CNT with the consideration of interfacial resistance and tunneling-assisted interfacial conductivity: (a) by Ngabonziza *et al.* (2011) data, and (b) by McLachlan *et al.* (2005) data.

This characteristic can be made more apparent if we rewrite Eq. (2.15) as

$$\sigma_i^c = \frac{1}{1/\sigma_i + \rho(c_1) S_{ii} (1/\alpha + 2)/R}. \tag{2.18}$$

It can be observed that, when $c_1 < c_1^*$, the numerical value of $\rho(c_1) S_{ii} (1/\alpha + 2)/R$ is much larger than $1/\sigma_i$. So in this case the latter can be neglected and we have, approximately, $\sigma_i^c = R/\left[\rho(c_1) S_{ii} (1/\alpha + 2)\right]$, which means that σ_i^c is now mainly controlled by the interfacial resistivity, rather than the intrinsic electrical conductivity

of CNT. As such, the several-orders-of-magnitude difference between the axial conductivity σ_3^c and the transverse conductivity σ_1^c, is only a result of the different components in the S-tensor. S-tensor characterizes the geometric property of CNT, which has a prolate spheroidal shape. Comparing Fig. 2.6(a) to 2.6(b), it can be further pointed out that the higher aspect ratio in the second data set also leads to larger difference between σ_3^c and σ_1^c. Therefore we can conclude that the geometry of CNTs plays a very important role in the anisotropy of σ_i^c.

2.3.2. Effective electrical conductivity of CNT nanocomposites

With the c_1-dependent σ_i^c to replace the original σ_i in Eq. (2.8), the effective electrical conductivity of CNT nanocomposites, σ_e, can be calculated as a function of CNT concentration c_1. The results are plotted in Fig. 2.7 and 2.8, that correspond to the experiment results of Ngabonziza *et al.* and McLachlan *et al.*, respectively.

In both figures the highest red curve represents the calculated result under the assumption of perfect interface between CNTs and the matrix. It is seen that, without accounting for the interfacial resistance, the theoretical predictions are substantially higher than the experimental data. The lowest black curve in each figure represents the case in which the interfacial resistance is included, but the interfacial resistivity ρ is regarded as a constant value ρ_0. This curve is seen to be lower than the experimental data, especially after percolation threshold. The middle blue curve represents the case in which ρ is modified to $\rho(c_1)$ according to Eq. (2.17) with the consideration of the additional contribution from the effect of tunneling-assisted

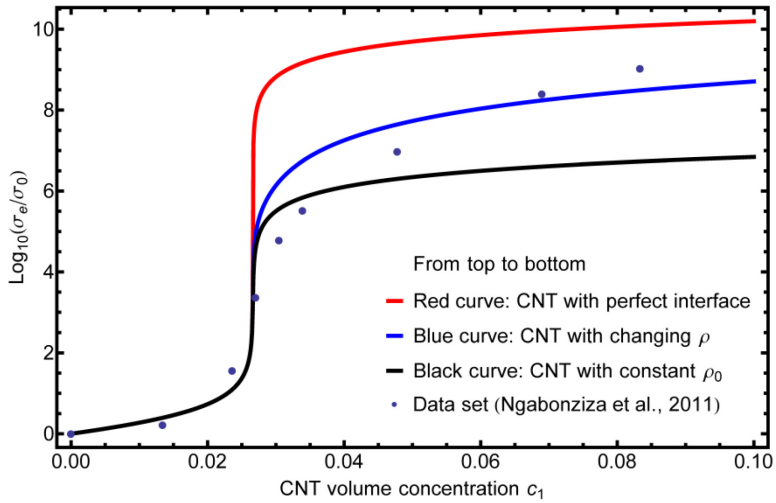

FIG. 2.7. Effective electrical conductivity of the CNT-based nanocomposite with Ngabonziza *et al.* (2011) data.

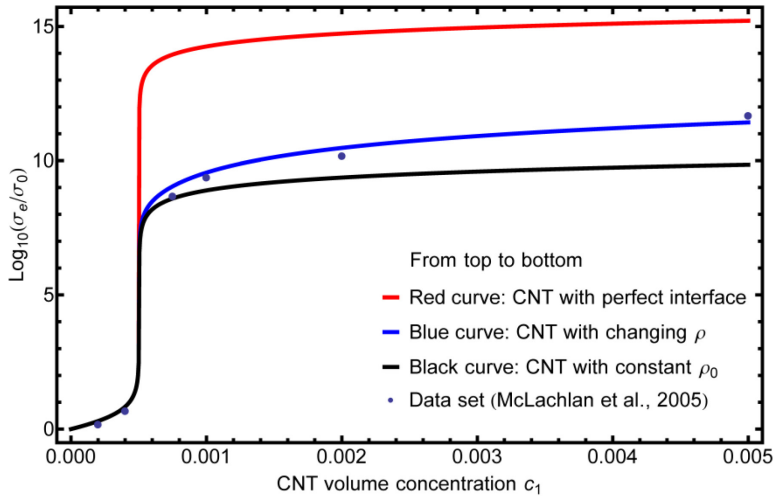

FIG. 2.8. Effective electrical conductivity of the CNT-based nanocomposite with McLachlan *et al.* (2005) data.

interfacial conductivity. And this curve gives the best predictions for the experimental data. This study clearly confirms the view that imperfect interface effect is important, and that the tunneling-assisted increase in interfacial conductivity is also a critical component of the theory. It is the combination of the effective-medium approach, interfacial resistance, and tunneling-assisted interfacial conductivity that eventually gives rise to a complete theory for the effective electrical conductivity of CNT-based nanocomposites.

2.3.3. Effect of CNT anisotropy

Now with the theory established, we can examine the effect of CNT anisotropy on the effective electrical conductivity. In our previous analysis, the results were obtained based on the assumed value of $m = 10^{-3}$. In fact while the transverse electrical conductivity of CNT is known to be several orders of magnitude lower than the axial one, the precise value of m is not clear. Thus further parametric studies are needed to clarify its effect. So we again use the first set of parameters listed in Table I for the experimental data of Ngabonziza *et al.* and consider four cases from isotropic to transversely isotropic, with $m = 1,\ 10^{-3},\ 10^{-8},$ and 0, with the last one meaning that there is only axial electrical conductivity. The results are displayed in Fig. 2.9. From this figure we can immediately conclude that the effective electrical conductivity of CNT-based nanocomposites is not sensitive to the value of m. Although the transverse electrical conductivity of CNT is lower than its axial one, it

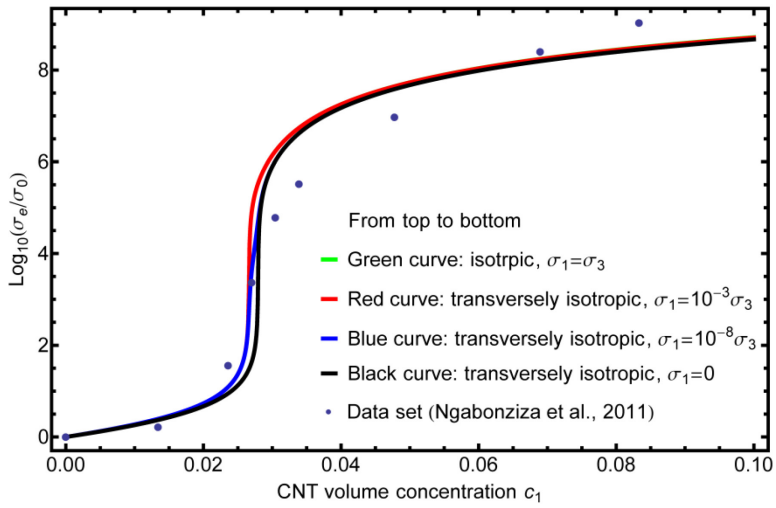

FIG. 2.9. Effect of CNT anisotropy on the overall electrical conductivity. The green curve is entirely overlapped by the red curve because of insignificant difference.

still has to be much higher than that of the polymer matrix. So far we have not seen

any direct measurement on σ_1 for CNTs, but for graphite sheets the electrical conductivity in the basal plane has been reported to be about 2-3 orders higher than that along the normal direction.[73] In this regard the value of *m* is most likely to lie within the range of $10^{-3} \sim 10^{-2}$, and our assumed value of 10^{-3} can be so justified.

2.3.4. Effective electrical conductivity with a totally insulating matrix

In CNT-based nanocomposites, electric current that flows from CNTs to the matrix or from one CNT to another one in contact, as well as the direct electron tunneling from one CNT to another, can all contribute to the overall electrical conductivity. So even when the polymer matrix is totally insulating ($\sigma_0 = 0$), a viable continuum model should still be able to deliver a non-zero σ_e from the last two mechanisms. In fact, even without the electron tunneling process, direct contact between CNTs should still provide a conductive pathway for current flow, and thus the overall electrical conductivity should still exist. Such a capability, however, is lost in both the M-T and the PCW methods, because in both cases each CNT must be embedded in the polymer matrix. This can be seen from Eq. (2.5) that, if $\sigma_0 = 0$, the effective electrical conductivity will be $\sigma_e = 0$ (to see this, multiply σ_0 on both sides of the equation). To test such a capability for the effective-medium approach, we take Eq. (2.9) to solve for σ_e under the insulating matrix condition. As has been discussed before, initially when c_1 is very low, All coefficient A, B and C in Eq. (2.9) are positive, so there are two negative roots, which should be rejected since the electrical conductivity must be positive. Only when $c_1 > c_1^*$, coefficient C becomes

negative, so there is one positive root, which is the effective electrical conductivity we want to solve. The condition of $C = 0$ is a critical point where the root is $\sigma_e = 0$.

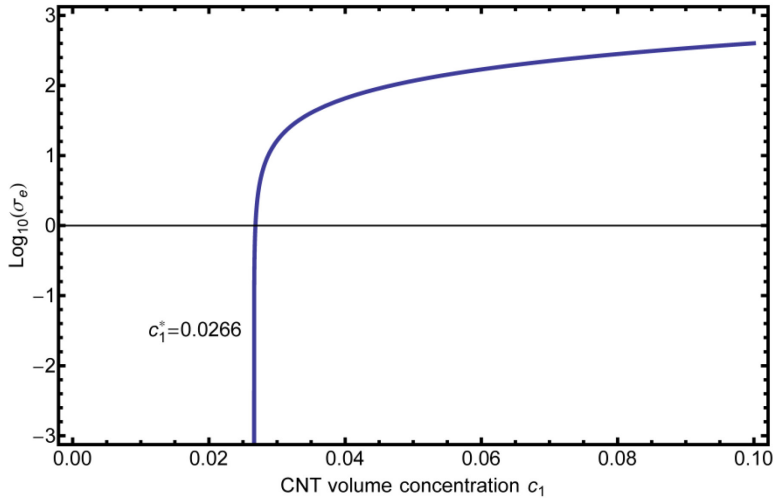

FIG. 2.10. Examination of the effective-medium approach for the effective electrical conductivity of a composite with a totally insulating matrix.

This analysis indicates that, when $c_1 < c_1^*$, since at this stage all CNTs are isolated by the insulating matrix, there is no overall electrical conductivity. And when $c_1 \geq c_1^*$, the nanocomposite starts to give a non-negative electrical conductivity due to the formation of the conductive networks. With the first set of constants taken from Table I, the calculated σ_e from $c_1 = c_1^*$ to $c_1 = 0.1$ is shown in Fig. 2.10. A drastic increase of electrical conductivity is observed near the percolation threshold.

2.4. Conclusions

In this chapter we have developed a continuum model to determine the electrical conductivity of CNT-based nanocomposites. This model consists of three major components: (i) the effective-medium approach with a perfect interface, (ii) a diminishing layer of interface with an interfacial resistivity, and (iii) a statistical

function to characterize the increase of interfacial conductivity due to electron tunneling effect. The outcome is a simple and widely useful model that possesses a percolation threshold, interfacial resistance, and the additional tunneling-assisted interfacial conductivity that contributes to the overall electrical conductivity of CNT-based nanocomposites.

We have demonstrated that this model could successfully capture the quantitative behavior of two sets of experimental data of the electrical conductivity of CNT nanocomposites, one for multi-walled CNT with polyimide, and another for single-walled CNT with polyimide. In this process, we have also shown how an imperfect interface lowers the overall electrical conductivity, and how the additional tunneling-assisted interfacial conductivity significantly brings it up after the percolation threshold. We have also used the developed model to study the effect of anisotropy of the electrical conductivity of CNT in the axial and transverse directions. It is demonstrated that, even though the transverse electrical conductivity of CNT is substantially lower than its axial one, its effect is insignificant, and it is the axial electrical conductivity of CNT that governs the whole transport process. In the end we have proved that, even with a perfectly insulating matrix, the effective-medium approach is still capable of delivering non-zero electrical conductivity for CNT-based nanocomposites after the percolation threshold.

Chapter 3.

Graphene-based nanocomposites

3.1. Overview

Graphene and CNT have many properties in common. Both of them possess high mechanical stiffness and strength, as well as exceptional thermal and electrical conductivity. With extremely small aspect ratio, graphene's flat shape also gives it very low percolation threshold (as low as 0.1 vol.%[74]) which makes it an ideal filler to improve the electrical conductivity of polymer composites. Compared with CNT, graphene is in general easier to prepare and less costly for mass production which gives it a potential edge over CNT for applications. Graphene is usually prepared from the exfoliation of graphite down to single layer.[75,76] However, the complete exfoliation of graphite to a single layer, as well as the homogeneous dispersion of individual graphene, is not easy to achieve. The prepared graphene samples usually have a few layers stacked together, and are also likely to cluster together to form graphene agglomerates which can be observed from various TEM images. Different process conditions, such as the oxidation of graphite and the energy supplied during sonication, as well as interaction energies between graphene, matrix, and surfactant (if present) can all affect the dispersion state of graphene fillers and give rise to different degrees of graphene agglomeration. A similar picture has also been found in CNT-based nanocomposites. Since dispersion state is one of the key factors in the determination of overall properties of composites, it is essential that the nature of

dispersion state and its influence are fully considered. This issue appears not to have received close attention. But with CNT fillers, a few experimental results - including those by Martin *et al.*,[52] Hernández *et al.*,[77] and Aguilar *et al.*[78] - have indicated that agglomeration could favor the formation of conductive networks and improve the effective electrical conductivity. Recently Gong *et al.*[19] also analyzed this issue by experiment and MC simulations. In the context of thermal conductivity, Cherkasova and Shan[79] have also reported that CNT agglomeration can have a significant effect. Filler agglomeration also has a direct impact on the percolation threshold. As extensively reviewed by Nan *et al.*,[80] this is a particularly acute issue for electrical conductivity with extreme filler aspect ratios, such as CNTs and graphene. Therefore, when studying the electrical conductivity of graphene-based nanocomposites, it is essential to take the nonhomogeneous dispersion state of graphene fillers, i.e., filler agglomeration, into account.

One of the simplest ways to treat the filler agglomeration effect is to adopt a two-scale approach as suggested by Barai and Weng[81] in the study of CNT-based metal plasticity, and also by Prasher *et al.*[82] and Reinecke *et al.*[83] in the context of thermal conductivity. In this approach the composite is considered to consist of CNT-rich agglomerated regions embedded in a CNT-poor region. Barai and Weng[81] assumed that all CNTs were clustered together to form spherically shaped agglomerates, while the CNT-poor region was occupied solely by the matrix material. Under this setting they reported a significant reduction in overall yield strength and it was found to be in close agreement with the experimental data of Kim *et al.*[84] In

current study, we will take advantage of the continuum model we have built for CNT-based nanocomposites, together with this two-scale approach, to investigate the graphene-based nanocomposites with different degrees of graphene agglomeration. In addition to filler agglomeration, the effect of imperfect interface and electron tunneling effect are also important issues for the electrical conductivity of graphene-based nanocomposites. To resolve these two issues, our previous model that possesses a diminishing layer of weak interphase and a statistical representation for tunneling-assisted interfacial conductivity, will also be adopted here.

3.2. The theory

In the theoretical development we will first outline the geometrical setting for the two-scale morphology of the graphene-based nanocomposite consisting of the graphene-rich agglomerates and the remaining graphene-poor region. Then we will introduce the effective-medium approach to determine the percolation threshold and the overall electrical conductivity. Finally we will take advantage of our previous interface model that can account for interfacial resistance on one hand and the reduction of interfacial resistivity due to electron tunneling effect on the other. These three components will then be integrated to form the complete theory.

3.2.1. Two-scale morphology of graphene-based nanocomposites

The typical morphology of a graphene-based, agglomerated nanocomposite is schematically shown in Fig. 3.1. Inside the composite, some graphene fillers gather

together to form the agglomerates, while others exist as individual graphene. Both

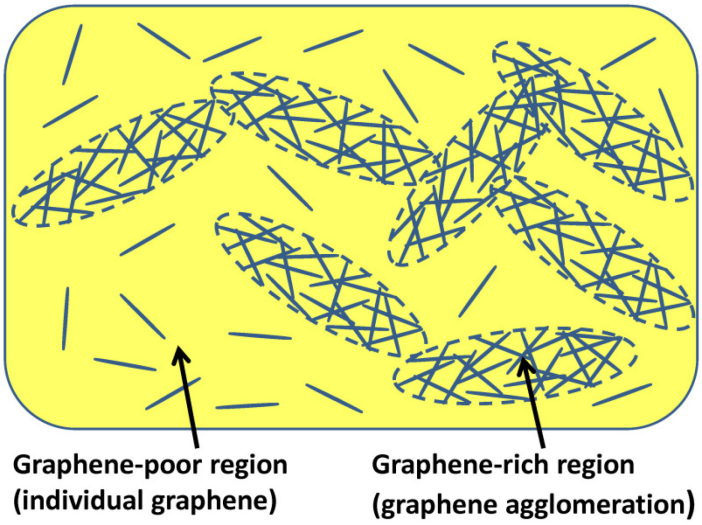

FIG. 3.1. A schematic plot of the two-scale model of the nanocomposite with filler agglomeration.

kinds of graphene are taken to be homogeneously dispersed and randomly oriented in each region. To model such a morphology, we divide the entire volume of the composite into two - one is the graphene-rich agglomerates and the other is the graphene-poor region. The volume concentrations of the graphene-rich and the graphene-poor regions are denoted as c_R and c_P, respectively, so that

$$c_R + c_P = 1, \tag{3.1}$$

where subscript *R* stands for "rich" and *P* for "poor". We assume that the agglomerates are also homogeneously dispersed and randomly oriented, and have a shape that can be grossly represented by a spheroid, with an aspect ratio α_R. Inside the agglomerate, there is a large amount of graphene residing in the polymer matrix, with the volume concentrations $c_1^{(R)}$ and $c_0^{(R)}$, respectively, satisfying

$$c_1^{(R)} + c_0^{(R)} = 1, \tag{3.2}$$

where subscripts 1 and 0 stand for graphene and polymer matrix, respectively. We

shall also represent the individual graphene sheets by highly oblate spheroids with a very low aspect ratio, α. The low aspect-ratio graphene can be easily in contact with each other to form conductive networks. When this happens, $c_1^{(R)}$ must be large enough to exceed the percolation threshold of the graphene-rich region. In the graphene-poor region, there are also graphene and polymer matrix, with the volume concentrations $c_1^{(P)}$ and $c_0^{(P)}$, respectively, such that

$$c_1^{(P)} + c_0^{(P)} = 1. \tag{3.3}$$

As a result of these distributions, the total volume concentration of graphene fillers, denoted by c_1, is the sum of graphene concentration from both graphene-rich and graphene-poor regions, and so is the total volume concentration of the matrix, c_0. They satisfy

$$\begin{aligned} c_1 &= c_1^{(R)} c_R + c_1^{(P)} c_P, \\ c_0 &= c_0^{(R)} c_R + c_0^{(P)} c_P, \\ c_1 &+ c_0 = 1. \end{aligned} \tag{3.4}$$

It is this c_1 that represents the volume concentration of total graphene inside the nanocomposite that is commonly measured in experiments. With these definitions, the dispersion state of graphene fillers can be described. However, we still need to know how they evolve as c_1 increases. Here we choose to study the dependence of c_R, $c_1^{(R)}$ and $c_1^{(P)}$, as the other three can be derived from above relations. There are two basic requirements for c_R, $c_1^{(R)}$ and $c_1^{(P)}$. The first one is that, if there is no graphene fillers in the composite, there should be no graphene agglomerates and no individual graphene inside the graphene-poor region. In other words, when $c_1 = 0$, we must have $c_R = 0$ and $c_1^{(P)} = 0$. The second one is that, if graphene fillers

occupy the entire composite, then both the graphene-rich and the graphene-poor regions are filled with graphene. This implies that, when $c_1 = 1$, we must have both $c_1^{(R)} = 1$ and $c_1^{(P)} = 1$.

We also need to know how graphene fillers are distributed into the graphene-rich and the graphene-poor regions. For this purpose, we introduce a parameter, *a* ($0 \le a \le 1$), to represent the volume fraction of graphene inside the graphene-rich region out of the total amount of graphene; it satisfies

$$a = c_1^{(R)} c_R / c_1 . \tag{3.5}$$

Essentially, the parameter *a* specifies how much of the total amount of graphene is allocated to the graphene-rich region (say, 70 or 80%). We also need to specify the dependence of $c_1^{(R)}$ on c_1. As the graphene agglomerate tends to percolate earlier than the entire composite, $c_1^{(R)}$ can be greater than the percolation threshold of the graphene-rich region at low c_1. Hence when $c_1 \to 0$, $c_1^{(R)}$ doesn't need to start from 0, but can have a non-zero initial value, represented by another parameter *b*. But this $c_1^{(R)}$ must grow to 1 when $c_1 = 1$. From these two requirements we assume a linear dependence on c_1 for $c_1^{(R)}$, as

$$c_1^{(R)} = b + c_1 (1 - b). \tag{3.6}$$

Parameter *b* also lies between 0 and 1. When $b = 0$, we have $c_1^{(R)} = c_1^{(P)} = c_1$; there is no distinction among the three and thus the composite is homogeneous. For an agglomerated composite, its *b* value has to be greater than 0, so that $c_1^{(R)} > c_1$. This implies that graphene is more concentrated inside the graphene-rich region, and its percolation condition is reached earlier than that of the overall nanocomposite. It

should also be noted that it is the quantity, $c_1^{(R)}c_R$, that specifies the volume fraction of graphene out of the total c_1 to reside inside the agglomerates. At $c_1 = 0$, the volume fraction of the graphene-rich region is zero, i.e., $c_R = 0$. So even though at zero graphene concentration $c_1^{(R)} \neq 0$, there is still no graphene in the "graphene-rich" region or anywhere else.

With parameters *a* and *b*, we can then obtain the dependence of c_R and $c_1^{(P)}$ on c_1, as

$$\begin{aligned} c_R &= \frac{a}{b + c_1(1-b)} c_1, \\ c_1^{(P)} &= \frac{(1-a)\left[b + c_1(1-b)\right]}{-c_1 a + \left[b + c_1(1-b)\right]} c_1. \end{aligned} \tag{3.7}$$

The dispersion state of graphene is now completely specified by the two parameters, *a* and *b*. In the limiting case when $a = 1$, all graphene are allocated to the agglomerates and there is no $c_1^{(P)}$. When $a = 0$ we have $c_R = 0$ and $c_1^{(P)} = c_1$, so the composite is completely specified by the graphene-poor region. In both cases the two-scale composite is reduced to only one scale, making it back to a homogeneous composite. With Eq. (3.6) and (3.7) representing the geometrical foundation of graphene filler agglomeration, we have now fully established the two-scale morphology of graphene-based nanocomposites.

3.2.2. The effective-medium approach in the two-scale model

The electrical conductivity of graphene-based nanocomposites has similar features to that of CNT-based nanocomposites. It is also a problem with high contrast between two phases and significantly low percolation threshold. The graphene fillers

have random orientation and very low aspect ratio, and the latter will facilitate the formation of conductive networks. Therefore, the 3-D random effective-medium approach for a two-phase composite is still applicable here. In this approach, phase 1 denotes the randomly orientated ellipsoidal inclusions, while phase 0 denotes the matrix, such that

$$c_0 \frac{\sigma_0 - \sigma_e}{\sigma_e + (1/3)(\sigma_0 - \sigma_e)} + c_1 \frac{1}{3}\left[\frac{2(\sigma_1 - \sigma_e)}{\sigma_e + S_{11}(\sigma_1 - \sigma_e)} + \frac{\sigma_3 - \sigma_e}{\sigma_e + S_{33}(\sigma_3 - \sigma_e)} \right] = 0, \quad (3.8)$$

which is identical to Eq. (2.8). This equation can be applied to both scales of graphene nanocomposites. On the smaller scale of the graphene-rich and graphene-poor regions, phase 1 is identified as the individual graphene. It has electrical conductivity σ_3 in the normal direction and $\sigma_1 = \sigma_2$ in the isotropic hexagonal graphene plane, S-tensor components S_{11} and S_{33} which are determined by its aspect ratio α according to Eq. (2.2), and volume concentration c_1 replaced by $c_1^{(R)}$ (for graphene-rich region) or $c_1^{(P)}$ (for graphene-poor region). Phase 0 on the other hand is identified as polymer matrix. It has isotropic electrical conductivity σ_0, S-tensor component 1/3 in all three directions, and volume concentration c_0 replaced by $c_0^{(R)}$ (for graphene-rich region) or $c_0^{(P)}$ (for graphene-poor region). On the larger scale of the composite, phase 1 is identified as the graphene agglomerates while phase 0 as the graphene-poor region. In this case σ_3 and σ_1 become the overall electrical conductivity of the graphene-rich region in the normal and in-plane direction; σ_0 becomes the overall electrical conductivity of the graphene-poor region; S_{11} and S_{33} becomes the S-tensor components of graphene agglomerates, $S_{11}^{(R)}$ and $S_{33}^{(R)}$, which are calculated from the aspect ratio of graphene agglomerates, α_R; and lastly, c_1 and

c_0 become c_R and c_P, respectively.

In our two-scale model, the calculation of effective electrical conductivity of graphene-based nanocomposites takes two steps. In the first place, in both graphene-rich and graphene-poor regions graphene fillers are embedded in the polymer matrix (or more strictly speaking, both graphene fillers and polymer matrix are embedded in the effective medium, as indicated by effective-medium approach). So we use Eq. (3.8) on the smaller scale, to obtain the overall electrical conductivity of the graphene-rich and graphene-poor region, respectively. On the larger scale, it can be regarded that graphene agglomerates are also embedded in the graphene-poor region. Therefore, we take advantage of the properties of both regions to implement Eq. (3.8) once again, and the effective electrical conductivity of the whole composite, σ_e, can then be solved.

3.2.3. The percolation threshold in the two-scale model

The derivation of percolation threshold has been discussed in last chapter, and its result is given in Eq. (2.11) as a function of S-tensor component S_{33}. By taking the S-tensor of graphene, Eq. (2.11) can be used to determine the percolation threshold of the graphene-rich region, with c_1^* identified as $c_1^{(R)*}$. $c_1^{(R)*}$ is related to c_1^* of the overall composite through Eq. (3.6), such that

$$c_1^* = \frac{c_1^{(R)*} - b}{1-b}, \quad \text{where} \quad c_1^{(R)*} = \frac{9S_{33}\left(1-S_{33}\right)}{-9S_{33}^2 + 15S_{33} + 2}. \tag{3.9}$$

Likewise, Eq. (2.11) can also be used to determine the percolation condition of the large-scale overall composite, c_R^*, by identifying S-tensor as that of the graphene

agglomerate. This c_R^* is related to c_1^* of the composite through Eq. (3.7), such that

$$c_1^* = \frac{bc_R^*}{a-(1-b)c_R^*}, \quad \text{where} \quad c_R^* = \frac{9S_{33}^{(R)}\left(1-S_{33}^{(R)}\right)}{-9S_{33}^{(R)2}+15S_{33}^{(R)}+2}, \tag{3.10}$$

where $S_{33}^{(R)}$ (so is $S_{11}^{(R)}$) is the component of S-tensor of graphene agglomerate that depends on its aspect ratio, α_R.

For the graphene-based nanocomposite to be in a percolated state, the percolation condition by individual graphene inside the graphene-rich region as specified by Eq. (3.9) and the percolation condition by the large-scale agglomerates specified by Eq. (3.10) must both be satisfied. So it is the larger of the two c_1^* calculated from these two equations that represents the true percolation threshold of the nanocomposite. But in general it is the second one given by Eq. (3.10) that defines the percolation threshold as the first condition is easier to meet. It is clear from Eq. (3.10) that the percolation threshold c_1^* for the overall, large-scale composite depends on the three parameters, *a*, *b*, and α_R. Parameter *a* specifies how much of the total amount of graphene is allocated to the graphene-rich agglomerates; parameter *b* specifies the volume fraction of graphene inside the agglomerate, $c_1^{(R)}$; and parameter α_R specifies the shape of the agglomerates.

3.2.4. Interfacial resistance and tunneling-assisted interfacial conductivity

For the problem of imperfect interface condition between graphene fillers and polymer matrix, we use the same coated graphene model as we did for CNTs, to incorporate the effect of interfacial resistance. The calculation of the overall electrical conductivity of coated graphene, $\sigma_i^{(c)}$, by M-T method is the same as Eq. (2.13). But

now the volume concentration of original graphene in the coated graphene, ν, is expressed in terms of the thickness of interface, *t*, and that of the graphene, λ, as

$$\nu = \frac{\lambda}{2}\left(\frac{\lambda}{2\alpha}\right)^2 \Bigg/ \left[\left(\frac{\lambda}{2}+t\right)\left(\frac{\lambda}{2\alpha}+t\right)^2\right] \approx 1-(2+4\alpha)\frac{t}{\lambda}, \tag{3.11}$$

by taking the limit $t \to 0$. With the additional assumption $\sigma_i^{\text{int}}/\sigma_i \to 0$, $\sigma_i^{(c)}$ can then be rewritten as

$$\sigma_i^{(c)} = \frac{\sigma_i}{1+\sigma_i S_{ii}(2+4\alpha)\rho/\lambda}, \tag{3.12}$$

where $\rho = \lim_{\sigma_i^{\text{int}}/\sigma_i \to 0,\, t\to 0} t/\sigma_i^{\text{int}}$ has been taken to be isotropic for the interface. Furthermore, the effect of tunnel-assisted interfacial conductivity is considered by letting ρ decrease from initial value ρ_0 as c_1 increases. And the dependence of ρ on c_1 is also governed by Cauchy's cumulative distribution function *F*, as has been given in Eq. (2.16) and (2.17).

The above imperfect interface model with tunnel-assisted interfacial conductivity will be applied to both the small-scale graphene/polymer interface, as well as to the large-scale graphene-rich/graphene-poor interface. So far our theory has been completely developed. We then demonstrate that a set of newly reported data for graphene/polystyrene nanocomposites can be well captured by this theory.

3.3. Results and discussion

This set of experimental data was reported by Tkalya *et al*.[32] They measured the percolation threshold and effective electrical conductivity of graphene/polystyrene nanocomposites as a function of weight percent of graphene fillers. Four different

samples of nanocomposites were prepared. Their different dispersion states can be identified from the reported TEM images. The data of the four samples display conspicuously different percolation thresholds, as reproduced in Fig. 1.3. Note that the data are plotted in terms of weight fraction of graphene. They also indicated that the density of graphene is twice of that of polystyrene, so that the wt.% can be converted to the vol.% by the formula, $1/c_1 = 2/w_1 - 1$, where c_1 and w_1 are the volume and weight concentrations of graphene, respectively. It can be seen that sample B has the highest percolation threshold at 4.5 wt.%, followed by samples A-HE, A-LC, and A, with 3.0 wt.%, 2.3 wt.%, and 2.0 wt.%, in turn. These results can be translated into the percolation thresholds of $c_1^* = 0.023$, 0.015, 0.012 and 0.010, respectively.

They also reported that the major difference among the four samples was the different degrees of graphene agglomeration due to different processing routes. Sample B was prepared from graphene produced by the liquid-phase exfoliation of graphite, which resulted in the most dispersed graphene fillers. The other three samples were prepared from graphene produced by thermal reduction of graphite oxide, but with different amount of energy provided during the sonication process. The UV-vis spectra can further indicate their dispersion states, that graphene fillers in samples A and A-LC were more agglomerated than those in sample A-HE, which was in line with the fact that more energy was supplied to sample A-HE during the sonication process. Sample A was only slightly more agglomerated than sample A-LC, but this made it the highest agglomerated sample among the four. Based on

these observations, we assume that the amount of graphene agglomeration in sample B is negligible, and that the degree of graphene agglomeration increases from sample A-HE, to A-LC, and to A.

Table II. Physical values used in model calculations for samples B, A-HE, A-LC, and A. The last column gives the percolation threshold for the idealized spherical agglomerates.

	Sample A	Sample A-LC	Sample A-HE	Sample B	Spherical agglomerates
Parameter a	0.9	0.8	0.9	...	0.7
Parameter b	0.05	0.08	0.05	...	0.05
Percolation threshold (%)	1.01	1.16	1.52	2.30	4.35
Aspect ratio of agglomerate α_R	0.1241	0.0728	0.1399	...	1.0
Thickness of agglomerate λ (nm)	50	50	50	...	50
Initial interfacial resistivity ρ_0 (m^2/S)	5×10^{-8}	1×10^{-7}	6×10^{-7}	5×10^{-7}	5×10^{-7}
Scale parameter γ	0.03	0.003	0.01	0.001	0.01

In our numerical computations, the in-plane electrical conductivity of graphene is taken to be $\sigma_1 = 8.32\times10^4$ S/m. This value is adopted from Stankovich *et al*.[28] who gave a range of $10^{4.92\pm0.52}$ S/m, so here we use the value of $10^{4.92}$ S/m. The normal electrical conductivity of graphene is taken as $\sigma_3 = m\sigma_1$, with $m = 10^{-3}$. The electrical conductivity of polystyrene is taken to be $\sigma_0 = 6.09\times10^{-12}$ S/m, from Srivastava and Mehra.[85] Other parameters used here include the aspect ratio of graphene $\alpha = 0.0136$, the thickness of graphene $\lambda = 5$ nm, the initial interfacial resistivity $\rho_0 = 5\times10^{-7}$ m^2/S, and scale parameter $\gamma = 0.001$. On the larger scale of the composite consisting of graphene-rich agglomerates and graphene-poor region, the constants used are sample-dependent and listed in Table II. Note that the listed α_R, λ and ρ_0 pertain to this large-scale property. With these constants, we now

show the calculated results.

3.3.1. Homogeneously dispersed graphene: Sample B

First we consider the test data of sample B, which are reproduced in Fig. 3.2. This set of data has a reported percolation threshold of $c_1^* = 0.023$, that can be directly calculated from Eq. (2.2) with the aspect ratio $\alpha = 0.0136$, since this sample has no filler agglomerations. We make an initial calculation for the overall electrical conductivity by assuming a perfect interface (with $\rho = 0$, or $\sigma_i^{(c)} = \sigma_i$). The effective electrical conductivity can be obtained from Eq. (3.8). The calculated result is shown in red line in Fig. 3.2. The comparison between this curve and the experimental data clearly indicates that the calculated electrical conductivity is substantially higher than the test data. This is an indication that the interface condition between graphene and polystyrene cannot be perfect.

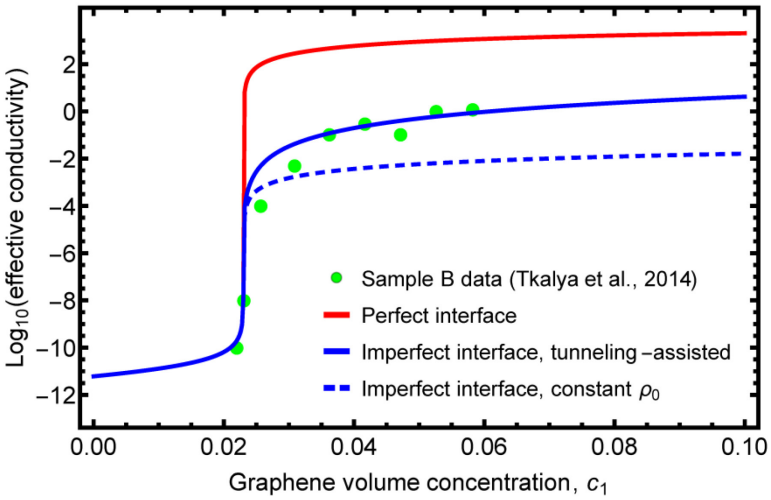

FIG. 3.2 Theoretical curves for sample B data with perfect and imperfect interface.

In order to understand the effect of an imperfect interface, we then use the constant interfacial resistivity, $\rho = \rho_0$, to make the calculation. The calculated

conductivity is shown in the dashed blue line. When compared with the perfect interface curve, this result clearly shows a substantial drop, to an order that is closer to the test data. But the trend of this curve is seen to stay relatively flat after percolation threshold. This is an indication that, without accounting for the additional contribution from the tunneling-assisted interfacial conductivity, the theoretical results become too low, especially after the percolation condition has been reached. When this tunneling effect is implemented through $\rho(c_1)$ in Eq. (2.17), we can see a continuous gain in effective electrical conductivity as shown in the blue line. The outcome is a curve with an added slope, and the theory is then in very close agreement with the experimental data. This consideration strongly points to the need of an imperfect interface with a tunneling-assisted interfacial conductivity.

3.3.2. Nanocomposites with agglomerations: Samples A-HE, A-LC and A

We now use the two-scale model to study the effect of graphene agglomeration on the percolation threshold and overall electrical conductivity in samples A-HE, A-LC, and A. These three samples were reported to have increasing degree of agglomeration, respectively. Their experimental data are reproduced in Fig. 3.3 to Fig. 3.5, along with theoretical results from the two-scale effective-medium approach. In each case parameters *a* and *b* and the aspect ratio of graphene-rich agglomerates, α_R, are all involved in the calculation.

With the constants listed in Table II, the calculated results for these three samples are also plotted in Fig. 3.3 to Fig. 3.5. As with Fig. 3.2, the red line in each figure

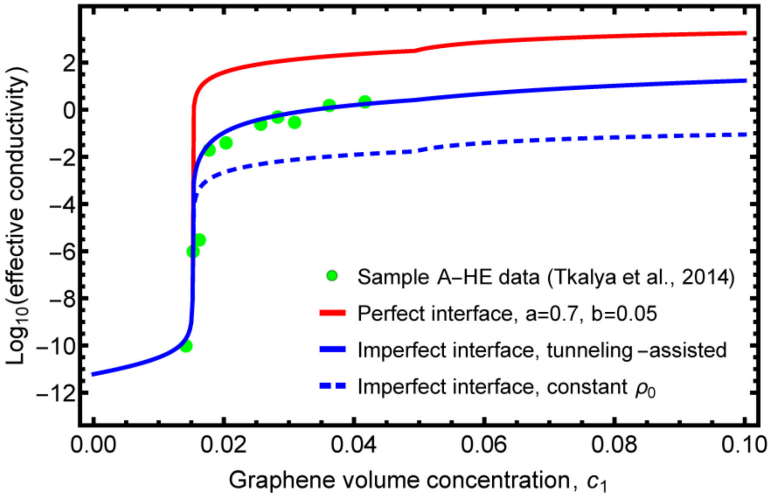

FIG. 3.3. Theoretical curves for sample A-HE data with perfect and imperfect interface.

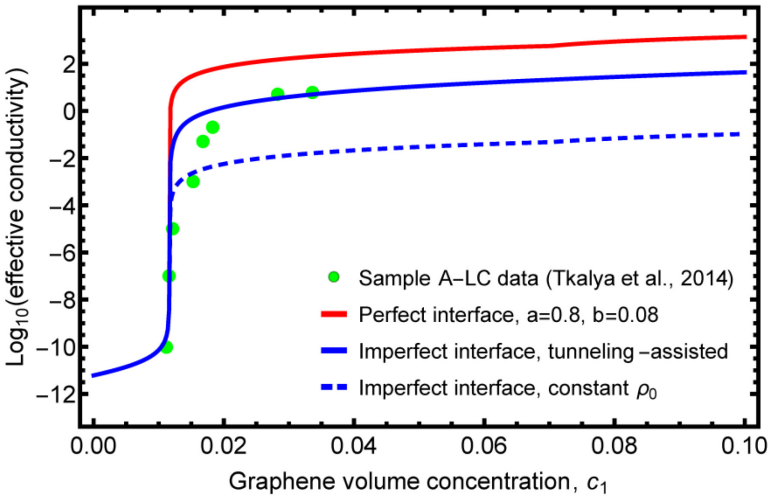

FIG. 3.4. Theoretical curves for sample A-LC data with perfect and imperfect interface.

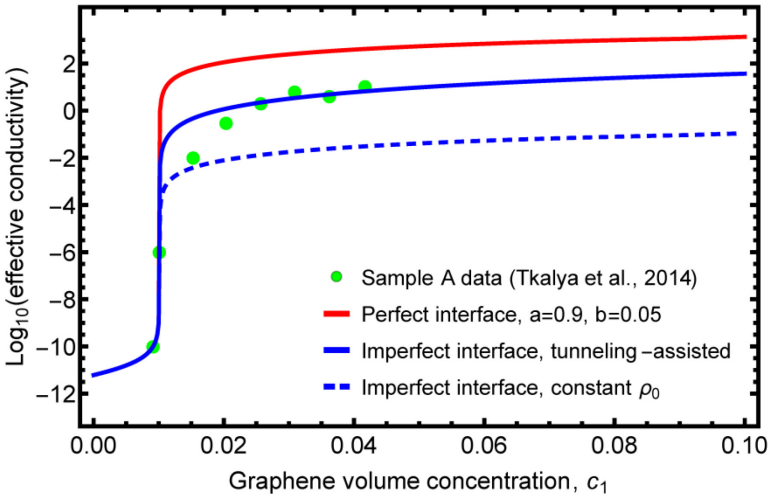

FIG. 3.5. Theoretical curves for sample A data with perfect and imperfect interface.

represents the calculated conductivity under the assumption of a perfect interface. The three red curves are seen to be notably higher than their respective experimental data. By implementing a constant interfacial resistivity, $\rho = \rho_0$, the calculated conductivity, shown in each dashed blue line, is significantly reduced. These curves however all appear to stay relatively flat after the percolation threshold. It is only when the tunneling-assisted interfacial conductivity is also implemented into the interface model can all the reported experimental data be well captured.

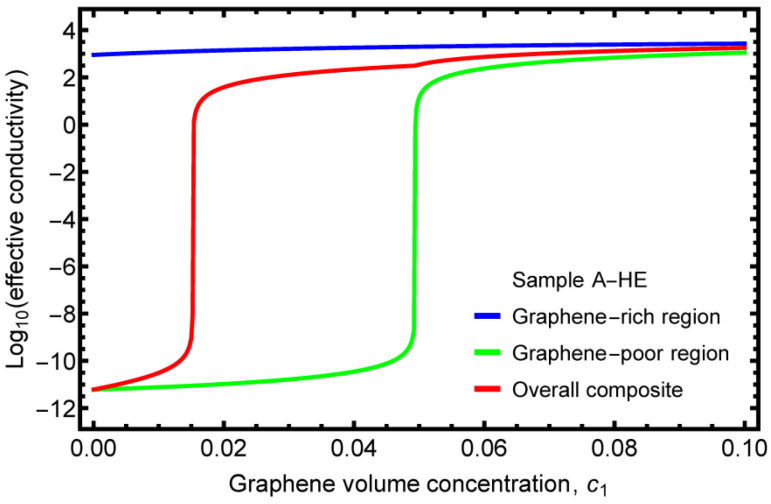

FIG. 3.6. Contribution of percolation in the graphene-poor region to the kink in the curves of Fig. 3.3.

In passing it may be noted that there is a strange kink in the red curve in Fig. 3.3 around $c_1 = 0.05$, and so is in Fig. 3.4 around $c_1 = 0.07$. At first sight this might appear to be a numerical artifact, but it is not. This slight increase is due to the onset of percolation in the graphene-poor region, as shown in Fig. 3.6.

3.3.3. The role of agglomerate shape on the percolation threshold

The preceding discussions have suggested that filler agglomeration has the

primary effect on the percolation threshold, and that interface conditions control the level of overall conductivity post percolation. In the past, it is often said that filler agglomeration tends to increase the percolation threshold, but we have proved and the discussed experiment has also shown that filler agglomeration can decrease the percolation threshold. This is a welcome consequence as high conductivity can be achieved at very low graphene loading. But it cannot be concluded that graphene agglomeration will always lower the percolation threshold. The percolation threshold c_1^*, as shown in Eq. (3.9) and (3.10), is seen to depend on the three parameters, *a*, *b*, and α_R. The first two specify the dispersion state of graphene in the agglomerates, whereas the third one defines the agglomerate shape. For the percolation threshold to decrease, the shape has to be sufficiently oblate (or prolate). If the shape is very rounded or becomes spherical, such a desirable outcome cannot be expected. To show such an effect, we have taken $\alpha_R = 1$ while retaining the other parameters used in the calculation of A-HE, to determine the corresponding percolation threshold. The newly calculated value is $c_1^* = 0.044$, which is higher than the percolation threshold of sample B, at $c_1^* = 0.023$. This value is listed in the last column of Table II. So it is possible that the percolation threshold increases with spherical or more rounded agglomerates.

To be sure, the choice of a spherical shape for the agglomerates, $\alpha_R = 1$, does not guarantee that the calculated percolation threshold will always be higher than $c_1^* = 0.023$; it also depends on the dispersion state represented by parameters *a* and *b*. This can be seen from the consideration of the percolation condition represented by

Eq. (3.10). When $\alpha_R = 1$, that is, when $c_R^* = 1/3$, we have $c_1^* = b/\left[3a-(1-b)\right]$. Therefore in order to have $c_1^* > 0.023$, it requires $b/\left[3a-(1-b)\right] > 0.023$ or $b > 0.0235(3a-1)$, which is 0.026 when $a = 0.7$. From the last column of Table II, the value of *b* is 0.05, which is indeed higher than 0.026, therefore the percolation threshold is higher than 0.023. If, instead, a value of $b < 0.026$ is chosen, the overall percolation threshold would become lower than that of the homogeneously dispersed nanocomposites

In summary, it is evident that the dispersion parameters *a* and *b*, and the agglomerate aspect ratio, α_R, all contribute to the final percolation threshold, c_1^*, of the agglomerated graphene nanocomposites.

3.4. Conclusions

In this chapter we have developed a continuum composite model to determine the percolation threshold and effective electrical conductivity of graphene-based nanocomposites, with a focus on the influence of graphene agglomeration. This model consists of three major components: (i) a two-scale model of the morphology of the nanocomposite, (ii) a two-scale effective-medium approach that is capable of delivering the percolation threshold, and (iii) an imperfect interface model that is coupled with the tunneling-assisted interfacial conductivity.

In the two-scale model of graphene-nanocomposite morphology, the composite is divided into two regions: the graphene-rich agglomerates and a graphene-poor region that serves as the matrix. In each region there exist randomly oriented graphene sheets

and polymer matrix. The effective-medium approach developed in the second component is then used to determine the effective electrical conductivity of the graphene-rich and the graphene-poor regions, and their conductivities in turn are used to determine the overall electrical conductivity of the nanocomposite. Due to the presence of interfacial resistance and the tunneling-assisted electric conduction process, the interface model developed in the third component is used to create a coated graphene (or a coated agglomerate) to replace the original graphene (or agglomerate) in the final calculation of the overall electrical conductivity.

Finally the developed theory is applied to examine a recently reported set of experimental data on the percolation threshold and overall electrical conductivity of graphene/polystyrene nanocomposites. This set of data involved four samples - samples B, A-HE, A-LC, and A - from no filler agglomeration to increasing degree of agglomeration. The one with no filler agglomerates, sample B, was found to have the highest percolation threshold, whereas the one with the most agglomerates, sample A, was reported to have the lowest percolation threshold. We have demonstrated that this new set of experimental data can be successfully explained with our newly developed theory. It is also demonstrated that it is the dispersion state of graphene, defined by parameters a and b, and the aspect ratio of agglomerates, α_R, that determine the percolation threshold, while it is the interface conditions and the intrinsic electrical conductivity of graphene and polymer matrix that determine the nanocomposite's overall electrical conductivity post percolation.

Chapter 4.

Multiferroic composites: inclusion-matrix type

4.1. Overview

In piezoelectric-piezomagnetic multiferroic composites, the most notable feature of their characteristics is the presence of magnetoelectric coupling coefficients even though neither constituent phase possesses such a property. The magnitude of these coefficients depends on many microstructural properties, including material property, phase connectivity, volume concentration, inclusion shape, and interface condition. In retrospect, magnetoelectric coupling effect was long reported by van Suchtelen in 1972,[33] but it was not until the Green's function formulation put forward by Nan in 1994[15] that a sound theoretical treatment was given. Soon after, Benveniste[36] also presented a theory in a spirit related to Hill[86] and Milgrom and Shtrikman[87] to determine the exact magnetoelectric coupling of a fibrous piezoelectric-piezomagnetic composite. The explicit expressions of the coupling coefficient, α_{33}, of the fibrous composite given by Nan and Benveniste are particularly enlightening, as the expressions vividly show how the elastic, piezoelectric, and piezomagnetic constants of the constituent phases jointly contribute to this magnetoelectric coupling coefficient. A critical issue in Nan's Green's function approach is the evaluation of Eshelby S-tensor of an ellipsoidal inclusion in the context of piezoelectric (or piezomagnetic) response. Since early 1990s many works have greatly contributed to this issue, as has been mentioned in Chapter 1. The progress in the formulation of

Eshelby S-tensor has made it possible for the study of the effective properties of transversely isotropic piezoelectric composites containing aligned spheroidal inclusions. Most notably among them are the works of Huang and Kuo,[17] Li and Dunn,[18] and Srinivas *et al*.[38]

Nevertheless, all of these works are concerned with the perfect interface case. In contrast there have been very few studies on the magnetoelectric coupling of multiferroic composites with an imperfect interface. It appears that the works of Wang and Pan,[88] Dinzart and Sabar,[89] Kuo,[90] and Yue and Xu[91] are the only ones that have considered the interface effect, but their focus of interface effects has been limited to the fibrous composites. It is well known that the interface condition can greatly affect the overall properties of a two-phase composite. In real composites the interface is usually not perfect, and the existence of imperfect interface could bring down its effective properties. This has been shown for CNT- and graphene-based nanocomposites in previous chapters. Therefore it is likely that imperfect interface would also lower the magnetoelectric coupling of a piezoelectric-piezomagnetic multiferroic composite. And this is the subject of our present investigation.

The composite model to be adopted here is schematically shown in Fig. 4.1(a), in which aligned spheroidal inclusions, which could be piezomagnetic or piezoelectric, are embedded in the matrix which could be piezoelectric or piezomagnetic. The interface between the two is not necessarily perfect. In this way, the basic microstructural features such as the volume concentration of the phases, phase connectivity, aspect ratio, and interface conditions, could all be included. Based on

this model we will develop a composite theory to explain how the effective magnetoelectric coupling coefficients, α_{33} and α_{11}, and voltage coefficients, α_{E33} and α_{E11}, of the multiferroic composite are controlled by these factors. In particular, our analysis will focus on the $BaTiO_3$-$CoFe_2O_4$ (BTO-CFO) system, and the aspect ratio α of inclusions will cover the entire range from zero to infinity, to represent the 2-2, 0-3, and 1-3 connectivities (shown in Fig. 4.1(b) to 4.1(d)). While the perfect

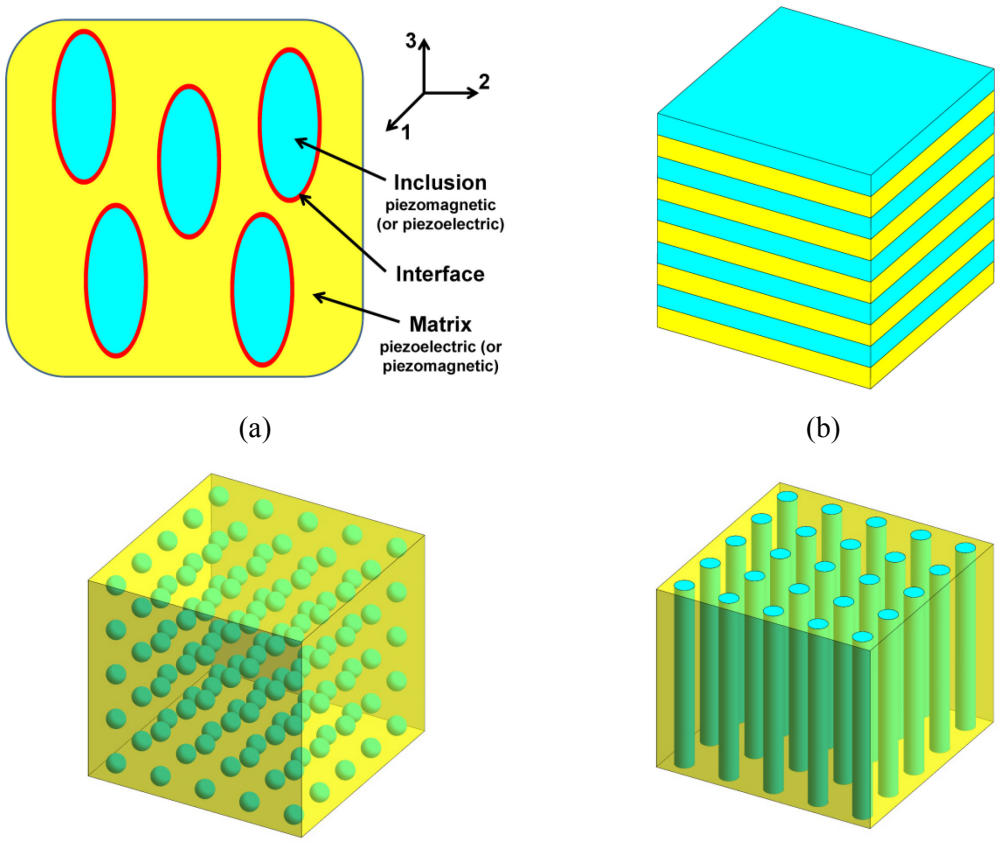

FIG. 4.1. Schematics of the microstructure of piezoelectric-piezomagnetic multiferroic composite: (a) general aligned spheroidal inclusions with an interface, (b) multilayers with 2-2 connectivity, (c) particulate composite with 0-3 connectivity, and (d) fibrous composite with 1-3 connectivity. In calculations $BaTiO_3$ (or BTO) and $CoFe_2O_4$ (or CFO) are taken as the piezoelectric and piezomagnetic phases, respectively.

interface case with full range of inclusion's aspect ratio and the imperfect interface case for fibrous composites have been separately studied in the past, simultaneous

investigation of interface effects and aspect-ratio dependence has never been done before; this is the spirit of this work and it is new.

The present study will provide a complete range of results for the magnetoelectric coupling of multiferroic composites, including all 2-2, 0-3 and 1-3 connectivities. Furthermore we will show that 1-3 composites tend to deliver a stronger α_{33} while 2-2 composites deliver a stronger α_{11}, and that CFO-in-BTO composites provide stronger coupling than BTO-in-CFO system. At the end, we will demonstrate that the experimentally measured data are far lower than the theoretical values calculated from the perfect interface condition, and that, with a weakened interface, the measured data could be captured by the theory.

4.2. The theory

The theory will be presented in three steps: (i) first we outline the general form of the coupled constitutive equations for multiferroic composites, (ii) then we provide the formulae for the effective electro-magneto-elastic moduli of multiferroic composites with a perfect interface, and (iii) finally we introduce an interface model to build a thinly coated inclusion for the study of interface effects.

4.2.1. Constitutive equations of the transversely isotropic phases and overall composites

We now first establish the constitutive equations of the piezoelectric and piezomagnetic phases and that of the overall electro-magneto-elastic multiferroic

composites. As shown in Appendix B, there are 8 different ways to write the constitutive equations. The choices depend on the selection of independent variables from mechanical stress σ and strain ε for the elastic field, electric displacement D and electric field E for the electric part, and magnetic flux density B and magnetic field H for the magnetic component. In the absence of body force and free charge, mechanical stress, electric displacement and magnetic flux density must satisfy the mechanical equilibrium and the quasi-static form of the Maxwell equations as

$$\sigma_{ij,j} = 0, \quad D_{i,i} = 0, \quad B_{i,i} = 0. \tag{4.1}$$

In addition, the mechanical strain, electric field, and magnetic field are all derivable from the gradients of displacement, u_i, and electric and magnetic potentials, ϕ and φ, respectively, as

$$\varepsilon_{ij} = \frac{1}{2}\left(u_{i,j} + u_{j,i}\right), \quad E_i = -\phi_{,i}, \quad H_i = -\varphi_{,i}. \tag{4.2}$$

For these reasons, it is convenient to choose (σ, D, B) as a pair and (ε, E, H) as the other, and write the constitutive equations in the form

$$\begin{aligned} \sigma &= \mathbf{C}\varepsilon - \mathbf{e}^{\mathrm{T}}E - \mathbf{q}^{\mathrm{T}}H, \\ D &= \mathbf{e}\varepsilon + \boldsymbol{\kappa}E + \boldsymbol{\alpha}H, \\ B &= \mathbf{q}\varepsilon + \boldsymbol{\alpha}E + \boldsymbol{\mu}H, \end{aligned} \tag{4.3}$$

where the diagonal tensor $\mathbf{C}$, $\boldsymbol{\kappa}$ and $\boldsymbol{\mu}$ are, respectively, fourth-order elastic stiffness tensor (measured at constant electric and magnetic fields), second-order electric permittivity tensor (measured at constant strain and magnetic field), and second-order magnetic permeability tensor (measured at constant strain and electric field). The off-diagonal tensor $\mathbf{e}$, $\mathbf{q}$ and $\boldsymbol{\alpha}$ are third-order piezoelectric, third-order piezomagnetic, and second-order magnetoelectric coefficient tensor, respectively, with

the superscript T denoting the transpose operation. Symbolically this set of coupled equations can be written in a unified fashion in terms of the Voigt and Nye contracted notations, as

$$\mathbf{X}_i = \mathbf{L}_{ij}\mathbf{Y}_j, \quad i, j = 1 \sim 12, \tag{4.4}$$

where

$$\begin{aligned} \mathbf{X} &= \left[\sigma, D, B\right]^{\mathrm{T}} = \left[\sigma_1\ \sigma_2\ \sigma_3\ \sigma_4\ \sigma_5\ \sigma_6\ D_1\ D_2\ D_3\ B_1\ B_2\ B_3\right]^{\mathrm{T}}, \\ \mathbf{Y} &= \left[\varepsilon, -E, -H\right]^{\mathrm{T}} = \left[\varepsilon_1\ \varepsilon_2\ \varepsilon_3\ \varepsilon_4\ \varepsilon_5\ \varepsilon_6\ -E_1\ -E_2\ -E_3\ -H_1\ -H_2\ -H_3\right]^{\mathrm{T}}, \end{aligned} \tag{4.5}$$

which are both 12-dimensional vectors, and

$$\mathbf{L} = \begin{bmatrix} \mathbf{C} & \mathbf{e}^{\mathrm{T}} & \mathbf{q}^{\mathrm{T}} \\ \mathbf{e} & -\boldsymbol{\kappa} & -\boldsymbol{\alpha} \\ \mathbf{q} & -\boldsymbol{\alpha} & -\boldsymbol{\mu} \end{bmatrix}, \tag{4.6}$$

which is the 12×12 electro-magneto-elastic moduli matrix (with **C** 6×6; **e** and **q** 3×6; $\boldsymbol{\kappa}$, $\boldsymbol{\alpha}$ and $\boldsymbol{\mu}$ 3×3). **L** is taken to be transversely isotropic with 3-direction as the symmetric axis and 1-2 plane isotropic. In this case it carries the form

$$\mathbf{L} = \begin{bmatrix} C_{11} & C_{12} & C_{13} & 0 & 0 & 0 & 0 & 0 & e_{31} & 0 & 0 & q_{31} \\ C_{12} & C_{11} & C_{13} & 0 & 0 & 0 & 0 & 0 & e_{31} & 0 & 0 & q_{31} \\ C_{13} & C_{13} & C_{33} & 0 & 0 & 0 & 0 & 0 & e_{33} & 0 & 0 & q_{33} \\ 0 & 0 & 0 & C_{44} & 0 & 0 & 0 & e_{15} & 0 & 0 & q_{15} & 0 \\ 0 & 0 & 0 & 0 & C_{44} & 0 & e_{15} & 0 & 0 & q_{15} & 0 & 0 \\ 0 & 0 & 0 & 0 & 0 & C_{66} & 0 & 0 & 0 & 0 & 0 & 0 \\ 0 & 0 & 0 & 0 & e_{15} & 0 & -\kappa_{11} & 0 & 0 & -\alpha_{11} & 0 & 0 \\ 0 & 0 & 0 & e_{15} & 0 & 0 & 0 & -\kappa_{11} & 0 & 0 & -\alpha_{11} & 0 \\ e_{31} & e_{31} & e_{33} & 0 & 0 & 0 & 0 & 0 & -\kappa_{33} & 0 & 0 & -\alpha_{33} \\ 0 & 0 & 0 & 0 & q_{15} & 0 & -\alpha_{11} & 0 & 0 & -\mu_{11} & 0 & 0 \\ 0 & 0 & 0 & q_{15} & 0 & 0 & 0 & -\alpha_{11} & 0 & 0 & -\mu_{11} & 0 \\ q_{31} & q_{31} & q_{33} & 0 & 0 & 0 & 0 & 0 & -\alpha_{33} & 0 & 0 & -\mu_{33} \end{bmatrix}, \tag{4.7}$$

which has 17 independent material constants (note that $C_{66} = \left(C_{11} - C_{12}\right)/2$). Here we have chosen the negative values of *E* and *H* in the **Y** term so that moduli matrix **L** can be cast in a diagonally symmetric form. Such a diagonal symmetry is essential as it

will ensure that its product with Eshelby S-tensor - which is not symmetric - to regain symmetry and make the effective moduli matrix of the multiferroic composite also symmetric. The general expression of moduli matrix **L** applies to all phases, but for the piezoelectric phase, its piezomagnetic *q*-components are all zero, and for the piezomagnetic phase its piezoelectric *e*-components are also all zero. Besides, none of these two phases has the magnetoelectric coupling coefficients, α_{33} and α_{11}, but the general multiferroic composite has all 17 constants.

4.2.2. Effective electro-magneto-elastic moduli with a perfect interface

For the perfect interface case the effective properties of the aligned multiferroic composite as depicted in Fig. 4.1(a) can be evaluated by Mori-Tanaka method. Its formulation is entirely analogous to the purely elastic one as shown in Introduction. By taking the inclusions as phase 1 and matrix as phase 0, and denoting their respective volume concentrations as c_1 and c_0, and phase moduli as $\mathbf{L}_1$ and $\mathbf{L}_0$, respectively, we can write the effective electro-magneto-elastic moduli of multiferroic composites, $\mathbf{L}_e$, as

$$\begin{aligned} &\mathbf{L}_e = \left(c_0\mathbf{L}_0 + c_1\mathbf{L}_1\mathbf{A}_1\right)\left(c_0\mathbf{I} + c_1\mathbf{A}_1\right)^{-1}, \quad \text{or} \\ &\mathbf{L}_e = \mathbf{L}_0 + c_1\left(\mathbf{L}_1 - \mathbf{L}_0\right)\left[\mathbf{I} + c_0\mathbf{S}_1\mathbf{L}_0^{-1}\left(\mathbf{L}_1 - \mathbf{L}_0\right)\right]^{-1}, \end{aligned} \tag{4.8}$$

where $\mathbf{S}_1$ is the Eshelby S-tensor in the electro-magneto-elastic context, evaluated with the properties of the matrix phase, which can be piezoelectric or piezomagnetic, and the shape of inclusions. The procedure of its evaluation has been given in Appendix C. For a transversely isotropic piezoelectric (or piezomagnetic) matrix, it

generally needs to be calculated numerically by Gaussian quadrature, except that in fibrous (1-3) and lamellar (2-2) composites it has explicit result available. Matrix $\mathbf{A}_1$ is the coupled mechanical strain-electric field-magnetic field concentration tensor of a single piezomagnetic (or piezoelectric) ellipsoidal inclusion in the piezoelectric (or piezomagnetic) matrix, given by Eq. (1.2) with subscript *r* as 1. The two expressions given in Eq. (4.8) are identical, but the second version has been particularly simplified for two-phase composites and is easier to apply. In addition, this effective moduli tensor for the multiferroic composite containing aligned ellipsoidal inclusions also has the virtue that it coincides with or stays within Willis' bounds;[92] it will never violate the bounds.[93]

4.2.3. The interface effect

With an imperfect interface, we assume it to exist as a very thin layer of material between the ellipsoidal inclusion and the matrix. This thin layer and the piezoelectric (or piezomagnetic) inclusion are taken to form a thinly coated inclusion, in which the volume concentration of the interface (or more exactly, interphase) is denoted as c_{int}, and that of the inclusion as $(1-c_{\text{int}})$. We further assume that the interphase is amorphous, neither piezoelectric nor piezomagnetic, with an isotropic property, denoted by $\mathbf{L}_{\text{int}}$. This isotropic interphase assumption ensures that the thinly coated inclusion still has no magnetoelectric coupling, the same as the original inclusion. As a result $\mathbf{L}_{\text{int}}$ only has four independent constants, which can be represented by $\mathbf{L}_{\text{int}} = \left(C_{11}^{\text{int}}, C_{44}^{\text{int}}, \kappa^{\text{int}}, \mu^{\text{int}}\right)$. Its matrix form is given as

$$\mathbf{L}_{\text{int}}=\begin{bmatrix} C_{11}^{\text{int}} & C_{12}^{\text{int}} & C_{12}^{\text{int}} & 0 & 0 & 0 & 0 & 0 & 0 & 0 & 0 & 0 \\ C_{12}^{\text{int}} & C_{11}^{\text{int}} & C_{12}^{\text{int}} & 0 & 0 & 0 & 0 & 0 & 0 & 0 & 0 & 0 \\ C_{12}^{\text{int}} & C_{12}^{\text{int}} & C_{11}^{\text{int}} & 0 & 0 & 0 & 0 & 0 & 0 & 0 & 0 & 0 \\ 0 & 0 & 0 & C_{44}^{\text{int}} & 0 & 0 & 0 & 0 & 0 & 0 & 0 & 0 \\ 0 & 0 & 0 & 0 & C_{44}^{\text{int}} & 0 & 0 & 0 & 0 & 0 & 0 & 0 \\ 0 & 0 & 0 & 0 & 0 & C_{44}^{\text{int}} & 0 & 0 & 0 & 0 & 0 & 0 \\ 0 & 0 & 0 & 0 & 0 & 0 & -\kappa^{\text{int}} & 0 & 0 & 0 & 0 & 0 \\ 0 & 0 & 0 & 0 & 0 & 0 & 0 & -\kappa^{\text{int}} & 0 & 0 & 0 & 0 \\ 0 & 0 & 0 & 0 & 0 & 0 & 0 & 0 & -\kappa^{\text{int}} & 0 & 0 & 0 \\ 0 & 0 & 0 & 0 & 0 & 0 & 0 & 0 & 0 & -\mu^{\text{int}} & 0 & 0 \\ 0 & 0 & 0 & 0 & 0 & 0 & 0 & 0 & 0 & 0 & -\mu^{\text{int}} & 0 \\ 0 & 0 & 0 & 0 & 0 & 0 & 0 & 0 & 0 & 0 & 0 & -\mu^{\text{int}} \end{bmatrix}, \tag{4.9}$$

where $C_{12}^{\text{int}}=C_{11}^{\text{int}}-2C_{44}^{\text{int}}$. The property of the transversely isotropic inclusion is still denoted by $\mathbf{L}_1$. The effective property of the thinly coated inclusion, denoted by $\mathbf{L}_{\text{coat}}$, can then be represented by Eq. (4.8) again, as

$$\mathbf{L}_{\text{coat}}=\mathbf{L}_{\text{int}}+\left(1-c_{\text{int}}\right)\left(\mathbf{L}_1-\mathbf{L}_{\text{int}}\right)\left[\mathbf{I}+c_{\text{int}}\mathbf{S}_{\text{int}}\mathbf{L}_{\text{int}}^{-1}\left(\mathbf{L}_1-\mathbf{L}_{\text{int}}\right)\right]^{-1}, \tag{4.10}$$

where $\mathbf{S}_{\text{int}}$ is evaluated with the property of the interphase, $\mathbf{L}_{\text{int}}$. Due to the absence of electroelastic (or magnetoelastic) coupling in the interface, explicit expressions of the components of $\mathbf{S}_{\text{int}}$ are available for all inclusion aspect ratios. They are listed in Appendix C.

This thinly coated inclusion is then embedded into the original piezoelectric (or piezomagnetic) matrix to compute the effective electro-magneto-elastic moduli, $\mathbf{L}_e$, again by Eq. (4.8), where $\mathbf{L}_1$ is now replaced by $\mathbf{L}_{\text{coat}}$. In this way, the effective electro-magneto-elastic moduli matrix, $\mathbf{L}_e$, for multiferroic composites with an imperfect interface has been obtained.

The expressions in Eq. (4.8) and (4.10) involve some heavy computations that

touch upon the evaluation of S-tensor of the transversely isotropic piezoelectric (or piezomagnetic) spheroidal inclusion, but explicit results for α_{33} and α_{11} of the 1-3 and 2-2 composites have been worked out, for both perfect and imperfect interface cases. They are listed in Appendix D.

4.3. Results and discussion

We now present the results for the magnetoelectric coupling coefficients, α_{33} and α_{11}, of the BTO-CFO multiferroic composite. In addition, the magnetoelectric voltage coefficients, defined as $\alpha_{E33} = \alpha_{33}/\kappa_{33}$, and $\alpha_{E11} = \alpha_{11}/\kappa_{11}$, will also be given. This is another important set of parameters in the experimental measurement of magnetoelectric coupling. The material constants of each phase are listed in Table III. We use the first set in the left two columns taken from Huang and Kuo[17] and Li and Dunn[18] in all calculations, and use the second set in the right two columns obtained from Harshé *et al*.[35] to make comparison with their experiment at the end. The first set of material constants has been widely used in the literature. With it, our results for the perfect interface case can be directly compared with those given by Nan,[15] Huang and Kuo,[17] Li and Dunn,[18] and Srinivas *et al*.[38] Even though their calculations did not cover all the cases considered here, we have found that, for those available, general agreement is observed. In particular, the results given by Li and Dunn[18] for fibrous and multilayers are in complete agreement with our results. To illustrate the interface effects, we have taken the interface volume concentration to be 1% of the coated inclusion ($c_{\text{int}} = 0.01$) and adopted a weak interface model with the following material

constants: $C_{11}^{\text{int}} = 3\times10^{9}$ Pa, $C_{44}^{\text{int}} = 1\times10^{9}$ Pa, $\kappa^{\text{int}} = 2\varepsilon_0$, and $\mu^{\text{int}} = 2\mu_0$. And the constants $\varepsilon_0 = 8.854\times10^{-12}$ F/m and $\mu_0 = 1.257\times10^{-6}$ H/m are the vacuum permittivity and vacuum permeability, respectively.

Table III. Material constants of BTO-CFO composites used in numerical calculations.

Source	Huang and Kuo (1997) and Li and Dunn (1998)		Harshé *et al.* (1993)	
Phase	BTO	CFO	BTO	CFO
C_{11} GPa	166	286	283	284
C_{12} GPa	77	173	186	171
C_{13} GPa	78	170	142	168
C_{33} GPa	162	269.5	178	268
C_{44} GPa	43	45.3	43	45.3
e_{31} C/m^2	-4.4	0	-9.69	0
e_{33} C/m^2	18.6	0	11.7	0
e_{15} C/m^2	11.6	0	11.6	0
q_{31} N/(A·m)	0	550	0	574
q_{33} N/(A·m)	0	580.3	0	695
q_{15} N/(A·m)	0	699.7	0	550
κ_{11} C^2/(N·m^2)	11.2×10^{-9}	0.08×10^{-9}	11.2×10^{-9}	0.08×10^{-9}
κ_{33} C^2/(N·m^2)	12.6×10^{-9}	0.093×10^{-9}	8.2×10^{-9}	0.089×10^{-9}
μ_{11} N/A^2	5×10^{-6}	590×10^{-6}	5×10^{-6}	590×10^{-6}
μ_{33} N/A^2	10×10^{-6}	157×10^{-6}	10×10^{-6}	157×10^{-6}

The case of CFO-in-BTO (CFO inclusions in BTO matrix) composites will be given first from Fig. 4.2 to Fig. 4.5, followed by the BTO-in-CFO results from Fig. 4.6 to 4.9. In each figure five different aspect ratios are illustrated. These 8 figures provide the interface effects as a function of inclusion volume concentration, c_1. The same order is also adopted from Fig. 4.10 to Fig. 4.17, but plotted as a function of inclusion aspect ratio, α, at three different inclusion concentrations. In the last figure, Fig. 4.18, comparison with experiment is made. In each figure the results for the perfect interface are shown in (a) and those for the imperfect interface in (b) to highlight their difference.

4.3.1. Interface effects and inclusion concentration dependence

For the CFO-in-BTO composites, the magnitudes of α_{33} and α_{11}, and α_{E33} and α_{E11}, as a function of volume concentration of CFO inclusions, c_1, are given from Fig. 4.2 to Fig. 4.5. Figures 4.2(a) and 4.2(b) show the effective magnetoelectric coupling coefficient α_{33}. The top curve for the fibrous composite is seen to provide the strongest coupling whereas the multilayer has very little effect. As the aspect ratio decreases from infinity to the prolate shape of 10, then to the spherical shape of 1, and to the oblate shape of 0.5, this coupling coefficient is seen to steadily decrease. The

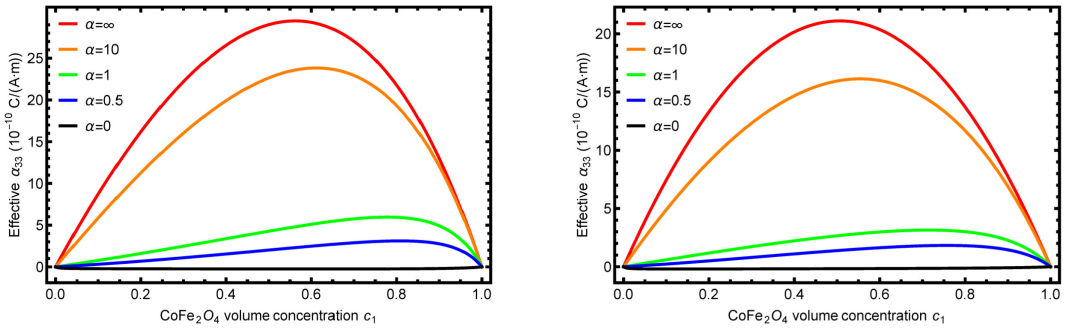

(a) (b)

FIG. 4.2. Inclusion concentration dependence of effective magnetoelectric coefficient α_{33} with (a) a perfect interface and (b) an imperfect interface. The matrix phase is $BaTiO_3$.

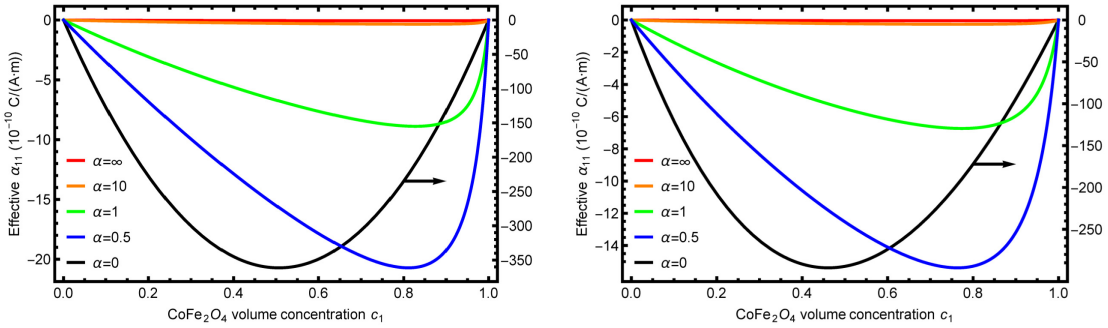

(a) (b)

FIG. 4.3. Inclusion concentration dependence of effective magnetoelectric coefficient α_{11} with (a) a perfect interface and (b) an imperfect interface. The matrix phase is $BaTiO_3$.

maximum value of α_{33} for each inclusion shape tends to occur at certain inclusion concentration, which shifts gradually to higher c_1 as the aspect ratio decreases. In all

cases the coupling coefficient returns to zero at both ends as pure BTO or CFO phase has no magnetoelectric coupling. By direct comparison between Fig. 4.2(a) to Fig. 4.2(b), the decrease of magnetoelectric coupling is evident due to the presence of weak interface.

The corresponding results for α_{11} with a perfect and an imperfect interface are given in Fig. 4.3(a) and 4.3(b), respectively. Along 1-direction, the values of α_{11} are negative, suggesting that the direction of induced electric displacement, D_1, is opposite to the applied magnetic field, H_1. This is in contrast to the dielectric effect in which the induced electric displacement has the same direction as the applied electric field, since κ_{11} and κ_{33} are always positive. Generally speaking the signs of α_{33} and α_{11} can be positive or negative as their values depend on the product of *e*- and *q*-components. For instance, the sign of α_{11} depends on the product, $-e_{15}q_{15}$, which is always negative according to the material constants used here. The explicit expressions given in Appendix D for the 1-3 and 2-2 composites make it more evident to see for these two extreme aspect ratios (e.g., see Eq. (D.21) and (D.22) for the 2-2 connectivity). It can also be observed that, for both perfect and imperfect interface, the general trend of the aspect-ratio dependence on α_{11} is exactly reversed from the α_{33} case. Multilayers now produce the strongest magnetoelectric coupling (note the horizontal arrow to the right vertical axis). Its maximum, at $-350\times10^{-10}\ \mathrm{C}/(\mathrm{A}\cdot\mathrm{m})$ for the perfect interface and $-300\times10^{-10}\,\mathrm{C}/(\mathrm{A}\cdot\mathrm{m})$ for the imperfect interface, are substantially higher than the $30\times10^{-10}\,\mathrm{C}/(\mathrm{A}\cdot\mathrm{m})$ maximum value of α_{33} for fibrous composites with a perfect interface and $20\times10^{-10}\,\mathrm{C}/(\mathrm{A}\cdot\mathrm{m})$ with an

imperfect interface in Fig. 4.2. The optimal CFO volume concentration that gives rise to the maximum α_{11} now shifts from about 0.5 for multilayers to higher c_1 as aspect ratio increases. By comparing Fig. 4.3(a) to 4.3(b), the value of α_{11} is seen to reduce as a result of imperfect interface (note the reduced scale).

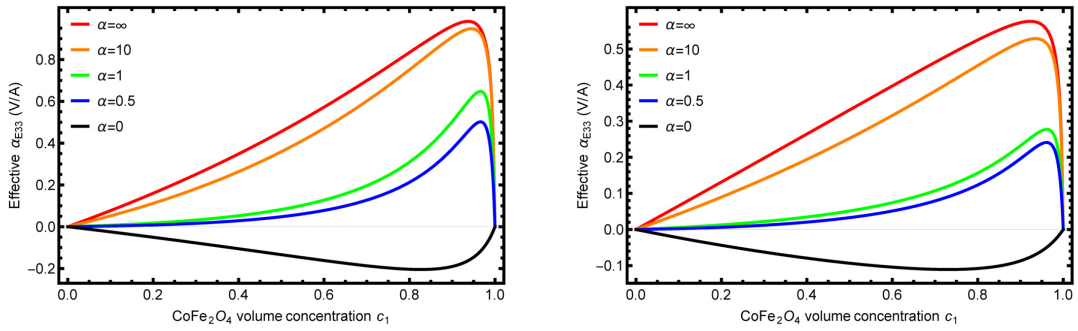

(a) (b)

FIG. 4.4. Inclusion concentration dependence of effective magnetoelectric voltage coefficient α_{E33} with (a) a perfect interface and (b) an imperfect interface. The matrix phase is $BaTiO_3$.

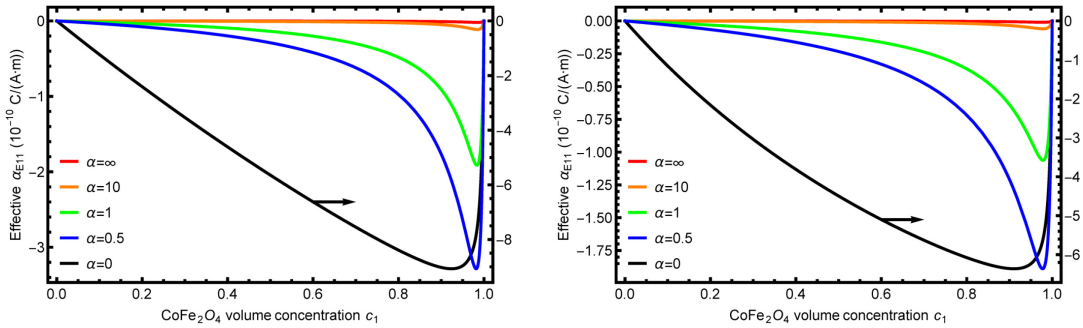

(a) (b)

FIG. 4.5. Inclusion concentration dependence of effective magnetoelectric voltage coefficient α_{E11} with (a) a perfect interface and (b) an imperfect interface. The matrix phase is $BaTiO_3$.

The results for the magnetoelectric voltage coefficient, α_{E33}, are shown in Fig. 4.4(a) and 4.4(b), with a perfect and an imperfect interface, respectively. These curves are to be read in direct comparison with those in Fig. 4.2. The main difference between the two comes from the definition of $\alpha_{E33} = \alpha_{33}/\kappa_{33}$, that it is affected by the effective electric permittivity, κ_{33}, of the composite. As κ_{33} of BTO is much higher than that of CFO, the κ_{33} of the composite will decrease with c_1. When divided by this quantity, the trend of α_{E33} will have its maximum shifted to a higher c_1. As a

consequence, all the curves in Fig. 4.4(a) and 4.4(b) shift horizontally to the right, with the maximum magnitude scaled by the κ_{33} value. With the multilayers, the voltage coupling coefficient is conspicuously negative, due to the negative, albeit small, value of α_{33} in Fig. 4.2. In all cases the voltage coupling coefficients for the imperfect interface are all lower than those with a perfect interface due to the weakening effect of the interface, but fibrous composites continue to exhibit the strongest coupling among all inclusion shapes.

Fig. 4.5(a) and 4.5(b) show the magnetoelectric voltage coefficient, α_{E11}, for the perfect and imperfect interface condition, respectively. This set is a result from Fig. 4.3 divided by κ_{11} of the composite. As with α_{E33}, its profiles display a horizontal shift from Fig. 4.3 due to the lower electric permittivity of CFO. The maxima for all inclusion shapes now all occur at higher value of c_1, while all curves return to zero at $c_1 = 0$ and 1.

For the BTO-in-CFO composites, the corresponding results are shown in Fig. 4.6 to 4.9, plotted as a function of BTO concentration, c_1. This c_1 is exactly equal to $(1 - c_1)$ in Fig. 4.2 to 4.5, but with a geometrical reversal. By comparing these two sets of data, we can read the influence of this geometrical interchange. For the magnetoelectric coefficient α_{33}, by comparing Fig. 4.6 to Fig. 4.2, we could see a broad similarity between the two cases, such as the strongest coupling occurs in fibrous composites and the lowest one in multilayers. With fibrous composites, the maximum values of α_{33} are nearly equal between these two sets, as in this case they generally follow the mixture rule in 3-direction. But with other aspect ratios, say with

$\alpha = 10$, the maximum value for BTO-in-CFO composites is now notably lower than that for CFO-in-BTO ones. This result suggests that CFO-in-BTO composites are superior to BTO-in-CFO systems. By comparing Fig. 4.6(b) to 4.6(a), we can also see that the magnitude of α_{33} with an imperfect interface is markedly reduced for each inclusion shape.

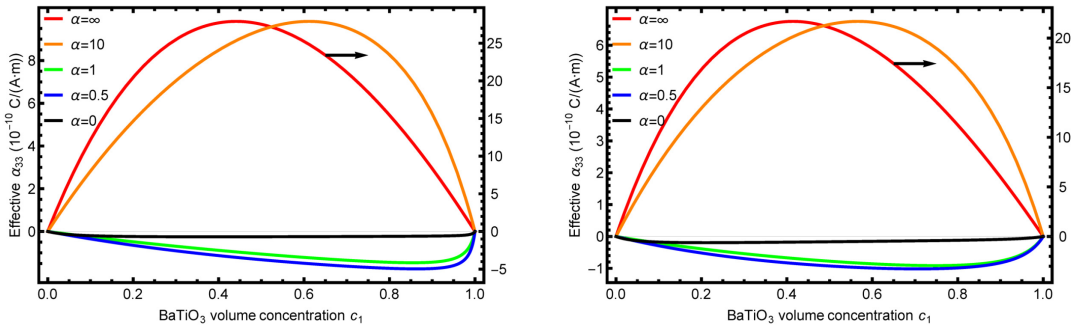

(a) (b)

FIG. 4.6. Inclusion concentration dependence of effective magnetoelectric coefficient α_{33} with (a) a perfect interface and (b) an imperfect interface. The matrix phase is $CoFe_2O_4$.

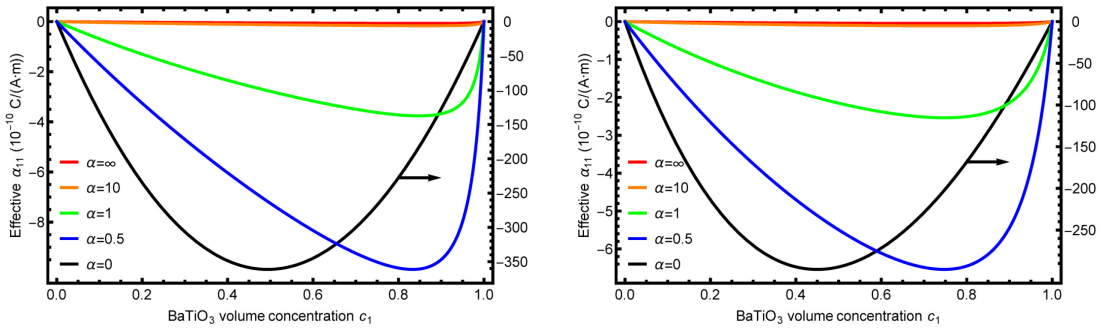

(a) (b)

FIG. 4.7. Inclusion concentration dependence of effective magnetoelectric coefficient α_{11} with (a) a perfect interface and (b) an imperfect interface. The matrix phase is $CoFe_2O_4$.

The features displayed in Fig. 4.7(a) and 4.7(b) also show notable weakening effect by the interface on α_{11}. Due to the symmetric nature of multilayers, the results with c_1 here are identical to those at $(1-c_1)$ in Fig. 4.3(a) and 4.3(b), for both perfect and imperfect interface. But with other inclusion shapes, say, spherical with $\alpha = 1$, the coupling coefficient for BTO-in-CFO are again lower than that for CFO-in-BTO.

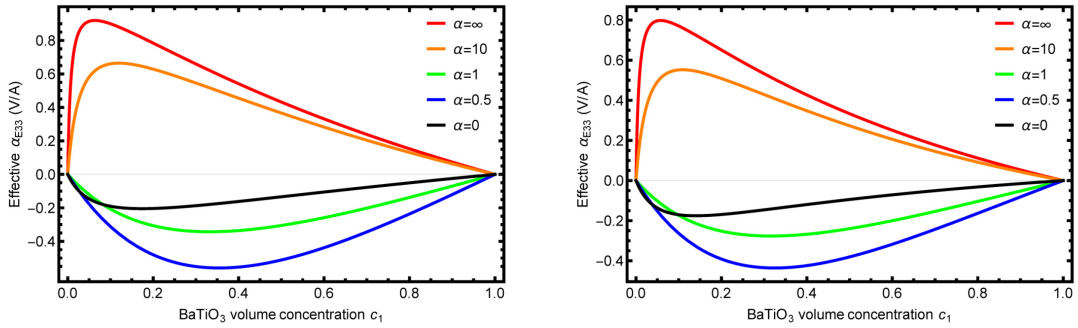

FIG. 4.8. Inclusion concentration dependence of effective magnetoelectric voltage coefficient α_{E33} with (a) a perfect interface and (b) an imperfect interface. The matrix phase is $CoFe_2O_4$.

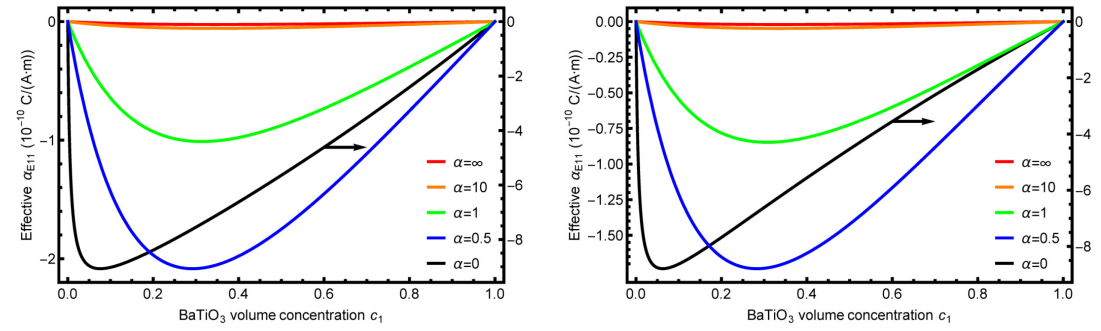

FIG. 4.9. Inclusion concentration dependence of effective magnetoelectric voltage coefficient α_{E11} with (a) a perfect interface and (b) an imperfect interface. The matrix phase is $CoFe_2O_4$.

The magnetoelectric voltage coefficient α_{E33} with a perfect and an imperfect interface are shown in Fig. 4.8(a) and 4.8(b), respectively. Weakening effect is not significant for fibrous composites because of the insignificant amount of interphase $c_{int} = 0.01$ and the closely related mixture rule, but for other inclusion shapes it is visible. By comparing Fig. 4.8 to Fig. 4.4, we observe that the maxima with all inclusion shapes shift to the left, to the lower BTO concentration, due to the fact that higher CFO concentration implies a lower κ_{33} and thus a higher α_{E33} of the composite. Another notable feature is that, with a perfect interface, the magnitudes of maxima for all inclusion shapes are also lower than those of CFO-in-BTO, confirming again the superiority of the latter system. But with an imperfect interface, the same conclusion cannot be drawn for the fibrous composite as α_{E33} is higher with

BTO-in-CFO. The voltage coefficient, α_{E11}, is shown in Fig. 4.9(a) and 4.9(b). Influence of an imperfect interface is again evident. Comparing this set of data to Fig. 4.5, we again observe that the maxima all shift to the left, to lower BTO concentration. But we also observe that the magnitudes of the maxima for CFO-in-BTO are not all higher than those for BTO-in-CFO. Unlike for α_{33} and α_{11}, similar conclusion for α_{E33} and α_{E11} that CFO-in-BTO is superior cannot be drawn.

4.3.2. Interface effects and inclusion aspect-ratio dependence

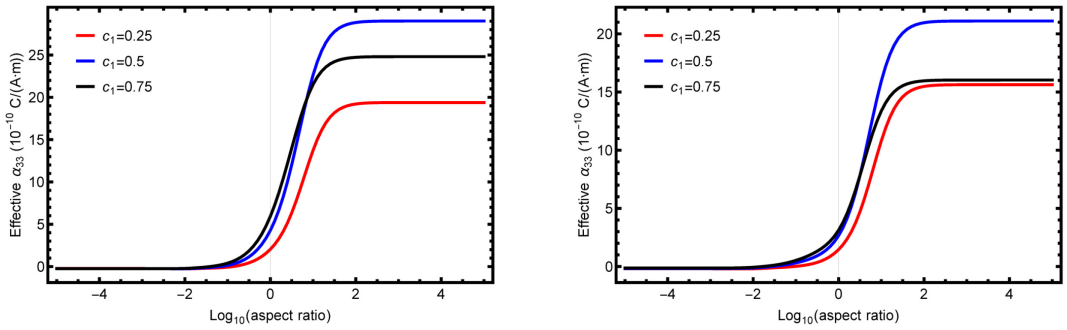

(a) (b)

FIG. 4.10. Inclusion aspect-ratio dependence of effective magnetoelectric coefficient α_{33} with (a) a perfect interface and (b) an imperfect interface. The matrix phase is $BaTiO_3$.

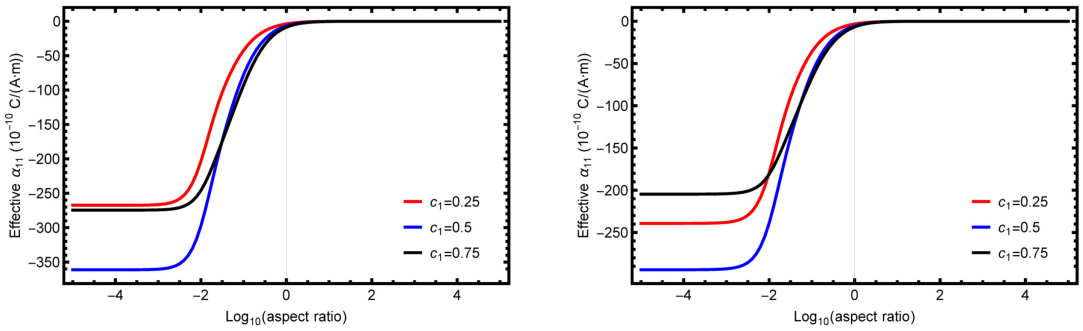

(a) (b)

FIG. 4.11. Inclusion aspect-ratio dependence of effective magnetoelectric coefficient α_{11} with (a) a perfect interface and (b) an imperfect interface. The matrix phase is $BaTiO_3$.

The continuous dependence of magnetoelectric coupling coefficients on the aspect ratio of inclusions is displayed from Fig. 4.10 to 4.17. For α_{33} of the CFO-in-BTO composite in Fig. 4.10, its marked improvement occurs only for the

prolate inclusions with $\alpha > 1$, and reaches the maximum for fibrous composites. For the oblate ones little is gained by changing the inclusion shape. This is true for both perfect and imperfect interface. For α_{11} shown in Fig. 4.11, the coupling coefficient is negative, and its magnitude is stronger with the oblate inclusions, reaching the maximum with multilayers. At each volume concentration, the interface effect is also evident by comparing Fig. 4.11(a) to 4.11(b).

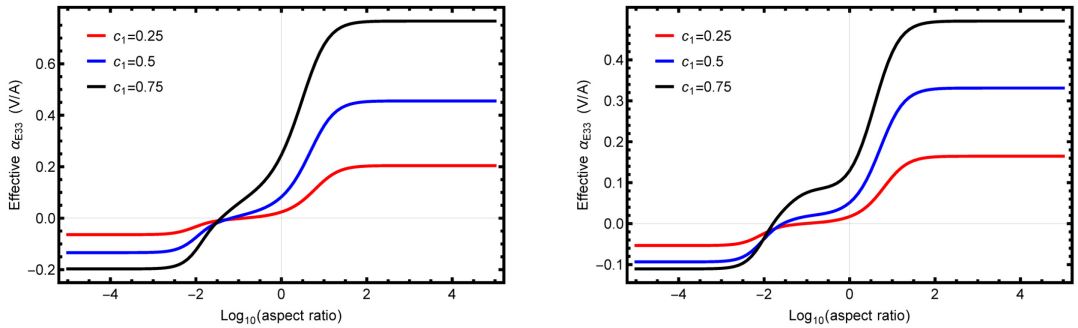

FIG. 4.12. Inclusion aspect-ratio dependence of effective magnetoelectric voltage coefficient α_{E33} with (a) a perfect interface and (b) an imperfect interface. The matrix phase is $BaTiO_3$.

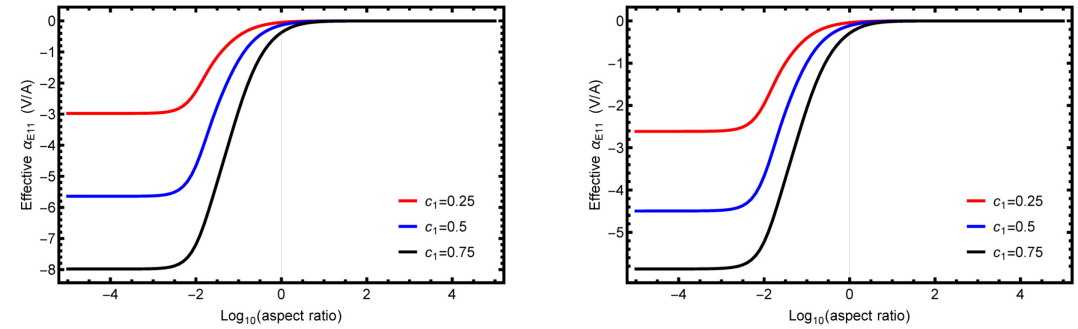

FIG. 4.13. Inclusion aspect-ratio dependence of effective magnetoelectric voltage coefficient α_{E11} with (a) a perfect interface and (b) an imperfect interface. The matrix phase is $BaTiO_3$.

The continuous dependence of the voltage coupling coefficient α_{E33} on the aspect ratio of CFO inclusions is shown in Fig. 4.12(a) and 4.12(b), for the perfect and imperfect interface conditions. The general trend that the coupling coefficient at each c_1 continues to increase with increasing aspect ratio remains the case, but, because α_{33} is actually negative (very small) with low aspect ratio ($\alpha < 0.01$), its value can

also be negative with oblate inclusions. In addition, lower CFO concentration, say at $c_1 = 0.25$, implies a higher BTO content and thus a higher κ_{33}, therefore α_{E33} is relatively lower as compared to $c_1 = 0.75$. Lower α_{E33} is also observed with the imperfect interface shown in Fig. 4.12(b). For α_{E11}, its dependence on the aspect ratio of CFO inclusions is displayed in Fig. 4.13(a) and 4.13(b). Multilayers again provide the highest coupling effect whereas prolate or fibrous composites have virtually zero coupling.

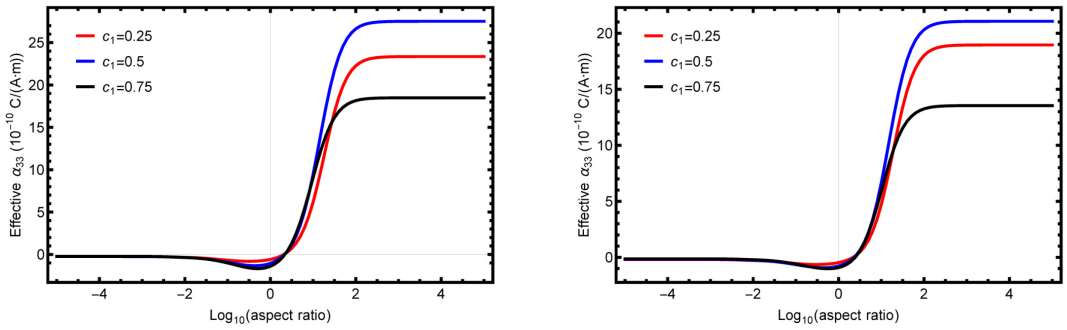

(a) (b)

FIG. 4.14. Inclusion aspect-ratio dependence of effective magnetoelectric coefficient α_{33} with (a) a perfect interface and (b) an imperfect interface. The matrix phase is $CoFe_2O_4$.

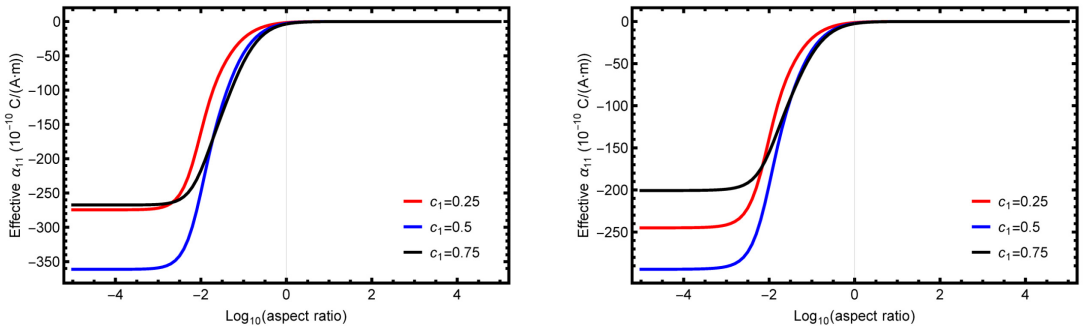

(a) (b)

FIG. 4.15. Inclusion aspect-ratio dependence of effective magnetoelectric coefficient α_{11} with (a) a perfect interface and (b) an imperfect interface. The matrix phase is $CoFe_2O_4$.

For the BTO-in-CFO composites, corresponding results are shown in Fig. 4.14 to 4.17, for the same four magnetoelectric coupling coefficients. Even with the geometrical reversal of two constituent phases, fibrous composites continue to lead the coupling effects (α_{33} and α_{E33}) in 3-direction, while multilayers give the

strongest ones (α_{11} and α_{E11}) along 1-direction. This holds for both perfect and imperfect interface conditions.

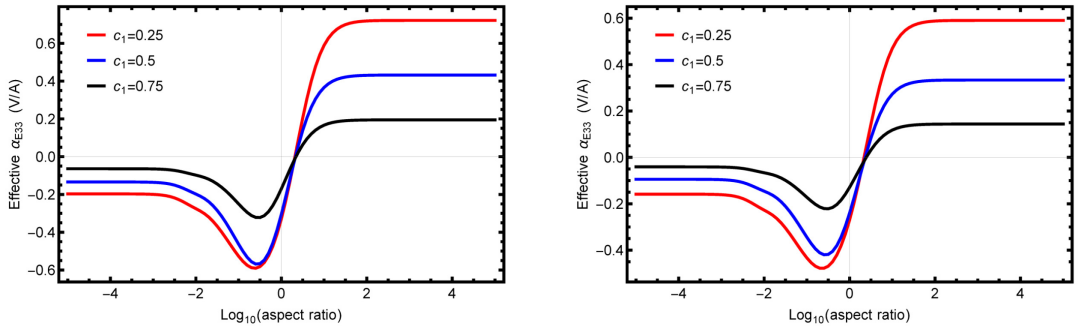

(a) (b)

FIG. 4.16. Inclusion aspect-ratio dependence of effective magnetoelectric voltage coefficient α_{E33} with (a) a perfect interface and (b) an imperfect interface. The matrix phase is $CoFe_2O_4$.

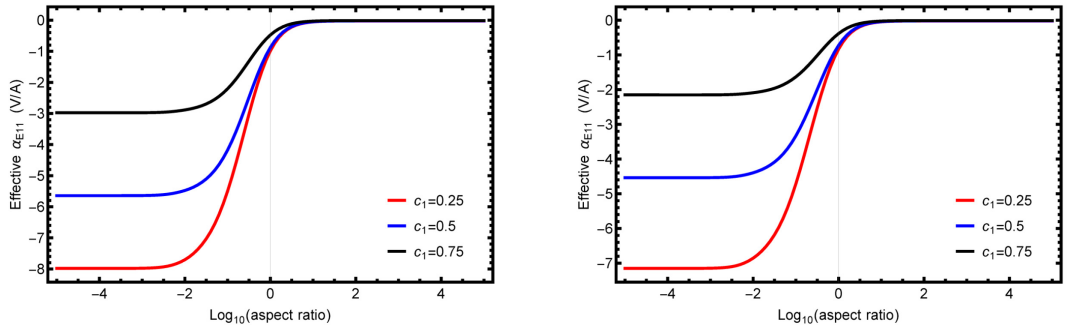

(a) (b)

FIG. 4.17. Inclusion aspect-ratio dependence of effective magnetoelectric voltage coefficient α_{E11} with (a) a perfect interface and (b) an imperfect interface. The matrix phase is $CoFe_2O_4$.

4.3.3. Comparison with experiment

We now demonstrate that experimentally measured magnetoelectric voltage coefficient, α_{E33}, of a CFO-in-BTO multiferroic composite generally falls lower than the theoretically predicted value based on the perfect interface condition, and that, with an imperfect interface, such data can be captured.

The experimental data of Harshé *et al.*[35] are reproduced in Fig. 4.18. The material constants of BTO and CFO used in this calculation are listed in the last two columns of Table III, which are obtained from the values in their paper (note: they

used the stress-based constitutive equations so their constants had to be converted to those of the strain-based constitutive equations as Eq. (4.3)) Their data were given at two volume concentrations of CFO, one at 11% and the other at 22%, both with a range of data as indicated by the error bar. We first use the perfect interface condition to obtain α_{E33}, and show them in the red curve (top one). The experimental data of the magnetoelectric voltage coupling coefficient are seen to be notably lower than this theoretical curve; it indicates that the perfect interface model predicts a coupling effect that cannot be delivered by the real system. We then compute another curve using a weak interface model, with $c_{\text{int}} = 0.02$ and the following material constants for interface properties: $C_{11}^{\text{int}} = 2\times10^9$ Pa, $C_{44}^{\text{int}} = 1\times10^9$ Pa, $\kappa^{\text{int}} = 2\varepsilon_0$, and $\mu^{\text{int}} = 2\mu_0$. The result is shown in the dark blue curve. It is seen that the lower experimental data now can be captured satisfactorily. This proves our assertion that the consideration of a weak interface is often essential to model a real system.

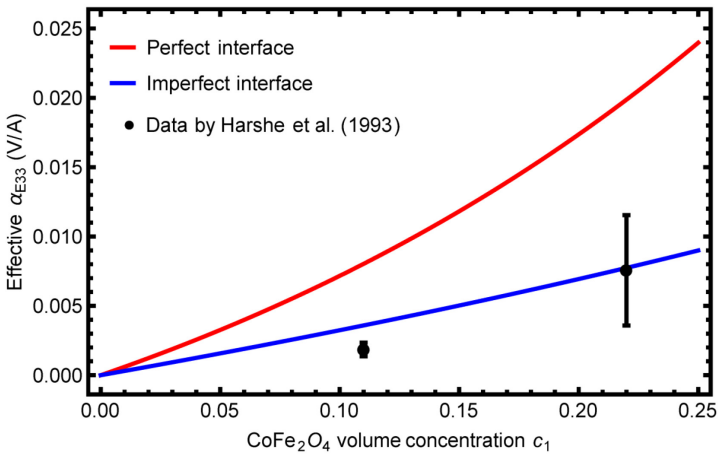

FIG. 4.18. Comparison between experiment and theory based on a perfect and an imperfect interface for the effective magnetoelectric voltage coefficient α_{E33} of a CFO-in-BTO composite.

4.4. Conclusions

In this chapter we have developed a composite theory to determine the interface effects and aspect-ratio dependence of magnetoelectric coupling in two-phase multiferroic composites. Our focus is on the piezoelectric-piezomagnetic system, with specific consideration for $BaTiO_3$ and $CoFe_2O_4$, in which one phase exists as aligned spheroidal inclusions and the other as the surrounding matrix. For the perfect interface case our model is built upon the Mori-Tanaka method. For the study of interface effects, we further introduce a thin layer of interphase between the inclusion and the matrix, to form a thinly coated inclusion that is subsequently embedded in the matrix. With the developed theory, we have first examined the case of CFO-in-BTO composites, and then BTO-in-CFO composites, to disclose the interface effect over the entire range of inclusion concentration from $c_1 = 0$ to 1, and the entire range of aspect ratio, α, from zero to infinity, to cover the widely used 2-2, 0-3, and 1-3 connectivities. Our calculations for the magnetoelectric coupling coefficients, α_{33} and α_{11}, and voltage coefficients, α_{E33} and α_{E11}, show a significant interface effect and aspect-ratio dependence for every term. A weak interface will universally lower the magnetoelectric coupling, while the aspect-ratio dependence is closely related to the specific loading direction. The results for α_{33} and α_{11} further indicate that CFO-in-BTO composites have stronger coupling coefficients than the BTO-in-CFO system, but for α_{E33} and α_{E11}, no such general conclusion could be drawn due to the additional influence of the κ_{33} and κ_{11} terms which are also dependent on the inclusion aspect ratio and interface condition. We have also demonstrated that the experimentally measured voltage coefficient, α_{E33}, of a CFO-in-BTO composite,

generally falls below the theoretical curve calculated from the ideal interface condition, and that, with the introduction of a weak interface, the measured data can be well captured.

Chapter 5.

Multiferroic composites: 0-0 and 1-1 connectivity

5.1. Overview

Magnetoelectric coupling effect in multiferroic composites consisting of piezoelectric and piezomagnetic phases with 0-0 and 1-1 connectivity is not a commonly studied subject. As illustrated in the schematic plots of Fig. 5.1 (where simple cubic blocks are used for easy rendering instead of spheres and cylinders), the geometrical settings of these two types of connectivity are quite particular that, unlike 0-3, 1-3 and 2-2 connectivity which have a clear inclusion-matrix type of geometry, both constituent phases now exist on equal geometrical footing. Thus different theoretical principles must be adopted in the determination of their overall properties. In this chapter we develop a continuum theory to examine the magnetoelectric coupling coefficients, α_{33} and α_{11}, for these two types of connectivity, and compare the results with those of the more commonly studied 0-3 and 1-3 composites. The computational process for solving the effective properties of 0-0 and 1-1 composites is highly nonlinear. With the BTO-CFO system, our study reveals that, for 0-0 connectivity, its α_{33} and α_{11} are substantially higher than those of 0-3 connectivity over a wide range of phase concentration, but that, with 1-1 connectivity, its α_{33} is only comparable to that of the 1-3 composite whereas its α_{11} is higher only within the range of 0.4 to 0.65 CFO vol.%. We have also calculated the effective values of the remaining 15 independent material constants of transversely isotropic multiferroic

composites, including 2 electric, 2 magnetic, 3 piezoelectric, 3 piezomagnetic, and 5 elastic constants, and found that most of these constants lie between those of the 0-3 and 1-3 composites with the CFO-in-BTO and BTO-in-CFO configurations. These remarkable features signify the importance of phase connectivity on magnetoelectric coupling and overall properties of multiferroic composites.

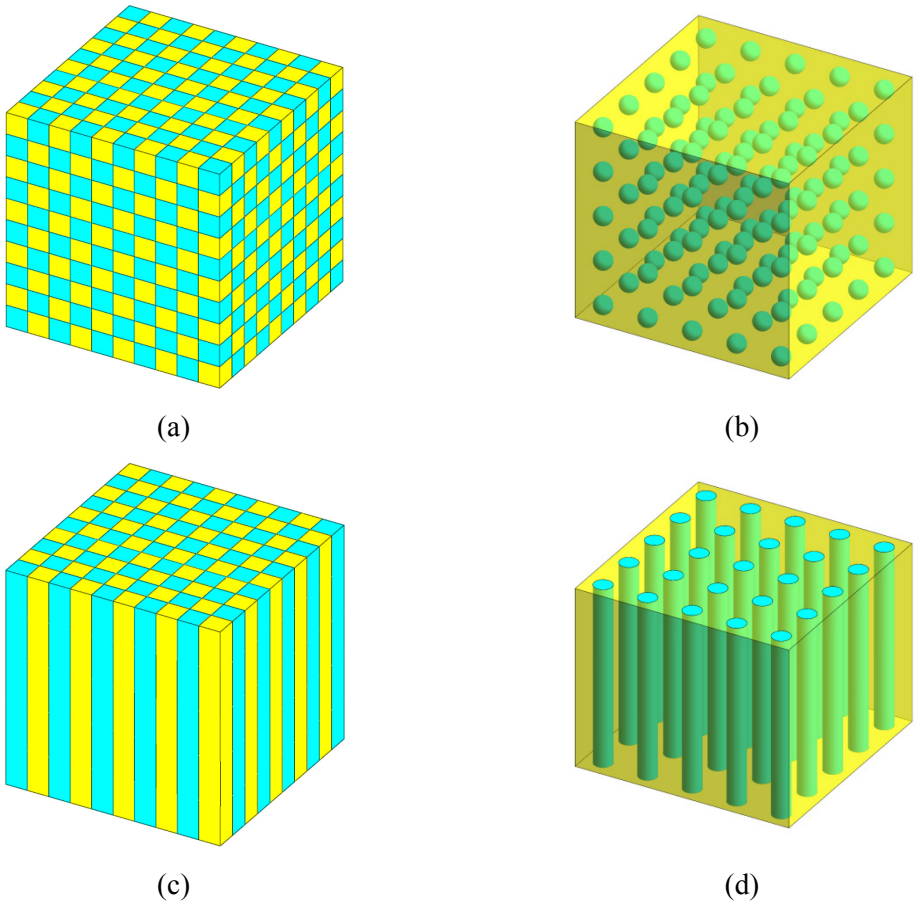

FIG. 5.1. Schematic plots of the piezoelectric-piezomagnetic multiferroic composites with: (a) 0-0 connectivity, (b) 0-3 connectivity, (c) 1-1 connectivity, and (d) 1-3 connectivity.

5.2. The theory

The microstructures of 0-0 and 1-1 connectivity as depicted in Fig. 5.1(a) and 5.1(c) are characterized by the symmetric appearance of the piezoelectric and the piezomagnetic phase. The effective properties of this type of microstructure can be

best studied by the effective-medium approach, which has been used in our previous chapters on CNT- and graphene-based nanocomposites. This approach has the merit of having a realizable microstructure, in which both phases have the same geometrical footing. In contrast, Fig. 5.1(b) and 5.1(d) for 0-3 and 1-3 connectivity are of the inclusion-matrix type whose effective magnetoelectric coupling could be conveniently studied by the Mori-Tanaka method. To evaluate the magnetoelectric coupling with 0-0 and 1-1 connectivity, we will first present the effective-medium approach for a transversely isotropic piezoelectric-piezomagnetic composite. It will be shown that, unlike electrical conductivity problem which has only one unknown quantity σ_e to solve, the present one is governed by an implicit matrix equation that involves 17 unknown constants.

5.2.1. Effective-medium approach for electro-magneto-elastic moduli

The two-phase effective-medium approach has already been derived in Introduction. The result of the effective electro-magneto-elastic moduli tensor of multiferroic composites, $\mathbf{L}_e$, is obtained by solving the following implicit equation

$$c_1\left[(\mathbf{L}_1-\mathbf{L}_e)^{-1}+\mathbf{S}_1\mathbf{L}_e^{-1}\right]^{-1}+c_2\left[(\mathbf{L}_2-\mathbf{L}_e)^{-1}+\mathbf{S}_2\mathbf{L}_e^{-1}\right]^{-1}=\mathbf{0}. \tag{5.1}$$

$\mathbf{S}_1$ and $\mathbf{S}_2$ are the S-tensors in the electro-magneto-elastic context, which are determined by the property of the effective medium (which is the effective property $\mathbf{L}_e$) and the shape of each individual phase. In 0-0 and 1-1 connectivity, since both phases share the same shape, we then have $\mathbf{S}_1=\mathbf{S}_2\equiv\mathbf{S}$. Therefore Eq. (5.1) can be simplified as

$$\mathbf{S}\mathbf{L}_e^{-1} + c_1\left(\mathbf{L}_2 - \mathbf{L}_e\right)^{-1} + c_2\left(\mathbf{L}_1 - \mathbf{L}_e\right)^{-1} = \mathbf{0}. \tag{5.2}$$

This equation is symmetric about subscript 1 and 2, which reflects the nature of effective-medium approach that both phases have equal geometrical footing. Eq. (5.2) is able to cover both 0-0 and 1-1 connectivity, and the difference between these two connectivities lies solely in the components of S-tensor in the transversely isotropic electro-magneto-elastic effective medium. These components are not known to have any explicit expressions, even though they are available with 1-3 connectivity. But their numerical results can be calculated with a general Gaussian quadrature algorithm, as described in Appendix C.

But it must be said that the solution to Eq. (5.2) for the effective $\mathbf{L}_e$ is still very complicated, as it involves the inverse of matrix $\mathbf{L}_e$ with 17 unknown constants as shown in Eq. (4.7), and it is to be multiplied by the S-tensor which further depends on these 17 constants. And then, there is another round of inversion. This is thus a highly nonlinear problem. In order to solve it, we have developed an incremental scheme to numerically calculate this $\mathbf{L}_e$ as the volume concentration of the piezoelectric or the piezomagnetic phase increases from 0 to 1. The details of this incremental procedure are listed in Appendix E.

We note in passing that the cases of 0-3 and 1-3 connectivity in Fig. 5.1(b) and 5.1(d) have been studied extensively, whose effective property can be given by

$$\mathbf{L}_e = \mathbf{L}_0 + c_1\left(\mathbf{L}_1 - \mathbf{L}_0\right)\left[\mathbf{I} + c_0\mathbf{S}_1\mathbf{L}_0^{-1}\left(\mathbf{L}_1 - \mathbf{L}_0\right)\right]^{-1}, \tag{5.3}$$

which has been given in Eq. (4.8). In Eq. (5.3), subscripts 0 and 1 respectively stand for the matrix and inclusion phases (we use subscript 1 and 2 in Eq. (5.2) since they

have equal geometrical footing). Unlike Eq. (5.2), it is explicit and simple to evaluate. In Chapter 4, we have analyzed the aspect-ratio dependence of the 2 magnetoelectric coupling coefficients, α_{33} and α_{11}, but we have not given the results for the rest 5 elastic, 3 piezoelectric, 3 piezomagnetic, 2 electric, and 2 magnetic constants. In order to reveal the merits of all the four configurations depicted in Fig. 5.1, we will also give these results here so that a full comparison between 0-0 and 0-3, and between 1-1 and 1-3, can be made. In computations, those cubic or rectangular blocks will be replaced by spherical particles or circular cylinders so that they are in line with those in 0-3 and 1-3 connectivity, and the periodic arrays will be considered to be randomly distributed. This assumption is necessary so that the effective-medium approach can be feasibly applied.

5.2.2. The interface effect

To account for the effect of an imperfect interface in the effective-medium approach, we envision the existence of a very thin layer of interphase, with the moduli tensor, $\mathbf{L}_{\text{int}}$, between the two phases. Due to the symmetric nature of the geometry of 0-0 and 1-1 connectivity, this layer is to be shared equally between the two phases, such that each inclusion becomes a coated one with a thin layer of interphase as coating. The volume concentration of coating interphase in the coated inclusion is denoted as c_{int}, so that, in this assemblage, the volume concentration of inclusion is $(1-c_{\text{int}})$. With such an inclusion-matrix configuration, the effective moduli tensor of the coated inclusion for phase 1 can be written as

$$\mathbf{L}_1^{\text{coat}} = \mathbf{L}_{\text{int}} + \left(1 - c_{\text{int}}\right)\left(\mathbf{L}_1 - \mathbf{L}_{\text{int}}\right)\left[\mathbf{I} + c_{\text{int}}\mathbf{S}_{\text{int}}\mathbf{L}_{\text{int}}^{-1}\left(\mathbf{L}_1 - \mathbf{L}_{\text{int}}\right)\right]^{-1}, \tag{5.4}$$

which is analogous to Eq. (5.3). The expression for $\mathbf{L}_2^{\text{coat}}$ can be obtained simply by replacing $\mathbf{L}_1$ with $\mathbf{L}_2$ in Eq. (5.4). These $\mathbf{L}_1^{\text{coat}}$ and $\mathbf{L}_2^{\text{coat}}$ will then respectively replace $\mathbf{L}_1$ and $\mathbf{L}_2$ in Eq. (5.2), to solve for the effective moduli tensor, $\mathbf{L}_e$, of the two-phase multiferroic 0-0 or 1-1 composites with an imperfect interface. As has been discussed in Chapter 4, the property of thin interphase should be taken to be isotropic, with $\mathbf{L}_{\text{int}} = \left(C_{11}^{\text{int}}, C_{44}^{\text{int}}, \kappa^{\text{int}}, \mu^{\text{int}}\right)$. The determination of S-tensor $\mathbf{S}_{\text{int}}$ is also the same as that given in Appendix C. In numerical calculations we take $C_{11}^{\text{int}} = 3\times10^9$ Pa, $C_{44}^{\text{int}} = 1\times10^9$ Pa, $\kappa^{\text{int}} = 2\varepsilon_0$, and $\mu^{\text{int}} = 2\mu_0$, which amount to a weak interface. In addition, as there is no interface at both $c_1 = 0$ and $c_1 = 1$, its volume concentration c_{int} must be zero at both ends. This can be satisfied with the function, $c_1^2\left(1-c_1\right)^2$. Therefore we take $c_{\text{int}} = 0.036\left(1-c_1\right)^2 c_1^2$ which gives $c_{\text{int}} = 0.00225$ at $c_1 = 0.5$, a very thin interface indeed.

5.3. Results and discussion

We now consider the specific system of $BaTiO_3$-$CoFe_2O_4$ (or BTO-CFO) composites. The properties of the individual piezoelectric BTO and the individual piezomagnetic CFO are listed in the left column of Table III. The 17 independent constants - in the order of α_{ij}, κ_{ij}, μ_{ij}, e_{ij}, q_{ij}, and C_{ij} - are to be presented first for 0-0 connectivity and then for 1-1 connectivity under both perfect and imperfect interface. In each case the results of 0-3 and 1-3 connectivity with perfect interface will also be plotted alongside for comparison.

5.3.1. Magnetoelectric coupling and overall properties of 0-0 composites

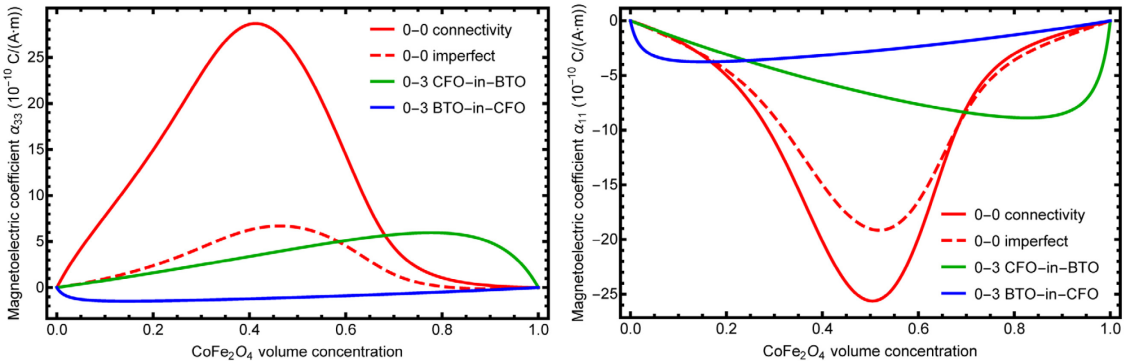

FIG. 5.2. Effective magnetoelectric coupling coefficients of 0-0 and 0-3 connectivity: (a) α_{33} and (b) α_{11}.

The calculated effective α_{33} and α_{11} of multiferroic composites as a function of CFO volume concentration are shown in Fig. 5.2(a) and 5.2(b), respectively. These two quantities are often referred to as the figures of merit for multiferroics. As neither the piezoelectric nor the piezomagnetic phase possesses such a property, it is the true product effect. In these figures the red curves are for 0-0 connectivity with a perfect interface calculated from Eq. (5.2), and the dashed red curves are with an imperfect interface calculated from Eq. (5.2) in conjunction with Eq. (5.4). The green and blue ones are for 0-3 connectivity with CFO-in-BTO and BTO-in-CFO configurations, both under a perfect interface calculated from Eq. (5.3). From Fig. 5.2(a), it is seen that the magnitude of α_{33} generated by 0-0 connectivity under a perfect interface is significantly higher than those of the CFO-in-BTO and BTO-in-CFO 0-3 composites over a wide range of CFO concentration. Its maximum reaches 30×10^{-10} C/(A·m) at the CFO concentration of 0.4. This is significantly higher than the maximum of 6×10^{-10} C/(A·m) reached by CFO-in-BTO later and -1.5×10^{-10} C/(A·m) by

BTO-in-CFO earlier. For α_{11} in Fig. 5.2(b), 0-0 connectivity again demonstrates its superior magnetoelectric coupling with a maximum of -25×10^{-10} C/(A·m) at the CFO concentration of 0.5; it is unmatched by the -9×10^{-10} C/(A·m) by CFO-in-BTO later and -4×10^{-10} C/(A·m) by BTO-in-CFO earlier. With an imperfect interface the coupling coefficients are notably reduced from the perfect interface case for both coupling coefficients.

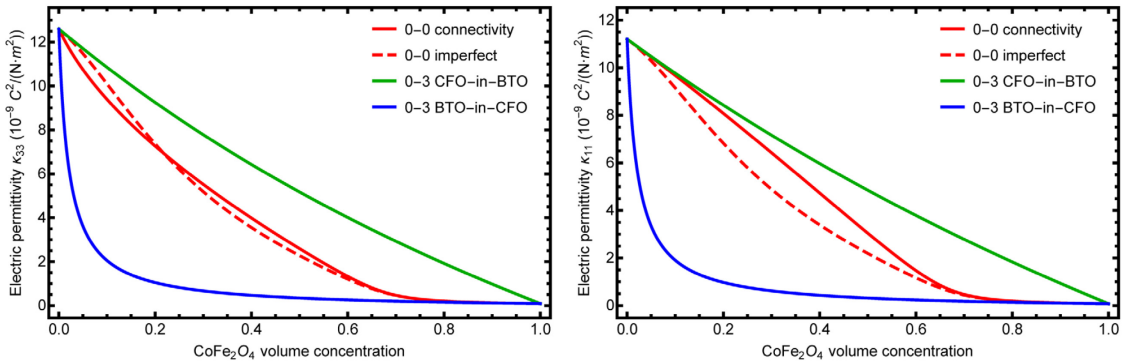

FIG. 5.3. Effective electric permittivity of 0-0 and 0-3 connectivity: (a) κ_{33} and (b) κ_{11}.

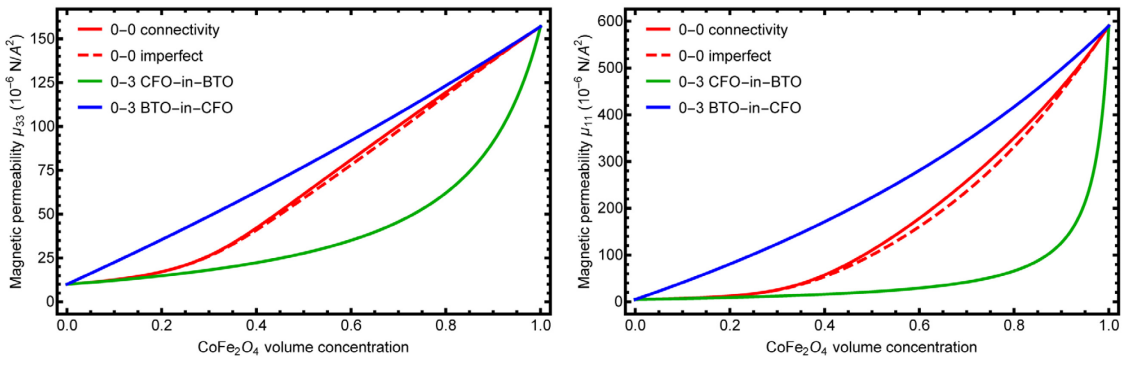

FIG. 5.4. Effective magnetic permeability of 0-0 and 0-3 connectivity: (a) μ_{33} and (b) μ_{11}.

The results for the effective electric permittivity, κ_{33} and κ_{11}, are shown in Fig. 5.3(a) and 5.3(b), respectively. Permittivity κ_{33} signifies the induced axial electric displacement, D_3, by a unit electric field E_3, while κ_{11} provides the same connection in the transverse direction. As the electric permittivity is strong in BTO but low in CFO, a continuous decrease of both quantities with increasing CFO

concentration is noted for all three types of composites. But what is remarkable here is that the permittivity of 0-0 connectivity always lies between those of CFO-in-BTO and BTO-in-CFO. This is reminiscent of the upper-bound nature of the Mori-Tanaka predictions of the isotropic moduli with isotropic spherical inclusions and matrix when the stronger phase (BTO here) serves as the matrix (CFO-in-BTO), and of the lower-bound nature when the weaker phase (CFO here) serves as the matrix (BTO-in-CFO). The results with the symmetric 0-0 connectivity are seen to always lie between the upper- and the lower-bound types of curves associated with the two 0-3 composites. The imperfect interface does not seem to have a significant impact on κ_{33} but its effect on κ_{11} is significant.

The two effective magnetic permeability curves, μ_{33} and μ_{11}, shown in Fig. 5.4(a) and 5.4(b), have similar characteristics. In this case CFO carries a substantially stronger permeability and thus both curves continue to increase with increasing CFO concentration. For both constants the 0-3 BTO-in-CFO composite carries an upper-bound type of characteristic whereas the 0-3 CFO-in-BTO has a lower bound one. The results with the symmetric 0-0 connectivity again lie between those of the two 0-3 connectivity curves. The weak interface causes both quantities to decrease but the influence is not strong.

The three effective piezoelectric constants of the multiferroic composite, e_{31}, e_{33} and e_{15}, are shown in Fig. 5.5(a) to 5.5(c). As these three properties are higher in BTO and zero in CFO, a continuous decrease from the respective BTO values to zero is also observed for all three types of composites. The magnitudes of the piezoelectric

constants for 0-3 CFO-in-BTO are always greater than those of 0-3 BTO-in-CFO at any given CFO concentration, whereas those of 0-0 connectivity are again seen to lie between the two. The imperfect interface causes the magnitude of both e_{31} and e_{15} to decrease, but for e_{33} a crossover is found.

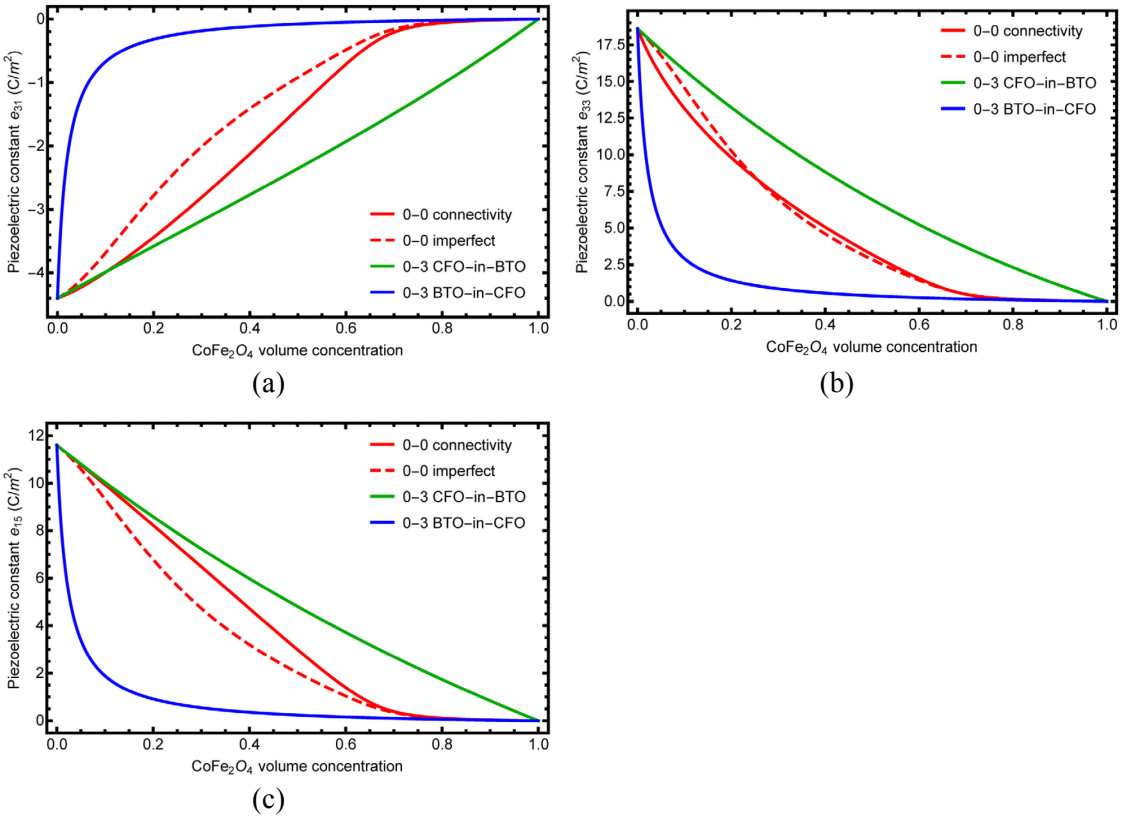

FIG. 5.5. Effective piezoelectric constants of 0-0 and 0-3 connectivity: (a) e_{31}, (b) e_{33} and (c) e_{15}.

The three effective piezomagnetic constants, q_{31}, q_{33} and q_{15}, are depicted in Fig. 5.6(a) to 5.6(c). Since CFO is the favored phase over BTO, the trends for all are continuously increasing with CFO concentration. Moreover, 0-3 BTO-in-CFO now shows higher piezomagnetic constants than 0-3 CFO-in-BTO at a given CFO volume concentration. But our calculations for 0-0 connectivity curve display a crossover with the 0-3 BTO-in-CFO curve for both q_{31} and q_{33}, even though it returns to the middle for q_{15}. Apparently, for such a highly anisotropic composite not every

component of the properties could be associated with the upper- or the lower-bound type of the curves. In fact explicit expressions of such bounds haven't even been reported in the literature. With an imperfect interface all three quantities are seen to be affected and lowered.

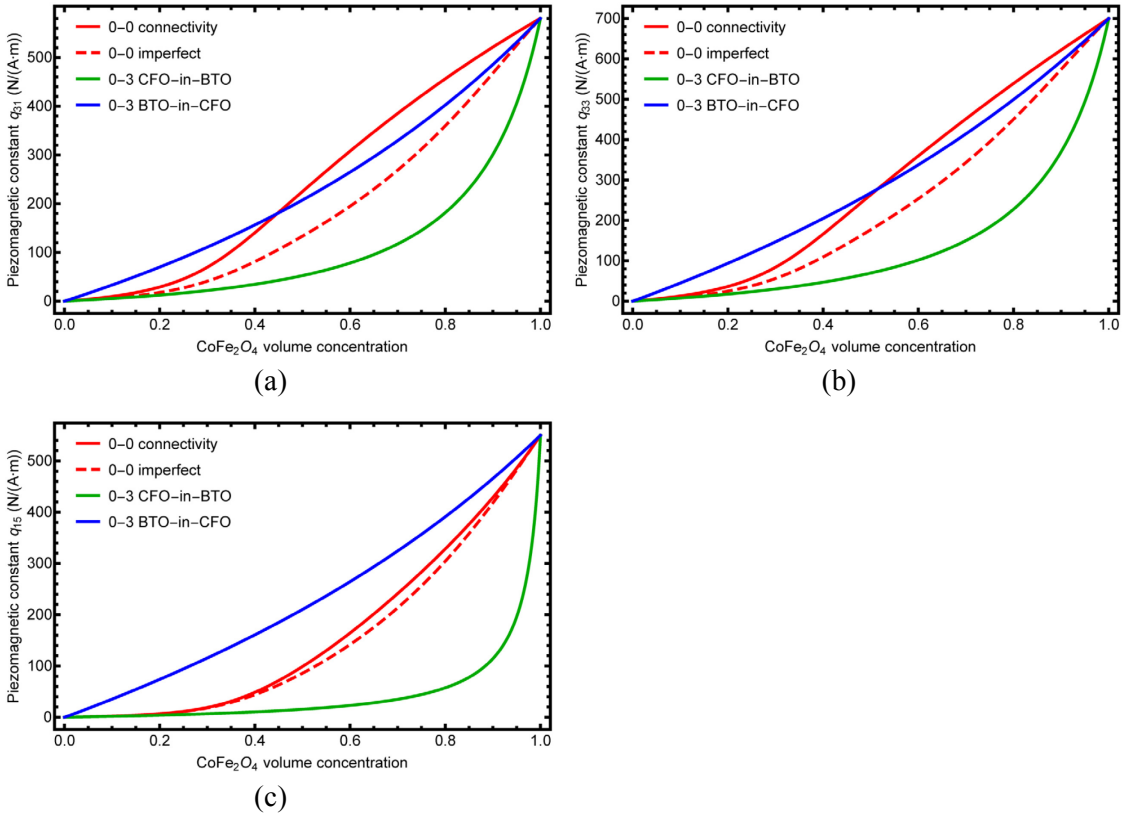

FIG. 5.6. Effective piezomagnetic constants of 0-0 and 0-3 connectivity: (a) q_{31}, (b) q_{33} and (c) q_{15}.

Finally we have the five effective elastic constants, C_{11}, C_{12}, C_{13}, C_{33} and C_{44}, that are shown in Fig. 5.7(a) to 5.7(e). The C_{11}, C_{12} and C_{13} curves of the two 0-3 composites are very close to each other and increase almost linearly with the CFO concentration, whereas those with 0-0 connectivity display slightly higher stiffness. For C_{33}, 0-3 BTO-in-CFO has a steeper gain initially, and a crossover is observed later. But it is C_{44}, the axial shear modulus, that has the most intriguing characteristic - its magnitude can be higher than either BTO or CFO phase at a given CFO volume

concentration. This remarkable property is exhibited in all three types of composites. It is, however, 0-0 connectivity that displays the highest magnitude at about 0.1 of CFO concentration. With an imperfect interface, the first four constants all decrease while a crossover is detected for C_{44}.

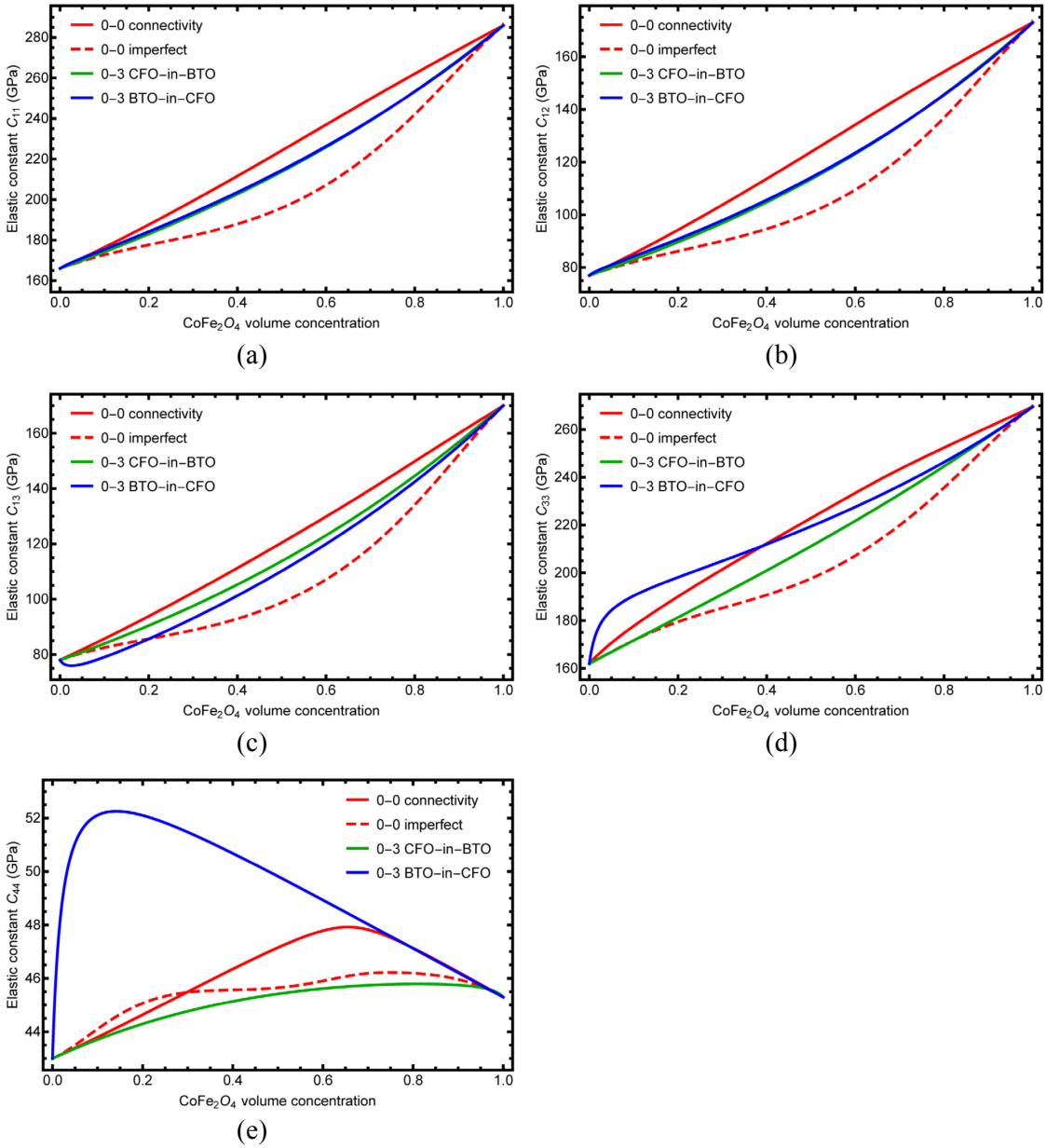

FIG. 5.7. Effective elastic constants of 0-0 and 0-3 connectivity: (a) C_{11}, (b) C_{12}, (c) C_{13}, (d) C_{33} and (e) C_{44}.

Summarizing these 0-0 and 0-3 studies, it can be said that: (i) the generation of the magnetoelectric coupling coefficients, α_{33} and α_{11}, (ii) the middle-ground

nature of 0-0 connectivity with respect to two 0-3 types in many properties, and (iii) the extraordinarily high value of C_{44}, are the three most intriguing features of the multiferroic composite here. When the interface is not perfect, most of the constants are found to be reduced from their counterparts with a perfect interface.

5.3.2. Magnetoelectric coupling and overall properties of 1-1 composites

With the symmetric, axial direction pointing along 3-direction and 1-2 plane isotropic, we now display the 17 calculated effective constants for 1-1 connectivity and compare them with the two 1-3 composites, CFO-in-BTO and BTO-in-CFO. The results with an imperfect interface will also be shown to disclose its effects.

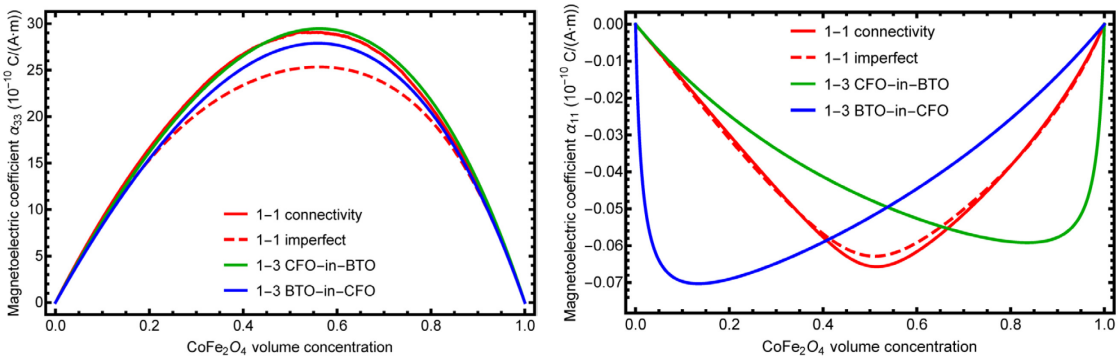

(a) (b)

FIG. 5.8. Effective magnetoelectric coupling coefficients of 1-1 and 1-3 connectivity: (a) α_{33} and (b) α_{11}.

The effective axial and transverse magnetoelectric coupling coefficients, α_{33} and α_{11}, are shown in Fig. 5.8(a) and 5.8(b), respectively. For α_{33}, the three types of composites are seen to exhibit very similar magnitudes over the entire range of CFO volume concentration. A small crossover between 1-1 and the 1-3 CFO-in-BTO lines is observed, however, and 1-3 CFO-in-BTO also displays a consistently higher coupling than 1-3 BTO-in-CFO. For α_{11} the characteristics of the three are widely

dispersed. Within the range of 0.4 to 0.65 CFO concentration, 1-1 connectivity provides a notably higher magnitude than the two 1-3 composites, but at the low and the high ends of CFO concentrations 1-3 BTO-in-CFO and 1-3 CFO-in-BTO respectively dominate the coupling coefficient α_{11}. In comparing Fig. 5.8(a) to Fig. 5.2(a), we also observe that the maximum α_{33} attained in 1-1 connectivity is comparable to that of 0-0 connectivity, both at about 30×10^{-10} C/(A·m). But the maximum of α_{33} for the two 1-3 composites are substantially higher than those of the two 0-3 composites. This trend, however, is reversed with α_{11}, for which the 1-1 and 1-3 composites could only generate a very small magnitude of magnetoelectric coupling. The imperfect interface is seen to cause both quantities to decrease from the perfect interface condition.

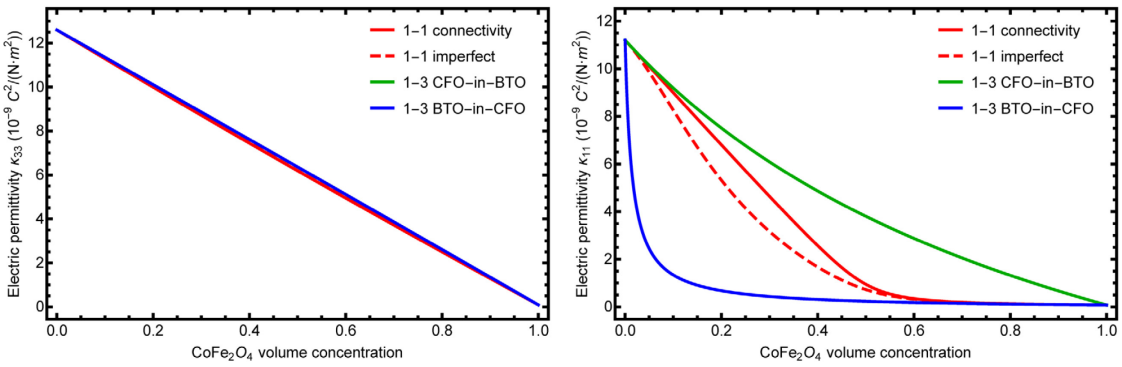

FIG. 5.9. Effective electric permittivity of 1-1 and 1-3 connectivity: (a) κ_{33} and (b) κ_{11}.

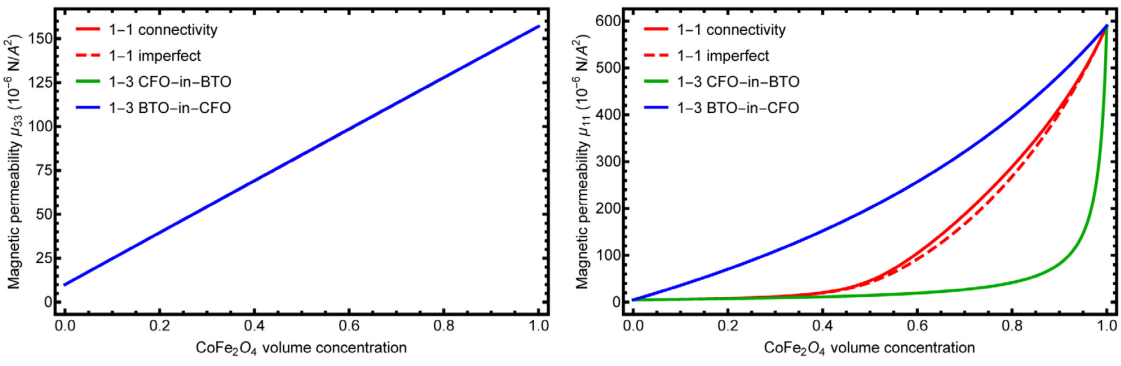

FIG. 5.10. Effective magnetic permeability of 1-1 and 1-3 connectivity: (a) μ_{33} and (b) μ_{11}.

The effective electric permittivity, κ_{33} and κ_{11}, are shown in Fig. 5.9(a) and 5.9(b), respectively. The axial coefficient κ_{33} is seen to decrease linearly for all composites, but the κ_{11} variations return to the now familiar pattern that 1-3 CFO-in-BTO is superior to 1-3 BTO-in-CFO, and that 1-1 connectivity lies between the two. While the general characteristics of κ_{11} displayed in Fig. 5.9(b) look strikingly similar to those in Fig. 5.3(b), the magnitudes associated with 1-3 connectivity are seen to be slightly lower than those of the 0-3 ones, regardless of CFO-in-BTO or BTO-in-CFO. With an imperfect interface the κ_{33} remains largely unaffected but κ_{11} value is notably lowered.

For μ_{33} and μ_{11}, the two effective magnetic permeability, the results are shown in Fig. 5.10(a) and 5.10(b). The axial permeability μ_{33}, like κ_{33}, is almost linear and very close for all cases, while the transverse permeability μ_{11} shows a reversed pattern to κ_{11}, since now CFO is the stronger phase. For μ_{11}, 1-1 connectivity initially behaves like 1-3 CFO-in-BTO but, after the CFO concentration exceeds 0.4, it takes off remarkably at the high concentration range. Its value is seen to be bounded between the two 1-3 composites. The effect of interface is found to be negligible for μ_{33} and weak for μ_{11}.

The three effective piezoelectric constants, e_{31}, e_{33} and e_{15}, are shown in Fig. 5.11(a) to 5.11(c). Constants e_{31} and e_{33} respectively characterize the induced axial electric displacement, D_3, due to a unit strain ε_1 and ε_3. These axial characteristics, as reflected in Fig. 5.11(a) and 5.11(b), are very linear and almost indistinguishable among the three composites. But the characteristics of e_{15}, which

signifies the induced transverse electric displacement, D_1, under a unit axial shear strain, ε_5, are quite nonlinear. Fig. 5.11(c) provides three distinctive curves that favor the 1-3 CFO-in-BTO composite. The magnitude of e_{15} for 1-1 connectivity clearly lies between the two 1-3 cases. The interface effect is stronger in both e_{31} and e_{15} with notable reductions, but is weak in e_{33}.

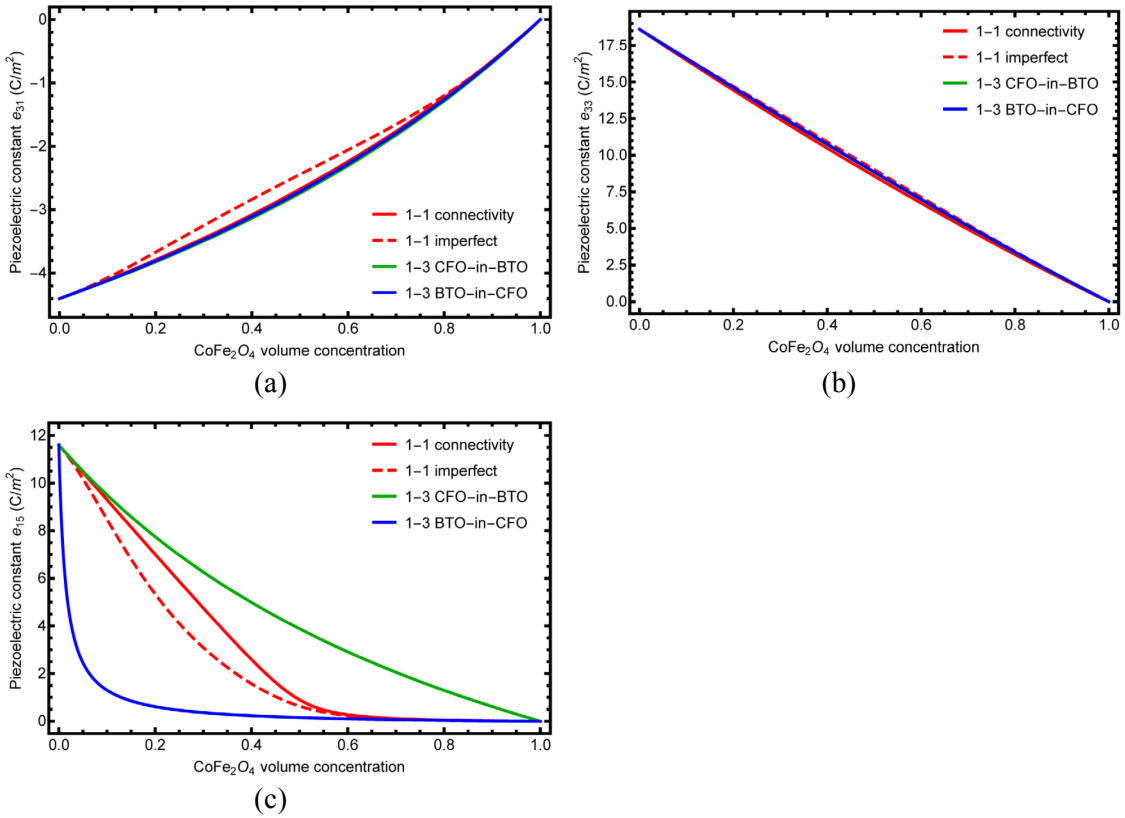

FIG. 5.11. Effective piezoelectric constants of 1-1 and 1-3 connectivity: (a) e_{31}, (b) e_{33} and (c) e_{15}.

The three effective piezomagnetic constants, q_{31}, q_{33} and q_{15}, are given in Fig. 5.12(a) to 5.12(c). The nearly linear dependence of both q_{31} and q_{33} can be explained similarly as the e_{31} and e_{33} above, only with the electric terms replaced by the corresponding magnetic terms. The nonlinear behavior of q_{15} also has a similar origin as that of e_{15}. In general, when the induced field is in the axial direction, the dependence is always close to linear, but when it is in the transverse

direction, nonlinear dependence will appear. Interface effects are observed for all three constants, all with some minor reductions.

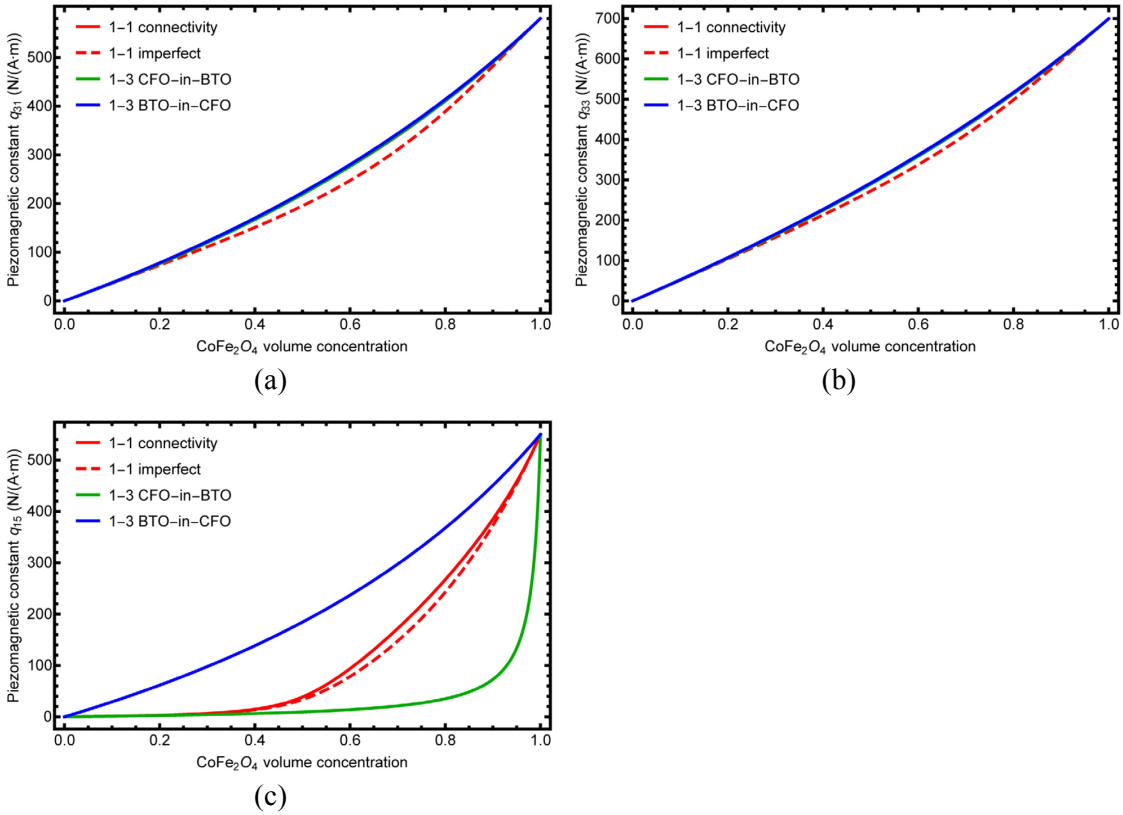

FIG. 5.12. Effective piezomagnetic constants of 1-1 and 1-3 connectivity: (a) q_{31}, (b) q_{33} and (c) q_{15}.

Finally, we have the five effective elastic constants, C_{11}, C_{12}, C_{13}, C_{33} and C_{44}, which are shown in Fig. 5.13(a) to 5.13(e). For the first four constants, their dependence on the CFO volume concentration are all very close to the linear behavior, and their magnitudes are virtually indistinguishable. It is again the axial shear modulus, C_{44}, as that of 0-0 connectivity, that exhibits the most remarkable electro-magneto-elastic coupling feature. Its effective values can far exceed the individual C_{44} of either the piezoelectric or the piezomagnetic phase. The results with an imperfect interface are notably lower for the first four constants, while for the last one a crossover is observed.

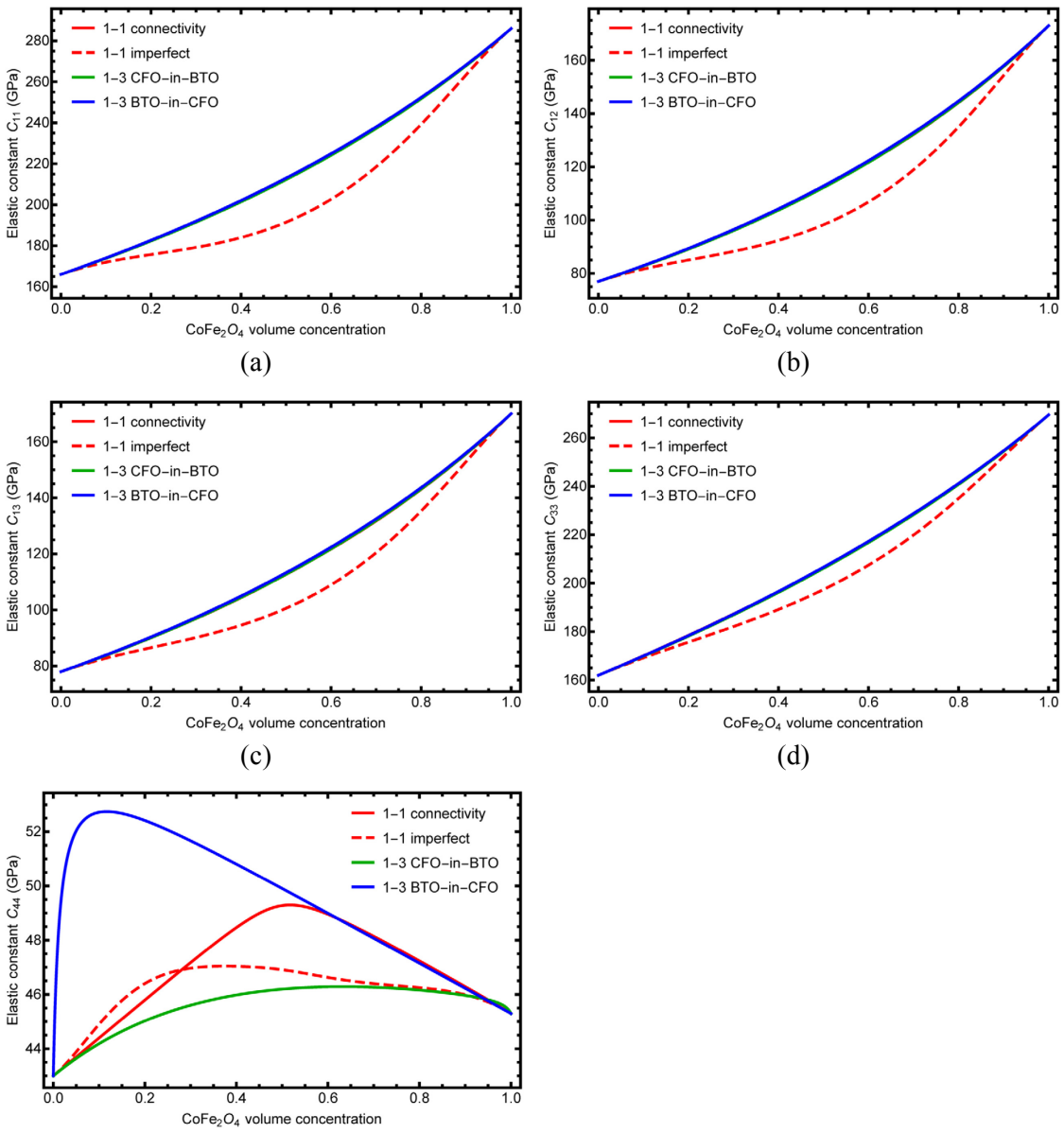

FIG. 5.13. Effective elastic constants of 1-1 and 1-3 connectivity: (a) C_{11}, (b) C_{12}, (c) C_{13}, (d) C_{33} and (e) C_{44}.

5.4. Conclusions

In this chapter we have implemented the effective-medium approach to study the nature of effective magnetoelectric coupling coefficients α_{33} and α_{11}, electric permittivity κ_{33} and κ_{11}, magnetic permeability μ_{33} and μ_{11}, piezoelectric constants e_{31}, e_{33} and e_{15}, piezomagnetic constants q_{31}, q_{33} and q_{15}, and elastic

constants C_{11}, C_{12}, C_{13}, C_{33} and C_{44}, of transversely isotropic multiferroic composites consisting of aligned piezoelectric and piezomagnetic phases with 0-0 and 1-1 connectivity, under both perfect and imperfect interface conditions. With the BTO-CFO system, we have also compared the calculated results with those of 0-3 and 1-3 connectivity with a perfect interface. Our calculations show remarkably high values of α_{33} and α_{11} within a wide range of CFO concentration for 0-0 connectivity. With 1-1 connectivity its α_{33} is only comparable to those of 1-3 CFO-in-BTO and 1-3 BTO-in-CFO, but its α_{11} is stronger than these two composites within the CFO concentration of 0.4 to 0.65. It is also found that, for 0-0 connectivity, its κ_{33} and κ_{11}, μ_{33} and μ_{11}, e_{31}, e_{33} and e_{15}, q_{15}, and C_{44}, all lie between those of the 0-3 type CFO-in-BTO and BTO-in-CFO. With 1-1 connectivity we have found that its κ_{11}, μ_{11}, e_{15}, q_{15}, and C_{44}, also lie between those of the 1-3 type CFO-in-BTO and BTO-in-CFO. We have also found that several property variations are quite linear; these include C_{11}, C_{12}, C_{13}, and C_{33} in the 0-0 and 0-3 cases, and κ_{33}, μ_{33}, e_{31}, e_{33}, q_{31}, q_{33}, C_{11}, C_{12}, C_{13}, and C_{33} in the 1-1 and 1-3 cases. Finally, remarkably high values of C_{44} that could far exceed the individual C_{44} of BTO and CFO are also discovered. For most properties an imperfect interface is found to have a significant effect to their magnitudes.

Chapter 6.

Future work

In the study of carbon-based nanocomposites, we have shown that the imperfect interface plays a crucial role in the determination of effective electrical conductivity. And in our current model the concept of interfacial resistivity is introduced to mathematically account for this interface effect. But one remaining problem is that, it is still not known yet what factors do interfacial resistivity ρ depend on. It is very important to find out the physical mechanism of ρ, and the formula to determine it. This is not a trivial problem, since interface effect involves lots of phenomena in condensed matter physics or even some quantum mechanics effects. The study on interfacial resistivity probably will go beyond the continuum level and call for more advanced theories in physics, nanotechnology and quantum mechanics.

On the other hand, our current study on multiferroic composites is limited to the linear behaviors, which is represented by the piezoelectric-piezomagnetic composites. However, in many multiferroic composites the material properties are ferroelectric and ferromagnetic, which are both nonlinear material properties. Lots of additional problems in the nonlinear behaviors, which are beyond the scope of current theory, need to be addressed. For example, ferroelectric and ferromagnetic materials are not homogenous, but consist of many individual domains. Applied external electric or magnetic field can switch these domains, causing the material properties to change. Their response to external fields not only depends on the magnitude, but also the history of external loading. Therefore it is important to investigate the physical

principle of domain switch. Another well-known characteristic of the nonlinear behavior of ferroelectric-ferromagnetic multiferroic composites is the hysteresis loop, as the one shown by the experimental results of Zheng *et al*.[94] More knowledge on the evolution of microstructural domains is apparently needed to analyze this nonlinear phenomenon. However the presented linear theory can serve as a starting point for a micromechanics-based nonlinear study, such as the works by Li and Weng[95] and Weng and Wong[96] in the study of domain switch in ferroelectric crystals. In this way, the mechanisms of polarization switch under a magnetic field and magnetization rotation under an electric field can be brought to light. This will be another main focus of our future study.

Appendix A.

Orientational average of tensors

In our 3-D random effective-medium approach, it is essential to calculate the orientational average of a tensor. We have given the result for a second-order tensor in previous chapter but without a formal derivation. Therefore in this appendix, we will show how to calculate the orientational average of a second-, third- and fourth-order tensor in details.

A.1. Orientational average of a second-order tensor

Let T_{ij} $(i, j = 1 \sim 3)$ be an arbitrary second-order tensor, the transformation of T_{ij}, $T_{ij}^{'}$, is given by

$$T_{ij}^{'} = \beta_{ik}\beta_{jl}T_{kl}, \tag{A.1}$$

where β_{ij} is the rotation matrix. The specific orientation in 3-D space can be represented by a set of Euler angles $(\varphi_1, \phi, \varphi_2)$, which denotes three consecutive rotations: (i) the first rotation is by an angle $\varphi_1 \in [0, 2\pi)$ about the original 3-axis; (ii) the second rotation is by an angle $\phi \in [0, \pi)$ about the new 1-axis; and (iii) the third rotation is by an angle $\varphi_2 \in [0, 2\pi)$ about the new 3-axis. All rotations follow the right hand rule. Consequently, we can express the rotation matrix β_{ij} in term of Euler angles $(\varphi_1, \phi, \varphi_2)$ as

$$\beta_{ij} = \begin{bmatrix} \cos\varphi_1\cos\varphi_2 - \sin\varphi_1\cos\phi\sin\varphi_2 & \sin\varphi_1\cos\varphi_2 + \cos\varphi_1\cos\phi\sin\varphi_2 & \sin\phi\sin\varphi_2 \\ -\cos\varphi_1\sin\varphi_2 - \sin\varphi_1\cos\phi\cos\varphi_2 & -\sin\varphi_1\sin\varphi_2 + \cos\varphi_1\cos\phi\cos\varphi_2 & \sin\phi\cos\varphi_2 \\ \sin\varphi_1\sin\phi & -\cos\varphi_1\sin\phi & \cos\phi \end{bmatrix}.$$

(A.2)

To calculate the orientational average of T_{ij}, denoted by $\overline{T}_{ij}$, we will integrate the $T_{ij}^{'}$ over the entire 3-D space, such that

$$\overline{T}_{ij} = \frac{1}{8\pi^2}\int_{\varphi_1=0}^{2\pi}\int_{\phi=0}^{\pi}\int_{\varphi_2=0}^{2\pi}\beta_{ik}\beta_{jl}T_{kl}\sin\phi d\varphi_1 d\phi d\varphi_2, \tag{A.3}$$

where

$$8\pi^2 = \int_{\varphi_1=0}^{2\pi}\int_{\phi=0}^{\pi}\int_{\varphi_2=0}^{2\pi}\sin\phi d\varphi_1 d\phi d\varphi_2. \tag{A.4}$$

This can be seen as the integration of a planer angle and a solid angle. Carrying out the integral in Eq. (A.3), we can get

$$\overline{T}_{ij} = \frac{1}{3}T_{kk}\delta_{ij}, \tag{A.5}$$

which is an isotropic second-order tensor. $\overline{T}_{ij}$ has only one unique component, which equals to the mean value of three diagonal components of T_{ij}. This is the reason why a tensor equation can be reduced to a scalar equation, as we have done in previous chapter.

A.2. Orientational average of a third-order tensor

Similarly, let T_{ijk} ($i, j, k = 1 \sim 3$) be an arbitrary third-order tensor, the transformation of T_{ijk}, $T_{ijk}^{'}$, is now given by

$$T_{ijk}^{'} = \beta_{il}\beta_{jm}\beta_{kn}T_{lmn}, \tag{A.6}$$

Then the orientational average of T_{ijk}, denoted by $\overline{T}_{ijk}$, can be obtained in a similar fashion

$$\begin{aligned}\overline{T}_{ijk} &= \frac{1}{8\pi^2}\int_{\varphi_1=0}^{2\pi}\int_{\phi=0}^{\pi}\int_{\varphi_2=0}^{2\pi}\beta_{il}\beta_{jm}\beta_{kn}T_{lmn}\sin\phi d\varphi_1 d\phi d\varphi_2 \\ &= \frac{1}{6}\left(\varepsilon_{lmn}T_{lmn}\right)\varepsilon_{ijk}.\end{aligned} \tag{A.7}$$

Here ε_{ijk} is the third-order permutation tensor. It has to be noted that in certain case, for example for the third-order piezoelectric moduli tensor e_{ijk}, we have symmetry $e_{ijk} = e_{ikj}$. Therefore its orientational average $\bar{e}_{ijk}$ is reduced to a zero tensor.

A.2. Orientational average of a fourth-order tensor

For an arbitrary fourth-order tensor T_{ijkl}, its transformation T'_{ijkl} is given by

$$T'_{ijkl} = \beta_{ip}\beta_{jq}\beta_{kr}\beta_{ls}T_{pqrs}. \tag{A.8}$$

Its orientational average $\overline{T}_{ijkl}$, is then calculated as

$$\begin{aligned}\overline{T}_{ijkl} &= \frac{1}{8\pi^2}\int_{\varphi_1=0}^{2\pi}\int_{\phi=0}^{\pi}\int_{\varphi_2=0}^{2\pi}\beta_{ip}\beta_{jq}\beta_{kr}\beta_{ls}T_{pqrs}\sin\phi d\varphi_1 d\phi d\varphi_2 \\ &= \frac{1}{3}T_{mmnn}J_{ijkl} + \frac{1}{5}\left(T_{mnmn} - \frac{1}{3}T_{mmnn}\right)K_{ijkl},\end{aligned} \tag{A.9}$$

where

$$J_{ijkl} = \frac{1}{3}\delta_{ij}\delta_{kl} \quad \text{and} \quad K_{ijkl} = \frac{1}{2}\left(\delta_{ik}\delta_{jl} + \delta_{il}\delta_{jk}\right) - \frac{1}{3}\delta_{ij}\delta_{kl}. \tag{A.10}$$

Eq. (A.9) is in accordance with the decomposition of an isotropic fourth-order tensor give by Walpole.[97] Therefore, like the second-order $\overline{T}_{ij}$, fourth-order $\overline{T}_{ijkl}$ is also an isotropic fourth-order tensor.

Appendix B.

Eight variants of multiferroic constitutive equations

There are eight different types of thermodynamic potentials that can be developed based on different choices of the (σ, ε), (D, E), and (B, H) pairs. This leads to eight different variants of the electro-magneto-elastic constitutive equations. Following the work of Soh and Liu,[98] they are listed as follows.

Type	Independent variables	Constitutive equations
1	ε, E, H	$\sigma = \mathbf{C}_{E,H}\varepsilon - \mathbf{e}_H^{\mathrm{T}}E - \mathbf{q}_E^{\mathrm{T}}H$ $D = \mathbf{e}_H\varepsilon + \boldsymbol{\kappa}_{\varepsilon,H}E + \boldsymbol{\alpha}_\varepsilon H$ $B = \mathbf{q}_E\varepsilon + \boldsymbol{\alpha}_\varepsilon E + \boldsymbol{\mu}_{\varepsilon,E}H$
2	σ, D, B	$\varepsilon = \mathbf{S}_{D,B}\sigma + \mathbf{g}_B^{\mathrm{T}}D + \mathbf{m}_D^{\mathrm{T}}B$ $E = -\mathbf{g}_B\sigma + \boldsymbol{\beta}_{\sigma,B}D - \boldsymbol{\lambda}_\sigma B$ $H = -\mathbf{m}_D\sigma - \boldsymbol{\lambda}_\sigma D + \boldsymbol{\upsilon}_{\sigma,D}B$
3	ε, D, H	$\sigma = \mathbf{C}_{D,H}\varepsilon - \mathbf{h}_H^{\mathrm{T}}D - \mathbf{q}_D^{\mathrm{T}}H$ $E = -\mathbf{h}_H\varepsilon + \boldsymbol{\beta}_{\varepsilon,H}D - \boldsymbol{\varsigma}_\varepsilon H$ $B = \mathbf{q}_D\varepsilon + \boldsymbol{\varsigma}_\varepsilon D + \boldsymbol{\mu}_{\varepsilon,D}H$
4	σ, E, B	$\varepsilon = \mathbf{S}_{E,B}\sigma + \mathbf{d}_B^{\mathrm{T}}E + \mathbf{m}_E^{\mathrm{T}}B$ $D = \mathbf{d}_B\sigma + \boldsymbol{\kappa}_{\sigma,B}E + \boldsymbol{\eta}_\sigma B$ $H = -\mathbf{m}_E\sigma - \boldsymbol{\eta}_\sigma E + \boldsymbol{\upsilon}_{\sigma,E}B$
5	ε, E, B	$\sigma = \mathbf{C}_{E,B}\varepsilon - \mathbf{e}_B^{\mathrm{T}}E - \mathbf{n}_E^{\mathrm{T}}B$ $D = \mathbf{e}_B\varepsilon + \boldsymbol{\kappa}_{\varepsilon,B}E + \boldsymbol{\eta}_\varepsilon B$ $H = -\mathbf{n}_E\varepsilon - \boldsymbol{\eta}_\varepsilon E + \boldsymbol{\upsilon}_{\varepsilon,E}B$
6	σ, D, H	$\varepsilon = \mathbf{S}_{D,H}\sigma + \mathbf{g}_H^{\mathrm{T}}D + \mathbf{p}_D^{\mathrm{T}}H$ $E = -\mathbf{g}_H\sigma + \boldsymbol{\beta}_{\sigma,H}D - \boldsymbol{\varsigma}_\sigma H$ $B = \mathbf{p}_D\sigma + \boldsymbol{\varsigma}_\sigma D + \boldsymbol{\mu}_{\sigma,D}H$
7	ε, D, B	$\sigma = \mathbf{C}_{D,B}\varepsilon - \mathbf{h}_B^{\mathrm{T}}D - \mathbf{n}_D^{\mathrm{T}}B$ $E = -\mathbf{h}_B\varepsilon + \boldsymbol{\beta}_{\varepsilon,B}D - \boldsymbol{\lambda}_\varepsilon B$ $H = -\mathbf{n}_D\varepsilon - \boldsymbol{\lambda}_\varepsilon D + \boldsymbol{\upsilon}_{\varepsilon,D}B$

8	σ, E, H	$\varepsilon = \mathbf{S}_{E,H}\sigma + \mathbf{d}_H^T E + \mathbf{p}_E^T H$ $D = \mathbf{d}_H \sigma + \boldsymbol{\kappa}_{\sigma,H} E + \boldsymbol{\alpha}_\sigma H$ $B = \mathbf{p}_E \sigma + \boldsymbol{\alpha}_\sigma E + \boldsymbol{\mu}_{\sigma,E} H$

In these constitutive equations, each subscript indicates that the corresponding tensor is measured under which kind of constant field. For instance, $\mathbf{C}_{E,H}$ means this elastic stiffness tensor is measured under constant electric and magnetic field, so its value is different from $\mathbf{C}_{E,B}$ which is measured under constant electric field and magnetic flux density. Each set of constitutive equations is related to a kind of electro-magneto-elastic moduli tensor, which can further be written in the Voigt and Nye contracted notations as a 12×12 moduli matrix. It has to be noted that, these moduli matrices are not necessarily symmetric. But in practice a symmetric moduli matrix is more desirable, so in some cases we rewrite the constitutive equations by giving some of the independent variables a negative sign, to make the moduli matrix symmetric. We have done this kind of change in previous chapter, but here we simply take all the eight kinds of moduli matrices in their original forms.

These eight kinds of moduli matrices are not independent, and actually from any one kind we can derive the other seven kinds. The way to transform one kind of moduli matrix to any other kind is presented as below:

(i) When all the independent variables are to be reversed, a direct inversion of the matrix is sufficient. For instance, given the moduli matrix for independent variables (ε, E, H), we can find that for (σ, D, B) through

$$\begin{bmatrix} \mathbf{S}_{D,B} & \mathbf{g}_B^{\mathrm{T}} & \mathbf{m}_D^{\mathrm{T}} \\ -\mathbf{g}_B & \boldsymbol{\beta}_{\sigma,B} & -\boldsymbol{\lambda}_\sigma \\ -\mathbf{m}_D & -\boldsymbol{\lambda}_\sigma & \boldsymbol{\upsilon}_{\sigma,D} \end{bmatrix} = \begin{bmatrix} \mathbf{C}_{E,H} & -\mathbf{e}_H^{\mathrm{T}} & -\mathbf{q}_E^{\mathrm{T}} \\ \mathbf{e}_H & \boldsymbol{\kappa}_{\varepsilon,H} & \boldsymbol{\alpha}_\varepsilon \\ \mathbf{q}_E & \boldsymbol{\alpha}_\varepsilon & \boldsymbol{\mu}_{\varepsilon,E} \end{bmatrix}^{-1}. \tag{B.1}$$

(ii) When only one or two independent variables are to be changed, a sequential conversion is needed. For example, given the moduli matrix for (ε, E, H), we can find that for (σ, E, H). In the first place we need to have the moduli matrices for both (ε, E, H) and (σ, D, B), which are already given in Eq. (B.1). Then we have the following relations

$$\begin{bmatrix} \sigma \\ D \\ B \end{bmatrix} = \begin{bmatrix} \mathbf{C}_{E,H} & -\mathbf{e}_H^{\mathrm{T}} & -\mathbf{q}_E^{\mathrm{T}} \\ \mathbf{e}_H & \boldsymbol{\kappa}_{\varepsilon,H} & \boldsymbol{\alpha}_{\varepsilon} \\ \mathbf{q}_E & \boldsymbol{\alpha}_{\varepsilon} & \boldsymbol{\mu}_{\varepsilon,E} \end{bmatrix} \begin{bmatrix} \varepsilon \\ E \\ H \end{bmatrix}. \tag{B.2}$$

At the same time, we also have

$$\begin{bmatrix} \varepsilon \\ D \\ B \end{bmatrix} = \begin{bmatrix} \mathbf{S}_{D,B} & \mathbf{g}_B^{\mathrm{T}} & \mathbf{m}_D^{\mathrm{T}} \\ \mathbf{0} & \mathbf{I} & \mathbf{0} \\ \mathbf{0} & \mathbf{0} & \mathbf{I} \end{bmatrix} \begin{bmatrix} \sigma \\ D \\ B \end{bmatrix}, \tag{B.3}$$

and

$$\begin{bmatrix} \sigma \\ E \\ H \end{bmatrix} = \begin{bmatrix} \mathbf{C}_{E,H} & -\mathbf{e}_H^{\mathrm{T}} & -\mathbf{q}_E^{\mathrm{T}} \\ \mathbf{0} & \mathbf{I} & \mathbf{0} \\ \mathbf{0} & \mathbf{0} & \mathbf{I} \end{bmatrix} \begin{bmatrix} \varepsilon \\ E \\ H \end{bmatrix}, \quad \text{thus} \quad \begin{bmatrix} \varepsilon \\ E \\ H \end{bmatrix} = \begin{bmatrix} \mathbf{C}_{E,H} & -\mathbf{e}_H^{\mathrm{T}} & -\mathbf{q}_E^{\mathrm{T}} \\ \mathbf{0} & \mathbf{I} & \mathbf{0} \\ \mathbf{0} & \mathbf{0} & \mathbf{I} \end{bmatrix}^{-1} \begin{bmatrix} \sigma \\ E \\ H \end{bmatrix}, \tag{B.4}$$

where the **0** and **I** denote the zero and identity matrix, respectively. With these relations we can get

$$\begin{aligned} \begin{bmatrix} \varepsilon \\ D \\ B \end{bmatrix} &= \begin{bmatrix} \mathbf{S}_{E,H} & \mathbf{d}_H^{\mathrm{T}} & \mathbf{p}_E^{\mathrm{T}} \\ \mathbf{d}_H & \boldsymbol{\kappa}_{\sigma,H} & \boldsymbol{\alpha}_{\sigma} \\ \mathbf{p}_E & \boldsymbol{\alpha}_{\sigma} & \boldsymbol{\mu}_{\sigma,E} \end{bmatrix} \begin{bmatrix} \sigma \\ E \\ H \end{bmatrix} \\ &= \begin{bmatrix} \mathbf{S}_{D,B} & \mathbf{g}_B^{\mathrm{T}} & \mathbf{m}_D^{\mathrm{T}} \\ \mathbf{0} & \mathbf{I} & \mathbf{0} \\ \mathbf{0} & \mathbf{0} & \mathbf{I} \end{bmatrix} \begin{bmatrix} \mathbf{C}_{E,H} & -\mathbf{e}_H^{\mathrm{T}} & -\mathbf{q}_E^{\mathrm{T}} \\ \mathbf{e}_H & \boldsymbol{\kappa}_{\varepsilon,H} & \boldsymbol{\alpha}_{\varepsilon} \\ \mathbf{q}_E & \boldsymbol{\alpha}_{\varepsilon} & \boldsymbol{\mu}_{\varepsilon,E} \end{bmatrix} \begin{bmatrix} \mathbf{C}_{E,H} & -\mathbf{e}_H^{\mathrm{T}} & -\mathbf{q}_E^{\mathrm{T}} \\ \mathbf{0} & \mathbf{I} & \mathbf{0} \\ \mathbf{0} & \mathbf{0} & \mathbf{I} \end{bmatrix}^{-1} \begin{bmatrix} \sigma \\ E \\ H \end{bmatrix}, \end{aligned} \tag{B.5}$$

which gives us the moduli matrix for (σ, E, H).

Appendix C.

Determination of electro-magneto-elastic S-tensor

C.1. General S-tensor

The electro-magneto-elastic S-tensor has been studied by Li and Dunn,[7] Huang *et al.*,[6] and several others. Here we briefly summarize the method for calculating this S-tensor with the notations used here. This method can be applied to multiferroic composites with ellipsoidal inclusions embedded in transversely isotropic matrix, and the aspect ratio of inclusions can range from 0 to ∞. But it also requires that the symmetric axis of ellipsoidal inclusions must coincide with the symmetric axis of the transversely isotropic property of the matrix.

First, we define a pseudo material constant "tensor" (which is not a real tensor by rigorous definition) $\mathbf{L}_{iJMn}$ for the matrix phase of multiferroic composites, with subscript $i,n=1\sim3$ and $J,M=1\sim5$,

$$\mathbf{L}_{iJMn}=\begin{cases}\mathbf{C}_{iJMn}, & J,M=1,2,3,\\ \mathbf{e}_{niJ}, & J=1,2,3,\ M=4,\\ \mathbf{q}_{niJ}, & J=1,2,3,\ M=5,\\ \mathbf{e}_{iMn}, & J=4,\ M=1,2,3,\\ \mathbf{q}_{iMn}, & J=5,\ M=1,2,3,\\ -\boldsymbol{\kappa}_{in}, & J=4,\ M=4,\\ -\boldsymbol{\alpha}_{in}, & J=4,\ M=5\ \&\ J=5,\ M=4,\\ -\boldsymbol{\mu}_{in}, & J=5,\ M=5.\end{cases} \tag{C.1}$$

With $\mathbf{L}_{iJMn}$, we introduce a 5×5 matrix $\mathbf{K}_{MJ}$,

$$\mathbf{K}_{MJ}=\mathbf{L}_{iJMn}x_i x_n, \tag{C.2}$$

where $x_i=\left[x_1,x_2,x_3\right]^{\mathrm{T}}$. Then we define another pseudo tensor $\mathbf{J}_{iJMn}$,

$$\mathbf{J}_{inMJ}\left(x_1, x_2, x_3\right) = x_i x_n \mathbf{K}_{MJ}^{-1}, \tag{C.3}$$

so that it is a function of x_1, x_2 and x_3. Next we integrate $\mathbf{J}_{iJMn}$ over the volume of an ellipsoidal inclusion $\Omega: x_1^2/a_1^2 + x_2^2/a_2^2 + x_3^2/a_3^2 \le 1$. When this spheroidal inclusion is symmetric about 3-direction, it satisfies $a_1 = a_2$, $\alpha = a_3/a_1$, where α is the aspect ratio of inclusion. Hence the volume integral of $\mathbf{J}_{iJMn}$ can be written as

$$\begin{aligned}\mathbf{H}_{inMJ} &= \int_\Omega \mathbf{J}_{inMJ}\left(x_1/a_1, x_2/a_2, x_3/a_3\right)dV = \int_\Omega \mathbf{J}_{inMJ}\left(x_1, x_2, x_3/\alpha\right)dV, \\ &= \int_{-1}^{1} d\tau \int_0^{2\pi} \mathbf{J}_{inMJ}\left(y_1, y_2, y_3/\alpha\right)d\tau d\theta,\end{aligned} \tag{C.4}$$

where the second equality is based on the fact that $\mathbf{J}_{iJMn}$ is a homogeneous function of order zero, thus multiplying all the variables by a_1 will not affect the integral. The third equality is given by applying a change of variables from x_1, x_2, x_3 to

$$y_1 = \sqrt{1-\tau^2}\cos\theta, \quad y_1 = \sqrt{1-\tau^2}\sin\theta, \quad y_3 = \tau, \tag{C.5}$$

with $\tau \in [-1, 1]$ and $\theta \in [0, 2\pi]$. Finally the S-tensor is determined by

$$\mathbf{S}_{MnAb} = \begin{cases} \dfrac{1}{8\pi}\mathbf{L}_{iJAb}\left(\mathbf{H}_{inMJ} + \mathbf{H}_{iMnJ}\right), & M = 1 \sim 3, \\ \dfrac{1}{4\pi}\mathbf{L}_{iJAb}\mathbf{H}_{in4J}, & M = 4, \\ \dfrac{1}{4\pi}\mathbf{L}_{iJAb}\mathbf{H}_{in5J}, & M = 5. \end{cases} \tag{C.6}$$

Still the electro-magneto-elastic S-tensor is a pseudo tensor. For the convenience of calculation it is generally converted into a 12×12 matrix by the Voigt and Nye contracted notations.

The integral in Eq. (C.4) can be analytically evaluated only when aspect ratio $\alpha = 0$ or ∞. For a general spheroid, it can be numerically carried out by using Gaussian quadrature, which turns the definite integral into a weighted sum of function values at specified points within the domain of integration. Thus Eq. (C.4) can be

rewritten as

$$\mathbf{H}_{inMJ} = \int_{-1}^{1} d\tau \int_{0}^{2\pi} \mathbf{J}_{inMJ}\left(y_1, y_2, y_3/\alpha\right) d\tau d\theta \approx \sum_{i=1}^{n} w_i f\left(\tau_i\right), \tag{C.7}$$

where $f\left(\tau\right) = \int_{0}^{2\pi} \mathbf{J}_{inMJ}\left(y_1, y_2, y_3/\alpha\right) d\theta$, n is the total number of specified points (usually $n = 20$ or more will provide enough accuracy), w_i is the weight at each specified point which can be constructed by different kinds of weight function. Up to this point the calculation of S-tensor is completed. In general, the S-tensor **S** is not symmetric, while $\mathbf{SL}^{-1}$ is always symmetric for any symmetric moduli matrix **L** of the matrix phase. This can be used as a criterion to check if the calculated components of S-tensor are correct.

C.2. Explicit S-tensor components for 1-3 and 2-2 connectivity

Explicit forms of the S-tensor are available for 1-3 fibrous composite ($\alpha \to \infty$) and 2-2 multilayered structure ($\alpha \to 0$). These two connectivities represent the most widely used microstructures and are frequently adopted in experiments. Their S-tensor components are summarized and listed below. It should be noted that the symmetric axis of the transversely isotropic property of the matrix lies on 3-direction, and 1-2 plane is isotropic.

Type	Piezoelectric matrix	Piezomagnetic matrix
1-3	$S_{11} = S_{22} = \frac{5C_{11} + C_{12}}{8C_{11}}$,	$S_{11} = S_{22} = \frac{5C_{11} + C_{12}}{8C_{11}}$,
	$S_{12} = S_{21} = -\frac{1}{8} + \frac{3C_{12}}{8C_{11}}$,	$S_{12} = S_{21} = -\frac{1}{8} + \frac{3C_{12}}{8C_{11}}$,

	$S_{13}=S_{23}=\dfrac{C_{13}}{2C_{11}},\quad S_{19}=S_{29}=\dfrac{e_{31}}{2C_{11}},$	$S_{13}=S_{23}=\dfrac{C_{13}}{2C_{11}},\quad S_{1,12}=S_{2,12}=\dfrac{q_{31}}{2C_{11}},$
	$S_{66}=\dfrac{3}{4}-\dfrac{C_{12}}{4C_{11}},$	$S_{66}=\dfrac{3}{4}-\dfrac{C_{12}}{4C_{11}},$
	$S_{44}=S_{55}=S_{77}=S_{88}=S_{10,10}=S_{11,11}=\dfrac{1}{2}.$	$S_{44}=S_{55}=S_{77}=S_{88}=S_{10,10}=S_{11,11}=\dfrac{1}{2}.$
	$S_{31}=S_{32}=\dfrac{e_{31}e_{33}+C_{13}\kappa_{33}}{{e_{33}}^2+C_{33}\kappa_{33}},$	$S_{31}=S_{32}=\dfrac{q_{31}q_{33}+C_{13}\mu_{33}}{{q_{33}}^2+C_{33}\mu_{33}},$
	$S_{57}=S_{48}=\dfrac{e_{15}}{C_{44}},$	$S_{5,10}=S_{4,11}=\dfrac{q_{15}}{C_{44}},$
2-2	$S_{91}=S_{92}=\dfrac{-C_{33}e_{31}+C_{13}e_{33}}{{e_{33}}^2+C_{33}\kappa_{33}},$	$S_{12,1}=S_{12,2}=\dfrac{-C_{33}q_{31}+C_{13}q_{33}}{{q_{33}}^2+C_{33}\mu_{33}},$
	$S_{33}=S_{44}=S_{55}=S_{99}=S_{12,12}=1.$	$S_{33}=S_{44}=S_{55}=S_{99}=S_{12,12}=1.$

Each 12×12 S-tensor has 144 components. All the other components are zero except for those listed above.

C.3. Explicit S-tensor components for isotropic interphase

In multiferroic composites, the interphase between the piezoelectric and piezomagnetic phase has isotropic property, as mentioned in previous chapter. In this case, the components of S-tensor have explicit results, for any aspect ratio of inclusion from $\alpha=0$ to ∞. They are given by[99]

$$S_{11}^{\text{int}}=S_{22}^{\text{int}}=\frac{3}{8(1-\nu_0)}\frac{\alpha^2}{\alpha^2-1}+\frac{1}{4(1-\nu_0)}\left[1-2\nu_0-\frac{9}{4(\alpha^2-1)}\right]g(\alpha),$$

$$S_{33}^{\text{int}}=\frac{1}{2(1-\nu_0)}\left\{1-2\nu_0+\frac{3\alpha^2-1}{\alpha^2-1}-\left[1-2\nu_0+\frac{3\alpha^2}{\alpha^2-1}\right]g(\alpha)\right\},$$

$$S_{12}^{\text{int}}=S_{21}^{\text{int}}=\frac{1}{4(1-\nu_0)}\left\{\frac{\alpha^2}{2(\alpha^2-1)}-\left[1-2\nu_0+\frac{3}{4(\alpha^2-1)}\right]g(\alpha)\right\},$$

$$
\begin{aligned}
&S_{13}^{\text{int}} = S_{23}^{\text{int}} = -\frac{1}{2(1-\nu_0)}\frac{\alpha^2}{\alpha^2-1} + \frac{1}{4(1-\nu_0)}\left\{\frac{3\alpha^2}{\alpha^2-1} - (1-2\nu_0)\right\} g(\alpha),\\
&S_{31}^{\text{int}} = S_{32}^{\text{int}} = -\frac{1}{2(1-\nu_0)}\left[1-2\nu_0+\frac{1}{\alpha^2-1}\right] + \frac{1}{2(1-\nu_0)}\left[1-2\nu_0+\frac{3}{2(\alpha^2-1)}\right] g(\alpha),\\
&S_{44}^{\text{int}} = S_{55}^{\text{int}} = \frac{1}{2(1-\nu_0)}\left\{1-2\nu_0-\frac{\alpha^2+1}{\alpha^2-1} - \frac{1}{2}\left[1-2\nu_0-\frac{3(\alpha^2+1)}{\alpha^2-1}\right] g(\alpha)\right\},\\
&S_{66}^{\text{int}} = \frac{1}{2(1-\nu_0)}\left\{\frac{\alpha^2}{2(\alpha^2-1)} + \left[1-2\nu_0-\frac{3}{4(\alpha^2-1)}\right] g(\alpha)\right\},\\
&S_{77}^{\text{int}} = S_{88}^{\text{int}} = S_{10,10}^{\text{int}} = S_{11,11}^{\text{int}} = \frac{1}{2} g(\alpha),\\
&S_{99}^{\text{int}} = S_{12,12}^{\text{int}} = 1 - g(\alpha),
\end{aligned}
\tag{C.8}
$$

and all the other components are zero. Here $\nu_0 = \left(C_{11}^{\text{int}} - 2C_{44}^{\text{int}}\right) \Big/ \left[2\left(C_{11}^{\text{int}} - C_{44}^{\text{int}}\right)\right]$, is the Poisson's ratio of the interphase, and auxiliary function $g(\alpha)$ depends on the aspect ratio α, as

$$
g(\alpha) = \begin{cases}
\dfrac{\alpha}{\left(1-\alpha^2\right)^{\frac{3}{2}}}\left[\cos^{-1}\alpha - \alpha\left(1-\alpha^2\right)^{\frac{1}{2}}\right], & \alpha < 1,\\
\dfrac{\alpha}{\left(\alpha^2-1\right)^{\frac{3}{2}}}\left[\alpha\left(\alpha^2-1\right)^{\frac{1}{2}} - \cosh^{-1}\alpha\right], & \alpha \geq 1.
\end{cases}
\tag{C.9}
$$

This set of S-tensor can reduce to the commonly used S-tensor for the uncoupled elastic, dielectric, or magnetic problem.

C.4. S-tensor for other kinds of constitutive equations

We have discussed the method to obtain the electro-magneto-elastic S-tensor, denoted as $\mathbf{S}^{(1)}$ (superscript 1 means "Type 1"), as given in Eq. (C.6). However this S-tensor is only for a particular kind of multiferroic constitutive equations, which has

independent variables $(\varepsilon, -E, -H)$. It is already known that there are eight kinds of constitutive equations, and their corresponding moduli matrices are interchangeable. Theoretically speaking, each kind of moduli matrix has its own S-tensor, and these eight kinds of S-tensor are also interchangeable. Here we provide the method to derive other kinds of S-tensor. Unlike the case of moduli matrices in which any one kind can be used to derive the other seven kinds, the derivation of S-tensors must start from $\mathbf{S}^{(1)}$. Because ε, E and H are all the gradients of certain potentials, so that only for this set of independent variables can we define multiferroic Green's function.

First let $\mathbf{L}^{(1)}$ be moduli matrix for independent variables $(\varepsilon, -E, -H)$, so the moduli matrix for (σ, D, B), denoted by $\mathbf{M}^{(1)}$, can be directly obtained by its inverse operation, which is $\mathbf{M}^{(1)} = \left(\mathbf{L}^{(1)}\right)^{-1}$. The S-tensor for $\mathbf{M}^{(1)}$ (which is usually call T-tensor), $\mathbf{T}^{(1)}$ is given by

$$\mathbf{T}^{(1)} = \mathbf{L}^{(1)}\left(\mathbf{I} - \mathbf{S}^{(1)}\right)\mathbf{M}^{(1)}. \tag{C.10}$$

By the definition in Eq. (1.1), we have the following relations for $\mathbf{S}^{(1)}$ and $\mathbf{T}^{(1)}$

$$\mathbf{Y} = \mathbf{S}^{(1)}\mathbf{Y}^{*} \quad \text{and} \quad \mathbf{X} = \mathbf{T}^{(1)}\mathbf{X}^{*}, \tag{C.11}$$

where **X** and **Y** have been given in Eq. (4.5). In addition, when the material is free from external field, **X** and **Y** also have the relations

$$\mathbf{X} = \mathbf{L}^{(1)}\left(\mathbf{Y} - \mathbf{Y}^{*}\right) \quad \text{and} \quad \mathbf{Y} = \mathbf{M}^{(1)}\left(\mathbf{X} - \mathbf{X}^{*}\right), \tag{C.12}$$

which can be further simplified to

$$\mathbf{X} = \left(\mathbf{L}^{(1)} - \mathbf{I}\right)\mathbf{Y}^{*} \quad \text{and} \quad \mathbf{Y} = \left(\mathbf{M}^{(1)} - \mathbf{I}\right)\mathbf{X}^{*}. \tag{C.13}$$

If we introduce two tensors **A** and **B**, with $\mathbf{A} = \mathbf{L}^{(1)} - \mathbf{I}$ and $\mathbf{B} = \mathbf{M}^{(1)} - \mathbf{I}$, we can rewrite Eq. (C.11) and (C.13) in components as

$$\begin{bmatrix} \varepsilon \\ -E \\ -H \end{bmatrix} = \begin{bmatrix} S_{11}^{(1)} & S_{12}^{(1)} & S_{13}^{(1)} \\ S_{21}^{(1)} & S_{22}^{(1)} & S_{23}^{(1)} \\ S_{31}^{(1)} & S_{32}^{(1)} & S_{33}^{(1)} \end{bmatrix} \begin{bmatrix} \varepsilon^* \\ -E^* \\ -H^* \end{bmatrix}, \quad \begin{bmatrix} \sigma \\ D \\ B \end{bmatrix} = \begin{bmatrix} T_{11}^{(1)} & T_{12}^{(1)} & T_{13}^{(1)} \\ T_{21}^{(1)} & T_{22}^{(1)} & T_{23}^{(1)} \\ T_{31}^{(1)} & T_{32}^{(1)} & T_{33}^{(1)} \end{bmatrix} \begin{bmatrix} \sigma^* \\ D^* \\ B^* \end{bmatrix}$$
$$\begin{bmatrix} \sigma \\ D \\ B \end{bmatrix} = \begin{bmatrix} A_{11} & A_{12} & A_{13} \\ A_{21} & A_{22} & A_{23} \\ A_{31} & A_{32} & A_{33} \end{bmatrix} \begin{bmatrix} \varepsilon^* \\ -E^* \\ -H^* \end{bmatrix}, \quad \begin{bmatrix} \varepsilon \\ -E \\ -H \end{bmatrix} = \begin{bmatrix} B_{11} & B_{12} & B_{13} \\ B_{21} & B_{22} & B_{23} \\ B_{31} & B_{32} & B_{33} \end{bmatrix} \begin{bmatrix} \sigma^* \\ D^* \\ B^* \end{bmatrix}. \tag{C.14}$$

This set of relations can be used to construct the S-tensor for any kind of constitutive equations. Here we take the S-tensor for independent variables (ε, D, B), denoted by $\mathbf{S}^{(2)}$, as an example. The definition of $\mathbf{S}^{(2)}$ is given by

$$\begin{bmatrix} \varepsilon \\ D \\ B \end{bmatrix} = \begin{bmatrix} S_{11}^{(2)} & S_{12}^{(2)} & S_{13}^{(2)} \\ S_{21}^{(2)} & S_{22}^{(2)} & S_{23}^{(2)} \\ S_{31}^{(2)} & S_{32}^{(2)} & S_{33}^{(2)} \end{bmatrix} \begin{bmatrix} \varepsilon^* \\ D^* \\ B^* \end{bmatrix}. \tag{C.15}$$

When only ε^* is applied in Eq. (C.15), we have

$$\varepsilon = S_{11}^{(2)}\varepsilon^*, \quad D = S_{21}^{(2)}\varepsilon^*, \quad B = S_{31}^{(2)}\varepsilon^*. \tag{C.16}$$

Likewise, when only ε^* is applied in Eq. (C.14), we have

$$\varepsilon = S_{11}^{(1)}\varepsilon^*, \quad D = A_{21}\varepsilon^*, \quad B = A_{31}\varepsilon^*. \tag{C.17}$$

Comparing Eq. (C.16) with Eq. (C.17), it is easy to get

$$S_{11}^{(2)} = S_{11}^{(1)}, \quad S_{21}^{(2)} = A_{21}, \quad S_{31}^{(2)} = A_{31}. \tag{C.18}$$

Next we can apply D^* only in Eq. (C.14) and (C.15). In the same way we can get

$$S_{12}^{(2)} = B_{12}, \quad S_{22}^{(2)} = T_{22}^{(1)}, \quad S_{32}^{(2)} = T_{32}^{(1)}. \tag{C.19}$$

Finally we can apply B^* only in Eq. (C.14) and (C.15), and get

$$S_{13}^{(2)} = B_{13}, \quad S_{23}^{(2)} = T_{23}^{(1)}, \quad S_{33}^{(2)} = T_{33}^{(1)}. \tag{C.20}$$

In summary, the S-tensor for independent variables (ε, D, B), $\mathbf{S}^{(2)}$, is given by

$$\mathbf{S}^{(2)} = \begin{bmatrix} S_{11}^{(1)} & B_{12} & B_{13} \\ A_{21} & T_{22}^{(1)} & T_{23}^{(1)} \\ A_{31} & T_{32}^{(1)} & T_{33}^{(1)} \end{bmatrix}. \tag{C.21}$$

And the S-tensors for other kinds of constitutive equations can be derived in the same way. It should be pointed out that, for $\mathbf{S}^{(2)}$, and the corresponding moduli matrix $\mathbf{L}^{(2)}$ for independent variables (ε, D, B), they also satisfy that $\mathbf{S}^{(2)}\left(\mathbf{L}^{(2)}\right)^{-1}$ is symmetric (given that $\mathbf{L}^{(2)}$ has already been adjusted to a symmetric matrix). In addition, not only can we use M-T method to calculate the effective property of multiferroic composites with moduli matrix $\mathbf{L}^{(1)}$ and S-tensor $\mathbf{S}^{(1)}$, but we also can do the same for multiferroic composites with moduli matrix $\mathbf{L}^{(2)}$ and S-tensor $\mathbf{S}^{(2)}$. And the effective property at any specific volume concentration c_1, given by these two ways, are interchangeable by the rules discussed in Appendix B.

Appendix D.

Explicit results for 1-3 and 2-2 multiferroic composites

For fibrous composites and multilayers, explicit formulae for the components of S-tensors are listed in Appendix C. With them and the theory given in Chapter 4 for the perfect and imperfect interface, we can obtain the explicit expressions for the magnetoelectric coupling coefficients, α_{33} and α_{11}. As 1-3 and 2-2 composites are widely useful, we present the results here for ready reference.

In reading the following expressions, care must be exercised that superscript "*e*" always refers to the properties of $BaTiO_3$ regardless whether BTO exists as the matrix or inclusions, and superscript "*m*" always refers to the properties of $CoFe_2O_4$, also regardless whether it exists as inclusion or matrix. Superscript "*i*" on the other hand refers to the properties of the interface. In addition, for 1-3 composites, c_1 and c_0 denote the volume concentrations of the inclusions and matrix, respectively, which could be CFO or BTO. c_{int} denotes the volume concentration of interface in the thinly-coated inclusion. While for 2-2 composites, c_0, c_1 and c_{int} denote the volume concentrations of BTO, CFO and interface in the whole composite, so that they satisfy $c_0 + c_1 + c_{\text{int}} = 1$.

D.1. The 1-3 fibrous composites with a perfect interface

First, with $CoFe_2O_4$ as inclusions and $BaTiO_3$ as the matrix, we can find

$$\alpha_{33} = -\frac{2c_0c_1e_{31}^{(e)}q_{31}^{(m)}}{C_{11}^{(e)} + C_{11}^{(m)} - c_0\left(C_{12}^{(e)} - C_{12}^{(m)}\right) + c_1\left(C_{11}^{(e)} - C_{11}^{(m)}\right)}, \tag{D.1}$$

and

$$\alpha_{11} = -\frac{4c_0c_1e_{15}^{(e)}q_{15}^{(m)}\kappa_{11}^{(m)}\mu_{11}^{(e)}}{D_{\alpha 11}^{\mathrm{BTO}}}, \tag{D.2}$$

where the denominator $D_{\alpha 11}^{\mathrm{BTO}}$ is

$$D_{\alpha 11}^{\mathrm{BTO}} = c_0{}^2 q_{15}^{(m)2}\left[\kappa_{11}^{(e)} + \kappa_{11}^{(m)} + c_1\left(\kappa_{11}^{(e)} - \kappa_{11}^{(m)}\right)\right] + \left\{\left(1+c_1\right)^2 e_{15}^{(e)2} + \left[C_{44}^{(e)} + C_{44}^{(m)} + c_1\left(C_{44}^{(e)} - C_{44}^{(m)}\right)\right]\times \left[\kappa_{11}^{(e)} + \kappa_{11}^{(m)} + c_1\left(\kappa_{11}^{(e)} - \kappa_{11}^{(m)}\right)\right]\right\}\left[\mu_{11}^{(e)} + \mu_{11}^{(m)} + c_1\left(\mu_{11}^{(e)} - \mu_{11}^{(m)}\right)\right]. \tag{D.3}$$

On the other hand, with $BaTiO_3$ as inclusions and $CoFe_2O_4$ as the matrix, the results are

$$\alpha_{33} = -\frac{2c_0c_1e_{31}^{(e)}q_{31}^{(m)}}{C_{11}^{(e)} + C_{11}^{(m)} + c_0\left(C_{12}^{(e)} - C_{12}^{(m)}\right) - c_1\left(C_{11}^{(e)} - C_{11}^{(m)}\right)}, \tag{D.4}$$

and

$$\alpha_{11} = -\frac{4c_0c_1e_{15}^{(e)}q_{15}^{(m)}\kappa_{11}^{(m)}\mu_{11}^{(e)}}{D_{\alpha 11}^{\mathrm{CFO}}}, \tag{D.5}$$

where the denominator $D_{\alpha 11}^{\mathrm{CFO}}$ is

$$D_{\alpha 11}^{\mathrm{CFO}} = c_0{}^2 e_{15}^{(e)2}\left[\mu_{11}^{(m)} + \mu_{11}^{(e)} + c_1\left(\mu_{11}^{(m)} - \mu_{11}^{(e)}\right)\right] + \left\{\left(1+c_1\right)^2 q_{15}^{(m)2} + \left[C_{44}^{(m)} + C_{44}^{(e)} + c_1\left(C_{44}^{(m)} - C_{44}^{(e)}\right)\right]\times \left[\mu_{11}^{(m)} + \mu_{11}^{(e)} + c_1\left(\mu_{11}^{(m)} - \mu_{11}^{(e)}\right)\right]\right\}\left[\kappa_{11}^{(m)} + \kappa_{11}^{(e)} + c_1\left(\kappa_{11}^{(m)} - \kappa_{11}^{(e)}\right)\right]. \tag{D.6}$$

From the above results, we can see that the signs of α_{33} and α_{11} are directly determined by the product of *e*- and *q*-components, which has been discussed in previous chapter.

D.2. The 1-3 fibrous composites with an imperfect interface

In order to obtain the effective magnetoelectric coefficients of 1-3 multiferroic

composites with an imperfect interface, we first derive the relevant properties of coated inclusion from Eq. (4.10). This in turn can be used for the properties of the inclusion phase in Eq. (4.8) for the overall composite. Since the final results of effective α_{33} and α_{11} are too complicated, here we just present the results for the properties of coated inclusion.

For the coated $CoFe_2O_4$ inclusion - with a prime added to superscript *m* - we can obtain from Eq. (4.10) that

$$C_{11}^{(m')}=\frac{C_{11}^{(i)}\left(C_{11}^{(m)}+C_{12}^{(m)}+2C_{44}^{(i)}\right)}{2C_{11}^{(i)}+c_{\text{int}}\left(C_{11}^{(m)}+C_{12}^{(m)}-2C_{11}^{(i)}+2C_{44}^{(i)}\right)}+\frac{2\left(1-c_{\text{int}}\right)C_{11}^{(i)}C_{44}^{(i)}\left(C_{11}^{(m)}-C_{12}^{(m)}-2C_{44}^{(i)}\right)}{4C_{11}^{(i)}C_{44}^{(i)}+c_{\text{int}}\left(C_{11}^{(i)}+C_{44}^{(i)}\right)\left(C_{11}^{(m)}-C_{12}^{(m)}-2C_{44}^{(i)}\right)},$$

(D.7)

$$C_{12}^{(m')}=\frac{C_{11}^{(i)}\left(C_{11}^{(m)}+C_{12}^{(m)}+2C_{44}^{(i)}\right)}{2C_{11}^{(i)}+c_{\text{int}}\left(C_{11}^{(m)}+C_{12}^{(m)}-2C_{11}^{(i)}+2C_{44}^{(i)}\right)}-\frac{2C_{44}^{(i)}\left[C_{11}^{(i)}\left(C_{11}^{(m)}-C_{12}^{(m)}+2C_{44}^{(i)}\right)+c_{\text{int}}C_{44}^{(i)}\left(C_{11}^{(m)}-C_{12}^{(m)}-2C_{44}^{(i)}\right)\right]}{4C_{11}^{(i)}C_{44}^{(i)}+c_{\text{int}}\left(C_{11}^{(i)}+C_{44}^{(i)}\right)\left(C_{11}^{(m)}-C_{12}^{(m)}-2C_{44}^{(i)}\right)},$$

(D.8)

$$C_{44}^{(m')}=C_{44}^{(i)}\frac{4C_{44}^{(m)}\mu^{(i)}+2c_{\text{int}}\left[q_{15}^{(m)2}+C_{44}^{(m)}\left(\mu_{11}^{(m)}-\mu^{(i)}\right)-\mu^{(i)}\left(C_{44}^{(m)}-C_{44}^{(i)}\right)\right]-c_{\text{int}}^2\left[q_{15}^{(m)2}+\left(C_{44}^{(m)}-C_{44}^{(i)}\right)\left(\mu_{11}^{(m)}-\mu^{(i)}\right)\right]}{4C_{44}^{(i)}\mu^{(i)}+2c_{\text{int}}\left[C_{44}^{(i)}\left(\mu_{11}^{(m)}-\mu^{(i)}\right)+\mu^{(i)}\left(C_{44}^{(m)}-C_{44}^{(i)}\right)\right]+c_{\text{int}}^2\left[q_{15}^{(m)2}+\left(C_{44}^{(m)}-C_{44}^{(i)}\right)\left(\mu_{11}^{(m)}-\mu^{(i)}\right)\right]},$$

(D.9)

$$q_{31}^{(m')}=\frac{2\left(1-c_{\text{int}}\right)q_{31}^{(m)}C_{11}^{(i)}}{c_{\text{int}}\left(C_{11}^{(m)}+C_{12}^{(m)}-2C_{11}^{(i)}+2C_{44}^{(i)}\right)+2C_{11}^{(i)}},\tag{D.10}$$

$$q_{15}^{(m')}=\frac{4\left(1-c_{\text{int}}\right)q_{15}^{(m)}C_{44}^{(i)}\mu^{(i)}}{4C_{44}^{(i)}\mu^{(i)}+2c_{\text{int}}\left[C_{44}^{(i)}\left(\mu_{11}^{(m)}-\mu^{(i)}\right)+\mu^{(i)}\left(C_{44}^{(m)}-C_{44}^{(i)}\right)\right]+c_{\text{int}}^2\left[q_{15}^{(m)2}+\left(C_{44}^{(m)}-C_{44}^{(i)}\right)\left(\mu_{11}^{(m)}-\mu^{(i)}\right)\right]},$$

(D.11)

$$\kappa_{11}^{(m')}=\kappa^{(i)}\frac{2\kappa_{11}^{(m)}-c_{\text{int}}\left(\kappa_{11}^{(m)}-\kappa^{(i)}\right)}{2\kappa^{(i)}+c_{\text{int}}\left(\kappa_{11}^{(m)}-\kappa^{(i)}\right)},\tag{D.12}$$

$$\mu_{11}^{(m')}=\mu^{(i)}\frac{4\mu_{11}^{(m)}C_{44}^{(i)}+2c_{\text{int}}\left[q_{15}^{(m)2}+\mu_{11}^{(m)}\left(C_{44}^{(m)}-C_{44}^{(i)}\right)-C_{44}^{(i)}\left(\mu_{11}^{(m)}-\mu^{(i)}\right)\right]-c_{\text{int}}^2\left[q_{15}^{(m)2}+\left(C_{44}^{(m)}-C_{44}^{(i)}\right)\left(\mu_{11}^{(m)}-\mu^{(i)}\right)\right]}{4\mu^{(i)}C_{44}^{(i)}+2c_{\text{int}}\left[\mu^{(i)}\left(C_{44}^{(m)}-C_{44}^{(i)}\right)+C_{44}^{(i)}\left(\mu_{11}^{(m)}-\mu^{(i)}\right)\right]+c_{\text{int}}^2\left[q_{15}^{(m)2}+\left(C_{44}^{(m)}-C_{44}^{(i)}\right)\left(\mu_{11}^{(m)}-\mu^{(i)}\right)\right]}.$$

(D.13)

This set of coated properties can be used to replace the original properties of CFO in Eq. (D.1) to (D.3), to obtain α_{33} and α_{11} of the CFO-in-BTO composite with an imperfect interface.

Likewise, for the coated $BaTiO_3$ inclusion - also with a prime added to superscript *e* - we have

$$C_{12}^{(e')}=\frac{C_{11}^{(i)}\left(C_{11}^{(e)}+C_{12}^{(e)}+2C_{44}^{(i)}\right)}{2C_{11}^{(i)}+c_{\text{int}}\left(C_{11}^{(e)}+C_{12}^{(e)}-2C_{11}^{(i)}+2C_{44}^{(i)}\right)}+\frac{2\left(1-c_{\text{int}}\right)C_{11}^{(i)}C_{44}^{(i)}\left(C_{11}^{(e)}-C_{12}^{(e)}-2C_{44}^{(i)}\right)}{4C_{11}^{(i)}C_{44}^{(i)}+c_{\text{int}}\left(C_{11}^{(i)}+C_{44}^{(i)}\right)\left(C_{11}^{(e)}-C_{12}^{(e)}-2C_{44}^{(i)}\right)},\tag{D.14}$$

$$C_{11}^{(e')}=\frac{C_{11}^{(i)}\left(C_{11}^{(e)}+C_{12}^{(e)}+2C_{44}^{(i)}\right)}{2C_{11}^{(i)}+c_{\text{int}}\left(C_{11}^{(e)}+C_{12}^{(e)}-2C_{11}^{(i)}+2C_{44}^{(i)}\right)}-\frac{2C_{44}^{(i)}\left[C_{11}^{(i)}\left(C_{11}^{(e)}-C_{12}^{(e)}+2C_{44}^{(i)}\right)+c_{\text{int}}C_{44}^{(i)}\left(C_{11}^{(e)}-C_{12}^{(e)}-2C_{44}^{(i)}\right)\right]}{4C_{11}^{(i)}C_{44}^{(i)}+c_{\text{int}}\left(C_{11}^{(i)}+C_{44}^{(i)}\right)\left(C_{11}^{(e)}-C_{12}^{(e)}-2C_{44}^{(i)}\right)},\tag{D.15}$$

$$C_{44}^{(e')}=C_{44}^{(i)}\frac{4C_{44}^{(e)}\kappa^{(i)}+2c_{\text{int}}\left[e_{15}^{(e)2}+C_{44}^{(e)}\left(\kappa_{11}^{(e)}-\kappa^{(i)}\right)-\kappa^{(i)}\left(C_{44}^{(e)}-C_{44}^{(i)}\right)\right]-c_{\text{int}}^{2}\left[e_{15}^{(e)2}+\left(C_{44}^{(e)}-C_{44}^{(i)}\right)\left(\kappa_{11}^{(e)}-\kappa^{(i)}\right)\right]}{4C_{44}^{(i)}\kappa^{(i)}+2c_{\text{int}}\left[C_{44}^{(i)}\left(\kappa_{11}^{(e)}-\kappa^{(i)}\right)+\kappa^{(i)}\left(C_{44}^{(e)}-C_{44}^{(i)}\right)\right]+c_{\text{int}}^{2}\left[e_{15}^{(e)2}+\left(C_{44}^{(e)}-C_{44}^{(i)}\right)\left(\kappa_{11}^{(e)}-\kappa^{(i)}\right)\right]},\tag{D.16}$$

$$e_{31}^{(e')}=\frac{2\left(1-c_{\text{int}}\right)e_{31}^{(e)}C_{11}^{(i)}}{c_{\text{int}}\left(C_{11}^{(e)}+C_{12}^{(e)}-2C_{11}^{(i)}+2C_{44}^{(i)}\right)+2C_{11}^{(i)}},\tag{D.17}$$

$$e_{15}^{(e')}=\frac{4\left(1-c_{\text{int}}\right)e_{15}^{(e)}C_{44}^{(i)}\kappa^{(i)}}{4C_{44}^{(i)}\kappa^{(i)}+2c_{\text{int}}\left[C_{44}^{(i)}\left(\kappa_{11}^{(e)}-\kappa^{(i)}\right)+\kappa^{(i)}\left(C_{44}^{(e)}-C_{44}^{(i)}\right)\right]+c_{\text{int}}^{2}\left[e_{15}^{(e)2}+\left(C_{44}^{(e)}-C_{44}^{(i)}\right)\left(\kappa_{11}^{(e)}-\kappa^{(i)}\right)\right]},\tag{D.18}$$

$$\kappa_{11}^{(e')}=\kappa^{(i)}\frac{4\kappa_{11}^{(e)}C_{44}^{(i)}+2c_{\text{int}}\left[e_{15}^{(e)2}+\kappa_{11}^{(e)}\left(C_{44}^{(e)}-C_{44}^{(i)}\right)-C_{44}^{(i)}\left(\kappa_{11}^{(e)}-\kappa^{(i)}\right)\right]-c_{\text{int}}^{2}\left[e_{15}^{(e)2}+\left(C_{44}^{(e)}-C_{44}^{(i)}\right)\left(\kappa_{11}^{(e)}-\kappa^{(i)}\right)\right]}{4\kappa^{(i)}C_{44}^{(i)}+2c_{\text{int}}\left[\kappa^{(i)}\left(C_{44}^{(e)}-C_{44}^{(i)}\right)+C_{44}^{(i)}\left(\kappa_{11}^{(e)}-\kappa^{(i)}\right)\right]+c_{\text{int}}^{2}\left[e_{15}^{(e)2}+\left(C_{44}^{(e)}-C_{44}^{(i)}\right)\left(\kappa_{11}^{(e)}-\kappa^{(i)}\right)\right]},\tag{D.19}$$

$$\mu_{11}^{(e')}=\mu^{(i)}\frac{2\mu_{11}^{(e)}-c_{\text{int}}\left(\mu_{11}^{(e)}-\mu^{(i)}\right)}{2\mu^{(i)}+c_{\text{int}}\left(\mu_{11}^{(e)}-\mu^{(i)}\right)}.\tag{D.20}$$

This set of coated properties can be used to replace the original properties of BTO in Eq. (D.4) to (D.6), to obtain α_{33} and α_{11} of the BTO-in-CFO composite with an

imperfect interface.

D.3. The 2-2 multiferroic multilayers with a perfect interface

For the 2-2 multiferroic composites with a perfect interface, we find

$$\alpha_{33} = -\frac{c_0 c_1 e_{33}^{(e)} q_{33}^{(m)} \kappa_{33}^{(m)} \mu_{33}^{(e)}}{D_{\alpha 33}}, \tag{D.21}$$

and

$$\alpha_{11} = -\frac{c_0 c_1 e_{15}^{(e)} q_{15}^{(m)}}{c_0 C_{44}^{(m)} + c_1 C_{44}^{(e)}}, \tag{D.22}$$

where the denominator $D_{\alpha 33}$ is

$$\begin{aligned} D_{\alpha 33} = {} & c_0^2 \left(c_0 \kappa_{33}^{(m)} + c_1 \kappa_{33}^{(e)}\right)\left(q_{33}^{(m)2} + C_{33}^{(m)} \mu_{33}^{(m)}\right) + c_0 c_1 \Big[\left(c_0 \kappa_{33}^{(m)} + c_1 \kappa_{33}^{(e)}\right) C_{33}^{(m)} \mu_{33}^{(e)} \\ & + \left(c_0 \mu_{33}^{(m)} + c_1 \mu_{33}^{(e)}\right) C_{33}^{(e)} \kappa_{33}^{(m)}\Big] + c_1^2 \left(c_0 \mu_{33}^{(m)} + c_1 \mu_{33}^{(e)}\right)\left(e_{33}^{(e)2} + C_{33}^{(e)} \kappa_{33}^{(e)}\right), \end{aligned} \tag{D.23}$$

where c_0 is for BTO and c_1 for CFO.

D.4. The 2-2 multiferroic multilayers with an imperfect interface

With an imperfect interface (denoted with the prime symbol), we have

$$\alpha_{33}^{'} = -\frac{c_0 c_1 e_{33}^{(e)} q_{33}^{(m)} \kappa_{33}^{(m)} \mu_{33}^{(e)} C_{11}^{(i)} \kappa^{(i)} \mu^{(i)}}{D_{\alpha 33}^{'}}, \tag{D.24}$$

and

$$\alpha_{11}^{'} = -\frac{c_0 c_1 e_{15}^{(e)} q_{15}^{(m)} C_{44}^{(i)}}{c_0 C_{44}^{(m)} C_{44}^{(i)} + c_1 C_{44}^{(e)} C_{44}^{(i)} + c_{\text{int}} C_{44}^{(e)} C_{44}^{(m)}}, \tag{D.25}$$

where the denominator $D_{\alpha 33}^{'}$ is

$$D_{\alpha 33}^{'} = \lambda_1 c_0^3 + \lambda_2 c_1^3 + \lambda_3 c_{\text{int}}^3 + \lambda_4 c_0^2 c_1 + \lambda_5 c_1^2 c_0 + \lambda_6 c_0^2 c_{\text{int}} + \lambda_7 c_1^2 c_{\text{int}} + \lambda_8 c_0 c_{\text{int}}^2 + \lambda_9 c_1 c_{\text{int}}^2 + \lambda_{10} c_0 c_1 c_{\text{int}}. \tag{D.26}$$

And the coefficients λ_1 to λ_{10} are given by

$$\lambda_1 = \kappa_{33}^{(m)}\left(q_{33}^{(m)2} + C_{33}^{(m)}\mu_{33}^{(m)}\right)C_{11}^{(i)}\kappa^{(i)}\mu^{(i)}, \quad \lambda_2 = \mu_{33}^{(e)}\left(e_{33}^{(e)2} + C_{33}^{(e)}\kappa_{33}^{(e)}\right)C_{11}^{(i)}\kappa^{(i)}\mu^{(i)},$$

$$\lambda_3 = \mu_{33}^{(e)}\left(e_{33}^{(e)2} + C_{33}^{(e)}\kappa_{33}^{(e)}\right)\kappa_{33}^{(m)}\left(q_{33}^{(m)2} + C_{33}^{(m)}\mu_{33}^{(m)}\right),$$

$$\lambda_4 = C_{11}^{(i)}\kappa^{(i)}\mu^{(i)}\left[\kappa_{33}^{(e)}\left(q_{33}^{(m)2} + C_{33}^{(m)}\mu_{33}^{(m)}\right) + \kappa_{33}^{(m)}\left(C_{33}^{(e)}\mu_{33}^{(m)} + C_{33}^{(m)}\mu_{33}^{(e)}\right)\right],$$

$$\lambda_5 = C_{11}^{(i)}\kappa^{(i)}\mu^{(i)}\left[\mu_{33}^{(m)}\left(e_{33}^{(e)2} + C_{33}^{(e)}\kappa_{33}^{(e)}\right) + \mu_{33}^{(e)}\left(C_{33}^{(e)}\kappa_{33}^{(m)} + C_{33}^{(m)}\kappa_{33}^{(e)}\right)\right],$$

$$\lambda_6 = \kappa_{33}^{(m)}\left(q_{33}^{(m)2} + C_{33}^{(m)}\mu_{33}^{(m)}\right)\left[C_{33}^{(e)}\kappa^{(i)}\mu^{(i)} + C_{11}^{(i)}\left(\kappa^{(i)}\mu_{33}^{(e)} + \kappa_{33}^{(e)}\mu^{(i)}\right)\right],$$

$$\lambda_7 = \mu_{33}^{(e)}\left(e_{33}^{(e)2} + C_{33}^{(e)}\kappa_{33}^{(e)}\right)\left[C_{33}^{(m)}\kappa^{(i)}\mu^{(i)} + C_{11}^{(i)}\left(\kappa^{(i)}\mu_{33}^{(m)} + \kappa_{33}^{(m)}\mu^{(i)}\right)\right],$$

$$\lambda_8 = \kappa_{33}^{(m)}\left(q_{33}^{(m)2} + C_{33}^{(m)}\mu_{33}^{(m)}\right)\left[\mu^{(i)}\left(e_{33}^{(e)2} + C_{33}^{(e)}\kappa_{33}^{(e)}\right) + \mu_{33}^{(e)}\left(C_{33}^{(e)}\kappa^{(i)} + C_{11}^{(i)}\kappa_{33}^{(e)}\right)\right],$$

$$\lambda_9 = \mu_{33}^{(e)}\left(e_{33}^{(e)2} + C_{33}^{(e)}\kappa_{33}^{(e)}\right)\left[\kappa^{(i)}\left(q_{33}^{(m)2} + C_{33}^{(m)}\mu_{33}^{(m)}\right) + \kappa_{33}^{(m)}\left(C_{33}^{(m)}\mu^{(i)} + C_{11}^{(i)}\mu_{33}^{(m)}\right)\right],$$

$$\lambda_{10} = C_{11}^{(\mathrm{int})}\left[\kappa_{33}^{(m)}\mu_{33}^{(m)}\mu^{\mathrm{int}}\left(e_{33}^{(e)2} + C_{33}^{(e)}\kappa_{33}^{(e)}\right) + \kappa_{33}^{(e)}\mu_{33}^{(e)}\kappa^{\mathrm{int}}\left(q_{33}^{(m)2} + C_{33}^{(m)}\mu_{33}^{(m)}\right) + \right.$$
$$\left.\kappa_{33}^{(m)}\mu_{33}^{(e)}\left(C_{33}^{(e)}\mu_{33}^{(m)}\kappa^{\mathrm{int}} + C_{33}^{(m)}\kappa_{33}^{(e)}\mu^{\mathrm{int}}\right)\right] + \kappa^{\mathrm{int}}\mu^{\mathrm{int}}\left(e_{33}^{(e)2} + C_{33}^{(e)}\kappa_{33}^{(e)}\right)\left(q_{33}^{(m)2} + C_{33}^{(m)}\mu_{33}^{(m)}\right).$$

(D.27)

Appendix E.

An incremental scheme for solving 0-0 and 1-1 connectivity

The equation governing the effective electro-magneto-elastic moduli, $\mathbf{L}_e$, for multiferroic composites with 0-0 and 1-1 connectivity has been given by Eq. (5.2). For convenience we denote the left-hand side of Eq. (5.2) as a function **W**, such that

$$\mathbf{W} \equiv \mathbf{S}\mathbf{L}_e^{-1} + c_1\left(\mathbf{L}_2 - \mathbf{L}_e\right)^{-1} + c_2\left(\mathbf{L}_1 - \mathbf{L}_e\right)^{-1} = \mathbf{0}. \tag{E.1}$$

Our goal is to solve the unknown moduli $\mathbf{L}_e$, which is a 12×12 matrix. With the transversely isotropic property, it has 17 independent constants. Taking 3-direction to be the symmetric axis, we then can write $\mathbf{L}_e$ in terms of these constants

$$\mathbf{L}_e = \left(C_{11}, C_{12}, C_{13}, C_{33}, C_{44}, e_{31}, e_{33}, e_{15}, q_{31}, q_{33}, q_{15}, \kappa_{11}, \kappa_{33}, \alpha_{11}, \alpha_{33}, \mu_{11}, \mu_{33}\right), \tag{E.2}$$

which means $\mathbf{L}_e$ depends on these constants, and its dependence has been given by Eq. (4.7). The S-tensor $\mathbf{S}$ also depends on these 17 constants and therefore it is a function of $\mathbf{L}_e$; its dependence has been summarized in Appendix C. At any given volume concentration c_1 (or equivalently c_2, which satisfies $c_2 = 1 - c_1$), Eq. (E.1) becomes a system of 17 independent implicit equations for the 17 undetermined constants of $\mathbf{L}_e$. Though theoretically they can be directly solved, it is actually extremely difficult (almost impossible) to do so, because these equations are highly nonlinear and highly coupled due to the inversion of unknown moduli $\mathbf{L}_e$. Therefore, to this end an increment scheme is proposed to solve this set of equations numerically from $c_1 = 0$ to 1.

First of all, we recognize that **W** is a function of c_1 and $\mathbf{L}_e$, We can then differentiate **W** with respect to c_1 and $\mathbf{L}_e$, as

$$\frac{\partial \mathbf{W}}{\partial \mathbf{L}_e} : \Delta \mathbf{L}_e = -\frac{\partial \mathbf{W}}{\partial c_1} \Delta c_1, \tag{E.3}$$

where the partial derivatives are

$$\begin{aligned} \frac{\partial \mathbf{W}}{\partial \mathbf{L}_e} : \Delta \mathbf{L}_e = & \left(\frac{\partial \mathbf{S}}{\partial \mathbf{L}_e} : \Delta \mathbf{L}_e \right) \mathbf{L}_e^{-1} - \mathbf{S} \mathbf{L}_e^{-1} \Delta \mathbf{L}_e \mathbf{L}_e^{-1} + c_1 \left(\mathbf{L}_2 - \mathbf{L}_e \right)^{-1} \Delta \mathbf{L}_e \left(\mathbf{L}_2 - \mathbf{L}_e \right)^{-1} \\ & + \left(1 - c_1 \right) \left(\mathbf{L}_1 - \mathbf{L}_e \right)^{-1} \Delta \mathbf{L}_e \left(\mathbf{L}_1 - \mathbf{L}_e \right)^{-1}, \end{aligned} \tag{E.4}$$

and

$$\frac{\partial \mathbf{W}}{\partial c_1} \Delta c_1 = \left[\left(\mathbf{L}_2 - \mathbf{L}_e \right)^{-1} - \left(\mathbf{L}_1 - \mathbf{L}_e \right)^{-1} \right] \Delta c_1. \tag{E.5}$$

Eq. (E.3) to (E.5) enables us to calculate $\Delta \mathbf{L}_e$, the increment of $\mathbf{L}_e$, from Δc_1, the increment of volume concentration c_1. If the current values of c_1 and $\mathbf{L}_e$ are already known, we can apply a small Δc_1 and solve for the corresponding $\Delta \mathbf{L}_e$. With these increments, the current values of c_1 and $\mathbf{L}_e$ can be continuously updated to $c_1 + \Delta c_1$ and $\mathbf{L}_e + \Delta \mathbf{L}_e$. In this way the iteration procedure can be carried out from $c_1 = 0$ to 1, so that the relation between $\mathbf{L}_e$ and c_1 can be determined. This is the main idea of our incremental scheme.

At the starting point $c_1 = 0$, it is obvious that $\mathbf{L}_e = \mathbf{L}_2$, since now $\mathbf{L}_2$ is the sole existing phase. However it should also be noted that, at this point, the effective-medium equation has a singularity (as well as at $c_1 = 1$), thus for the calculation of partial derivatives at this point, we should use an equivalent form of Eq. (E.1) (denoted by **W'**), which is

$$\mathbf{W}' = c_2 \left(\mathbf{L}_2 - \mathbf{L}_e \right) \left[\mathbf{I} + \mathbf{S} \mathbf{L}_e^{-1} \left(\mathbf{L}_2 - \mathbf{L}_e \right) \right]^{-1} + c_1 \left(\mathbf{L}_1 - \mathbf{L}_e \right) \left[\mathbf{I} + \mathbf{S} \mathbf{L}_e^{-1} \left(\mathbf{L}_1 - \mathbf{L}_e \right) \right]^{-1} = \mathbf{0}. \tag{E.6}$$

Then the partial derivatives at $c_1 = 0$ are given as

$$\frac{\partial \mathbf{W}'}{\partial \mathbf{L}_e} : \Delta \mathbf{L}_e = \Delta \mathbf{L}_e, \tag{E.7}$$

and

$$\frac{\partial \mathbf{W}'}{\partial c_1}\Delta c_1 = \left(\mathbf{L}_1 - \mathbf{L}_e\right)\left[\mathbf{I} + \mathbf{S}\mathbf{L}_e^{-1}\left(\mathbf{L}_1 - \mathbf{L}_e\right)\right]^{-1}\Delta c_1. \tag{E.8}$$

With the value of $\mathbf{L}_e$ and the partial derivatives of $\mathbf{W}'$ at $c_1 = 0$, the iteration can then start. During the iteration, we only need to solve for the 17 independent material constants, rather than the entire matrix of $\mathbf{L}_e$, from the 17 implicit equations. We now use *v* to denote these constants and *w* for the left-hand side of the equation set, so that

$$\begin{aligned} v &= \left(v_1, v_2, v_3, v_4, v_5, v_6, v_7, v_8, v_9, v_{10}, v_{11}, v_{12}, v_{13}, v_{14}, v_{15}, v_{16}, v_{17}\right) \\ &= \left(C_{11}, C_{12}, C_{13}, C_{33}, C_{44}, e_{31}, e_{33}, e_{15}, q_{31}, q_{33}, q_{15}, \kappa_{11}, \kappa_{33}, \alpha_{11}, \alpha_{33}, \mu_{11}, \mu_{33}\right), \end{aligned} \tag{E.9}$$

and

$$\begin{aligned} w &= \left(w_1, w_2, w_3, w_4, w_5, w_6, w_7, w_8, w_9, w_{10}, w_{11}, w_{12}, w_{13}, w_{14}, w_{15}, w_{16}, w_{17}\right) \\ &= \left(W_{11}, W_{12}, W_{13}, W_{33}, W_{44}, W_{19}, W_{39}, W_{57}, W_{1,12}, W_{3,12}, W_{5,10}, W_{77}, W_{99}, W_{7,10}, W_{9,12}, W_{10,10}, W_{12,12}\right). \end{aligned} \tag{E.10}$$

Then Eq. (E.3) can be rewritten as

$$\frac{\partial w_i}{\partial v_j}\Delta v_j = -\frac{\partial w_i}{\partial c_1}\Delta c_1, \tag{E.11}$$

where $i, j = 1 \sim 17$. Eq. (E.11) is a system of 17 linear equations. In order to solve it, a crucial step is to obtain the coefficients $\partial w_i / \partial v_j$ as well as $\partial w_i / \partial c_1$. Since **W** is a function of 17 independent constants v_i $(i = 1 \sim 17)$ and c_1, theoretically both partial derivatives can be analytically evaluated. However, their explicit forms are extremely complicated, due to three inversion operations and the complex form of S-tensor. Especially, for 0-0 connectivity, S-tensor has to be computed by Gaussian quadrature. In this case, although with a pretty long expression, it is still guaranteed that S-tensor can be expressed as a function of 17 independent constants and c_1. But as a

consequence of the complexity, it is advised to use mathematical program such as Mathematica to compute $\partial w_i/\partial v_j$ and $\partial w_i/\partial c_1$. Both of them are the functions of v_i $(i=1\sim 17)$ and c_1.

With the results for $\partial w_i/\partial v_j$ and $\partial w_i/\partial c_1$, our numerical scheme can further be illustrated as the following iterative procedures: (i) for the multiferroic composite, if the current values for 17 independent constants are already known at a given c_1, use them to calculate $\partial w_i/\partial v_j$ and $\partial w_i/\partial c_1$ at this c_1; (ii) substitute the results of these partial derivatives into Eq. (E.11), then take Δc_1 as a small, fixed value (for example, we have used 1/4000) to get a system of linear equations for Δv_i $(i=1\sim 17)$; (3) solve the linear equation system and add these incremental values Δv_i to the original 17 independent constants v_i, and to this end we have calculated the effective properties of the multiferroic composite at volume concentration $c_1+\Delta c_1$. Finally, with the initial conditions at $c_1=0$, repeat these abovementioned iterative procedures and we can fully obtain the effective properties of the multiferroic composite from $c_1=0$ to $c_1=1$.

References

[1]Eshelby, J. D., *"The Determination of the Elastic Field of an Ellipsoidal Inclusion, and Related Problems"*, Proceedings of the Royal Society of London A: Mathematical, Physical and Engineering Sciences **241.** 376-396 (1957).

[2]Liu, L. P., *"Solutions to the Eshelby conjectures"*, Proceedings of the Royal Society of London A: Mathematical, Physical and Engineering Sciences **464.** 573-594 (2008).

[3]Dunn, M. L. and Taya, M., *"An Analysis of Piezoelectric Composite Materials Containing Ellipsoidal Inhomogeneities"*, Proceedings of the Royal Society of London A: Mathematical, Physical and Engineering Sciences **443.** 265-287 (1993).

[4]Dunn, M. L., *"Electroelastic Green's functions for transversely isotropic piezoelectric media and their application to the solution of inclusion and inhomogeneity problems"*, International Journal of Engineering Science **32.** 119-131 (1994).

[5]Huang, J. H. and Yu, J. S., *"Electroelastic Eshelby tensors for an ellipsoidal piezoelectric inclusion"*, Composites Engineering **4.** 1169-1182 (1994).

[6]Huang, J. H., Chiu, Y.-H., and Liu, H.-K., *"Magneto-electro-elastic Eshelby tensors for a piezoelectric-piezomagnetic composite reinforced by ellipsoidal inclusions"*, Journal of Applied Physics **83.** 5364-5370 (1998).

[7]Li, J. Y. and Dunn, M. L., *"Anisotropic coupled-field inclusion and inhomogeneity problems"*, Philosophical Magazine A **77.** 1341-1350 (1998).

[8]Mikata, Y., *"Determination of piezoelectric Eshelby tensor in transversely isotropic piezoelectric solids"*, International Journal of Engineering Science **38.** 605-641 (2000).

[9]Mori, T. and Tanaka, K., *"Average stress in matrix and average elastic energy of materials with misfitting inclusions"*, Acta Metallurgica **21.** 571-574 (1973).

[10]Weng, G. J., *"Some elastic properties of reinforced solids, with special reference to isotropic ones containing spherical inclusions"*, International Journal of Engineering Science **22.** 845-856 (1984).

[11]Benveniste, Y., *"A new approach to the application of Mori-Tanaka's theory in composite materials"*, Mechanics of Materials **6.** 147-157 (1987).

[12]Hatta, H. and Taya, M., *"Effective thermal conductivity of a misoriented short fiber composite"*, Journal of Applied Physics **58.** 2478-2486 (1985).

[13]Nan, C.-W., Birringer, R., Clarke, D. R., and Gleiter, H., *"Effective thermal*

conductivity of particulate composites with interfacial thermal resistance", Journal of Applied Physics **81.** 6692-6699 (1997).

[14]Weng, G. J., *"The theoretical connection between Mori-Tanaka's theory and the Hashin-Shtrikman-Walpole bounds"*, International Journal of Engineering Science **28.** 1111-1120 (1990).

[15]Nan, C.-W., *"Magnetoelectric effect in composites of piezoelectric and piezomagnetic phases"*, Physical Review B **50.** 6082-6088 (1994).

[16]Dunn, M. L. and Taya, M., *"Micromechanics predictions of the effective electroelastic moduli of piezoelectric composites"*, International Journal of Solids and Structures **30.** 161-175 (1993).

[17]Huang, J. H. and Kuo, W.-S., *"The analysis of piezoelectric/piezomagnetic composite materials containing ellipsoidal inclusions"*, Journal of Applied Physics **81.** 1378-1386 (1997).

[18]Li, J. Y. and Dunn, M. L., *"Micromechanics of Magnetoelectroelastic Composite Materials: Average Fields and Effective Behavior"*, Journal of Intelligent Material Systems and Structures **9.** 404-416 (1998).

[19]Bruggeman, D. A. G., *"Calculation of various physics constants in heterogenous substances I Dielectricity constants and conductivity of mixed bodies from isotropic substances"*, Ann. Phys. **24.** 636-664 (1935).

[20]Landauer, R., *"The Electrical Resistance of Binary Metallic Mixtures"*, Journal of Applied Physics **23.** 779-784 (1952).

[21]Budiansky, B., *"On the elastic moduli of some heterogeneous materials"*, Journal of the Mechanics and Physics of Solids **13.** 223-227 (1965).

[22]Hill, R., *"A self-consistent mechanics of composite materials"*, Journal of the Mechanics and Physics of Solids **13.** 213-222 (1965).

[23]Willis, J. R., *"Variational and Related Methods for the Overall Properties of Composites"*, in *Advances in Applied Mechanics*; *Vol. Volume 21*, edited by Y. Chia-Shun (Elsevier, 1981), p. 1-78.

[24]Milton, G. W., *"The theory of composites"*, in *The Theory of Composites* (Cambridge University Press, Cambridge, 2002).

[25]Benveniste, Y. and Milton, G. W., *"The effective medium and the average field approximations vis-à-vis the Hashin–Shtrikman bounds. I. The self-consistent scheme in matrix-based composites"*, Journal of the Mechanics and Physics of Solids **58.** 1026-1038 (2010).

[26]Weng, G. J., *"A dynamical theory for the Mori–Tanaka and Ponte Castañeda–Willis estimates"*, Mechanics of Materials **42.** 886-893 (2010).

[27]Maxwell, J. C., in *A Treatise on Electricity and Magnetism*; *Vol. 1*, 3rd ed. (Clarendon Press, Oxford, 1982), p. 435-441.

[28]Stankovich, S., Dikin, D. A., Dommett, G. H. B., Kohlhaas, K. M., Zimney, E. J., Stach, E. A., Piner, R. D., Nguyen, S. T., and Ruoff, R. S., *"Graphene-based composite materials"*, Nature **442.** 282-286 (2006).

[29]Allen, M. J., Tung, V. C., and Kaner, R. B., *"Honeycomb Carbon: A Review of Graphene"*, Chemical Reviews **110.** 132-145 (2010).

[30]Geim, A. K. and Novoselov, K. S., *"The rise of graphene"*, Nature Materials **6.** 183-191 (2007).

[31]Iijima, S., *"Helical Microtubules of Graphitic Carbon"*, Nature **354.** 56-58 (1991).

[32]Tkalya, E., Ghislandi, M., Otten, R., Lotya, M., Alekseev, A., van der Schoot, P., Coleman, J., de With, G., and Koning, C., *"Experimental and Theoretical Study of the Influence of the State of Dispersion of Graphene on the Percolation Threshold of Conductive Graphene/Polystyrene Nanocomposites"*, ACS Applied Materials & Interfaces **6.** 15113-15121 (2014).

[33]van Suchtelen, J., *"Product properties: a new application of composite materials"*, Philips Research Reports **27.** 28-37 (1972).

[34]Newnham, R. E., Skinner, D. P., and Cross, L. E., *"Connectivity and piezoelectric-pyroelectric composites"*, Materials Research Bulletin **13.** 525-536 (1978).

[35]Harshé, G., Dougherty, J. P., and Newnham, R. E., *"Theoretical modelling of 3-0/0-3 magnetoelectric composites"*, International journal of applied electromagnetics in materials **4.** 161-171 (1993).

[36]Benveniste, Y., *"Magnetoelectric effect in fibrous composites with piezoelectric and piezomagnetic phases"*, Physical Review B **51.** 16424-16427 (1995).

[37]Avellaneda, M. and Harshé, G., *"Magnetoelectric Effect in Piezoelectric/Magnetostrictive Multilayer (2-2) Composites"*, Journal of Intelligent Material Systems and Structures **5.** 501-513 (1994).

[38]Srinivas, S., Li, J. Y., Zhou, Y. C., and Soh, A. K., *"The effective magnetoelectroelastic moduli of matrix-based multiferroic composites"*, Journal of Applied Physics **99.** 043905 (2006).

[39]Bichurin, M. I., Petrov, V. M., and Srinivasan, G., *"Theory of low-frequency*

magnetoelectric coupling in magnetostrictive-piezoelectric bilayers", Physical Review B **68.** 054402 (2003).

[40]Wang, Y., Hasanyan, D., Li, M., Gao, J., Li, J., Viehland, D., and Luo, H., *"Theoretical model for geometry-dependent magnetoelectric effect in magnetostrictive/piezoelectric composites"*, Journal of Applied Physics **111.** 124513 (2012).

[41]Liu, L. P. and Kuo, H.-Y., *"Closed-form solutions to the effective properties of fibrous magnetoelectric composites and their applications"*, International Journal of Solids and Structures **49.** 3055-3062 (2012).

[42]Kuo, H.-Y. and Bhattacharya, K., *"Fibrous composites of piezoelectric and piezomagnetic phases"*, Mechanics of Materials **60.** 159-170 (2013).

[43]Chen, Z., Su, Y., and Meguid, S. A., *"The effect of field-orientation on the magnetoelectric coupling in Terfenol-D/PZT/Terfenol-D laminated structure"*, Journal of Applied Physics **116.** 173910 (2014).

[44]Liu, G., Zhang, C., and Dong, S., *"Magnetoelectric effect in magnetostrictive/piezoelectric laminated composite operating in shear-shear mode"*, Journal of Applied Physics **116.** 074104 (2014).

[45]Ebbesen, T. W., Lezec, H. J., Hiura, H., Bennett, J. W., Ghaemi, H. F., and Thio, T., *"Electrical conductivity of individual carbon nanotubes"*, Nature **382.** 54-56 (1996).

[46]Gardea, F. and Lagoudas, D. C., *"Characterization of electrical and thermal properties of carbon nanotube/epoxy composites"*, Composites Part B: Engineering **56.** 611-620 (2014).

[47]Kirkpatrick, S., *"Percolation and Conduction"*, Reviews of Modern Physics **45.** 574-588 (1973).

[48]Balberg, I. and Binenbaum, N., *"Computer study of the percolation threshold in a two-dimensional anisotropic system of conducting sticks"*, Physical Review B **28.** 3799-3812 (1983).

[49]Nan, C.-W., Shen, Y., and Ma, J., *"Physical Properties of Composites Near Percolation"*, Annual Review of Materials Research **40.** 131-151 (2010).

[50]Stauffer, D. and Aharony, A., *Introduction to percolation theory* (Taylor & Francis, Philadelphia, 1994).

[51]Bauhofer, W. and Kovacs, J. Z., *"A review and analysis of electrical percolation in carbon nanotube polymer composites"*, Composites Science and Technology **69.** 1486-1498 (2009).

[52]Martin, C. A., Sandler, J. K. W., Shaffer, M. S. P., Schwarz, M. K., Bauhofer, W., Schulte, K., and Windle, A. H., *"Formation of percolating networks in multi-wall carbon-nanotube–epoxy composites"*, Composites Science and Technology **64.** 2309-2316 (2004).

[53]De Vivo, B., Lamberti, P., Spinelli, G., and Tucci, V., *"Numerical investigation on the influence factors of the electrical properties of carbon nanotubes-filled composites"*, Journal of Applied Physics **113,** 244301 (2013).

[54]Li, C. and Chou, T.-W., *"Continuum percolation of nanocomposites with fillers of arbitrary shapes"*, Applied Physics Letters **90,** 174108 (2007).

[55]Ma, H. M., Gao, X. L., and Tolle, T. B., *"Monte Carlo modeling of the fiber curliness effect on percolation of conductive composites"*, Applied Physics Letters **96,** 061910 (2010).

[56]Bao, W. S., Meguid, S. A., Zhu, Z. H., and Weng, G. J., *"Tunneling resistance and its effect on the electrical conductivity of carbon nanotube nanocomposites"*, Journal of Applied Physics **111,** 093726 (2012).

[57]Castañeda, P. P. and Willis, J. R., *"The effect of spatial distribution on the effective behavior of composite materials and cracked media"*, Journal of the Mechanics and Physics of Solids **43.** 1919-1951 (1995).

[58]Duan, H. L., Karihaloo, B. L., Wang, J., and Yi, X., *"Effective conductivities of heterogeneous media containing multiple inclusions with various spatial distributions"*, Physical Review B **73.** 174203 (2006).

[59]Pan, Y., Weng, G. J., Meguid, S. A., Bao, W. S., Zhu, Z.-H., and Hamouda, A. M. S., *"Percolation threshold and electrical conductivity of a two-phase composite containing randomly oriented ellipsoidal inclusions"*, Journal of Applied Physics **110,** 123715 (2011).

[60]Hashin, Z. and Shtrikman, S., *"A Variational Approach to the Theory of the Effective Magnetic Permeability of Multiphase Materials"*, Journal of Applied Physics **33.** 3125-3131 (1962).

[61]Maxwell, J. C., *A treatise on electricity and magnetism*, Vol. 1 (Clarendon press, Oxford, 1881).

[62]Balberg, I., Binenbaum, N., and Wagner, N., *"Percolation Thresholds in the Three-Dimensional Sticks System"*, Physical Review Letters **52.** 1465-1468 (1984).

[63]Bao, W. S., Meguid, S. A., Zhu, Z. H., Pan, Y., and Weng, G. J., *"Effect of carbon nanotube geometry upon tunneling assisted electrical network in nanocomposites"*, Journal of Applied Physics **113,** 234313 (2013).

[64]Chatterjee, A. P., *"A percolation-based model for the conductivity of nanofiber composites"*, The Journal of Chemical Physics **139,** 224904 (2013).

[65]Pan, Y., Weng, G. J., Meguid, S. A., Bao, W. S., Zhu, Z.-H., and Hamouda, A. M. S., *"Percolation threshold and electrical conductivity of a two-phase composite containing randomly oriented ellipsoidal inclusions"*, Journal of Applied Physics **110.** 123715 (2011).

[66]Pike, G. E. and Seager, C. H., *"Percolation and conductivity: A computer study. I"*, Physical Review B **10.** 1421-1434 (1974).

[67]Gao, L. and Li, Z., *"Effective medium approximation for two-component nonlinear composites with shape distribution"*, Journal of Physics: Condensed Matter **15.** 4397 (2003).

[68]Dunn, M. L. and Taya, M., *"The effective thermal conductivity of composites with coated reinforcement and the application to imperfect interfaces"*, Journal of Applied Physics **73.** 1711-1722 (1993).

[69]Hashin, Z., *"Thin interphase/imperfect interface in conduction"*, Journal of Applied Physics **89.** 2261-2267 (2001).

[70]Duan, H. L. and Karihaloo, B. L., *"Effective thermal conductivities of heterogeneous media containing multiple imperfectly bonded inclusions"*, Physical Review B **75.** 064206 (2007).

[71]Ngabonziza, Y., Li, J., and Barry, C. F., *"Electrical conductivity and mechanical properties of multiwalled carbon nanotube-reinforced polypropylene nanocomposites"*, Acta Mechanica **220.** 289-298 (2011).

[72]McLachlan, D. S., Chiteme, C., Park, C., Wise, K. E., Lowther, S. E., Lillehei, P. T., Siochi, E. J., and Harrison, J. S., *"AC and DC percolative conductivity of single wall carbon nanotube polymer composites"*, Journal of Polymer Science Part B: Polymer Physics **43.** 3273-3287 (2005).

[73]Mitchell, E. W. J. and Taylor, M. R., *"Mechanism of Stored-Energy Release at 200° C in Electron-Irradiated Graphite"*, Nature **208.** 638-641 (1965).

[74]Chen, H., Müller, M. B., Gilmore, K. J., Wallace, G. G., and Li, D., *"Mechanically Strong, Electrically Conductive, and Biocompatible Graphene Paper"*, Advanced Materials **20.** 3557-3561 (2008).

[75]Singh, V., Joung, D., Zhai, L., Das, S., Khondaker, S. I., and Seal, S., *"Graphene based materials: Past, present and future"*, Progress in Materials Science **56.** 1178-1271 (2011).

[76]Lee, S. and Lu, W., *"Controlling the number of graphene sheets exfoliated from*

graphite by designed normal loading and frictional motion", Journal of Applied Physics **116.** 024313 (2014).

[77]Hernández, J. J., García-Gutiérrez, M. C., Nogales, A., Rueda, D. R., Kwiatkowska, M., Szymczyk, A., Roslaniec, Z., Concheso, A., Guinea, I., and Ezquerra, T. A., *"Influence of preparation procedure on the conductivity and transparency of SWCNT-polymer nanocomposites"*, Composites Science and Technology **69.** 1867-1872 (2009).

[78]Aguilar, J., Bautista-Quijano, J., and Avilés, F., *"Influence of carbon nanotube clustering on the electrical conductivity of polymer composite films"*, Express Polym. Lett **4.** 292-299 (2010).

[79]Cherkasova, A. S. and Shan, J. W., *"Particle Aspect-Ratio and Agglomeration-State Effects on the Effective Thermal Conductivity of Aqueous Suspensions of Multiwalled Carbon Nanotubes"*, Journal of Heat Transfer **132.** 082402-082402 (2010).

[80]Nan, C.-W., Shen, Y., and Ma, J., *"Physical Properties of Composites Near Percolation"*, Annual Review of Materials Research **40.** 131-151 (2010).

[81]Barai, P. and Weng, G. J., *"A theory of plasticity for carbon nanotube reinforced composites"*, International Journal of Plasticity **27.** 539-559 (2011).

[82]Prasher, R., Evans, W., Meakin, P., Fish, J., Phelan, P., and Keblinski, P., *"Effect of aggregation on thermal conduction in colloidal nanofluids"*, Applied Physics Letters **89.** 143119 (2006).

[83]Reinecke, B. N., Shan, J. W., Suabedissen, K. K., and Cherkasova, A. S., *"On the anisotropic thermal conductivity of magnetorheological suspensions"*, Journal of Applied Physics **104.** 023507 (2008).

[84]Kim, K. T., Cha, S. I., Hong, S. H., and Hong, S. H., *"Microstructures and tensile behavior of carbon nanotube reinforced Cu matrix nanocomposites"*, Materials Science and Engineering: A **430.** 27-33 (2006).

[85]Srivastava, N. K. and Mehra, R. M., *"Study of structural, electrical, and dielectric properties of polystyrene/foliated graphite nanocomposite developed via in situ polymerization"*, Journal of Applied Polymer Science **109.** 3991-3999 (2008).

[86]Hill, R., *"Theory of mechanical properties of fibre-strengthened materials: I. Elastic behaviour"*, Journal of the Mechanics and Physics of Solids **12.** 199-212 (1964).

[87]Milgrom, M. and Shtrikman, S., *"Linear response of two-phase composites with cross moduli: Exact universal relations"*, Physical Review A **40.** 1568-1575 (1989).

[88]Wang, X. and Pan, E., *"Magnetoelectric effects in multiferroic fibrous composite with imperfect interface"*, Physical Review B **76.** 214107 (2007).

[89]Dinzart, F. and Sabar, H., *"Magnetoelectric effect in coated fibrous magnetic–piezoelectric composites"*, Journal of Intelligent Material Systems and Structures **23.** 1249-1261 (2012).

[90]Kuo, H.-Y., *"Effective property of multiferroic fibrous composites with imperfect interfaces"*, Smart Materials and Structures **22.** 105005 (2013).

[91]Yue, Y. M. and Xu, K. Y., *"Influence of thin interphase on magnetoelectric effect of coated cylindrical fibrous multiferroic composites"*, Journal of Applied Physics **113.** 224101 (2013).

[92]Willis, J. R., *"Bounds and self-consistent estimates for the overall properties of anisotropic composites"*, Journal of the Mechanics and Physics of Solids **25.** 185-202 (1977).

[93]Weng, G. J., *"Explicit evaluation of Willis' bounds with ellipsoidal inclusions"*, International Journal of Engineering Science **30.** 83-92 (1992).

[94]Zheng, H., Wang, J., Lofland, S. E., Ma, Z., Mohaddes-Ardabili, L., Zhao, T., Salamanca-Riba, L., Shinde, S. R., Ogale, S. B., Bai, F., Viehland, D., Jia, Y., Schlom, D. G., Wuttig, M., Roytburd, A., and Ramesh, R., *"Multiferroic BaTiO3-CoFe2O4 Nanostructures"*, Science **303.** 661-663 (2004).

[95]Li, J. and Weng, G. J., *"A theory of domain switch for the nonlinear behaviour of ferroelectrics"*, Proceedings of the Royal Society of London A: Mathematical, Physical and Engineering Sciences **455.** 3493-3511 (1999).

[96]Weng, G. J. and Wong, D. T., *"Thermodynamic driving force in ferroelectric crystals with a rank-2 laminated domain pattern, and a study of enhanced electrostriction"*, Journal of the Mechanics and Physics of Solids **57.** 571-597 (2009).

[97]Walpole, L. J., *"Elastic Behavior of Composite Materials: Theoretical Foundations"*, in *Advances in Applied Mechanics*; *Vol. Volume 21*, edited by Y. Chia-Shun (Elsevier, 1981), p. 169-242.

[98]Soh, A. K. and Liu, J. X., *"On the Constitutive Equations of Magnetoelectroelastic Solids"*, Journal of Intelligent Material Systems and Structures **16.** 597-602 (2005).

[99]Tandon, G. P. and Weng, G. J., *"The effect of aspect ratio of inclusions on the elastic properties of unidirectionally aligned composites"*, Polymer Composites **5.** 327-333 (1984).

Acknowledgment of Previous Publications

1) Yang Wang, George J. Weng, Shaker A. Meguid and Abdel Magid Hamouda,
"A continuum model with a percolation threshold and tunneling-assisted interfacial conductivity for carbon nanotube-based nanocomposites",
Journal of Applied Physics Vol. **115**, 193706, (2014).

2) Yang Wang, Yu Su, Jackie Li and George J. Weng,
"A theory of magnetoelectric coupling with interface effects and aspect-ratio dependence in piezoelectric-piezomagnetic composites",
Journal of Applied Physics Vol. **117**, 164106, (2015).

3) Yang Wang, Jerry W. Shan and George J. Weng,
"Percolation threshold and electrical conductivity of graphene-based nanocomposites with filler agglomeration and interfacial tunneling",
Journal of Applied Physics Vol. **118**, 065101, (2015).

4) Yang Wang and George J. Weng,
"Magnetoelectric coupling and overall properties of multiferroic composites with 0-0 and 1-1 connectivity",
Journal of Applied Physics Vol. **118**, 174102, (2015).